Università
Ca'Foscari
Venezia

Corso di Laurea Magistrale

in Chimica e Tecnologie Sostenibili
(ordinamento ex D.M. 270/2004)

Tesi di Laurea

Photoreforming: biomass upgrading in gas phase conditions

Relatore
Prof.ssa Michela Signoretto

Correlatore
Dott. Alberto Olivo

Laureando
Danny Zanardo
Matricola 841152

Anno Accademico
2016/2017

Contents:

1. INTRODUCTION

1.1. The energy problem: is our society sustainable?

Human activities require a huge amount of energy and the total primary energy supply (TPES) in 2014 was about 13652 MTOE (millions of tonnes of oil equivalent) [1], deriving mainly (81%) from fossil fuels as shown in Figure 1.

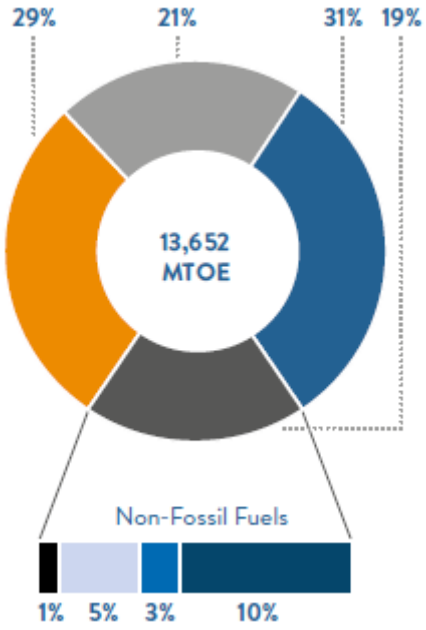

Figure 1 Energy sources of TPES in 2014. Oil (31%), coal (29%), natural gas (21%), biomass (10%), hydropower (3%), nuclear power (5%) and other renewables (1%) [1]

Since the beginning of industrial revolution at the end of XVIII century, fossil fuels have proved to be a more reliable energy source, by combustion, than biomass [1]. Beyond well developed and reliable technologies for surveying, extraction, processing and final utilisation, fossil fuels have an high energy density compared with other sources [1], and an high energy return on energy invested (EROEI) index, that is the ratio between energy gained and energy spent to get it [3]. Oil is the most used and important fossil fuel, and it is mainly used for transportation [1,4]. In 2015 4,4 billion tonnes of oil were produced all around the world, while the proven reserves are 239,4 billion tonnes [5]. This means at a current rate of consumption with current extraction technologies, oil will end in 54 years. Nevertheless, two factors must be kept in mind: on one hand oil request is still increasing, on the other hand, proven reserves have always been rising during decades due to progress in surveying and extraction technologies and the emerging use of non-conventional oil resources [5].

Besides their limited availability, one of the most important problem that affects fossil fuels is pollution issues. Fossil fuels combustion yields several products such as CO_2, CO, NO_x, SO_x and polycyclic aromatic hydrocarbons (PAHs) [6]. The most problematic pollutant is certainly carbon dioxide (CO_2), due to huge amount emitted and its effect on climate worldwide. In 2016, more than 40 billion tonnes of CO_2 were emitted [7] and this human-made waste derived almost only from fossil fuel combustion (99%) [8]. As reported in Figure 2, an exponential trend of CO_2 emission can be seen, that started with the Industrial Revolution and the spread use of fossil fuels.

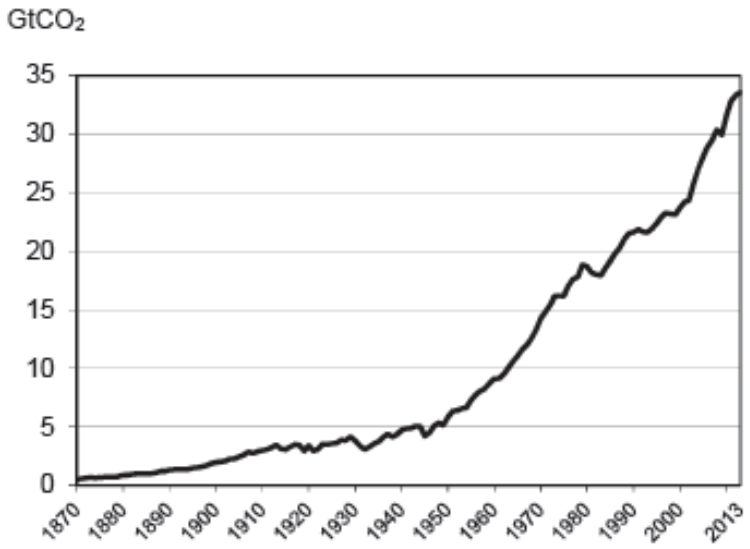

Figure 2 Carbon dioxide concentration trend from 1870 to 2013 [8]

Carbon dioxide concentration in atmosphere is ruled by natural mechanisms [9], but carbon dioxide wasted in atmosphere exceeds their capture and storage capability, thus rising its concentration in air. In July 2017, it has reached 408 ppm, the highest value observed in human history [10]. As reported in Figure 3, the modern increasing trend of atmospheric carbon dioxide is very fast and cannot be attributed to natural oscillation phenomena that occurs in geological era.

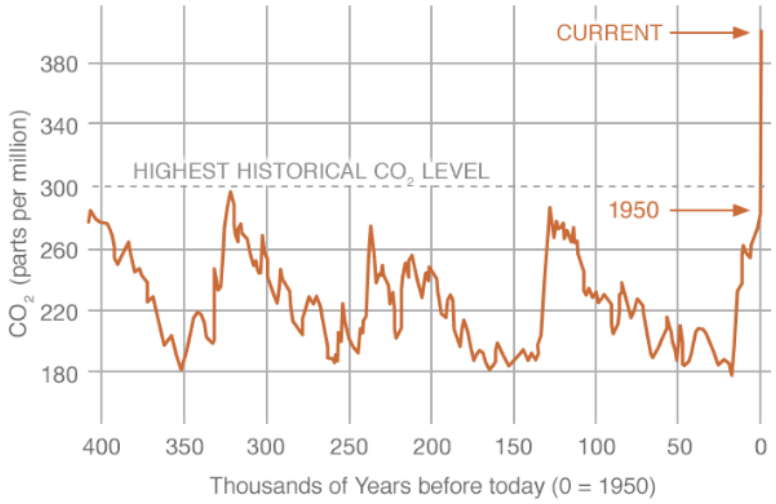

Figure 3 Carbon dioxide concentration (ppm) in air in the last 400'000 years [11]

A question should be asked now: can we continue with current society development without heavy effects on world environmental dynamics? In other terms: is our society sustainable? Climate models [12-15] try to quantitatively predict how current society development will affect Earth's future but, beside calculations, it is obvious that the answer is no. Our society is not sustainable and we have to do something. As previously written, the main cause of climate change is energy production, so we must work mainly on this topic developing more sustainable energy production techniques.

1.2. An alternative: renewable sources

1.2.1 Overview on alternative energy source

Besides fossil fuels many alternative energy sources exist although they actually provide only 19 % of TPES (Figure 4). Nevertheless, these sources provide a wider share in electric power production, about 33 % in 2014, and this is expected to double in the next forty years (Figure 4).

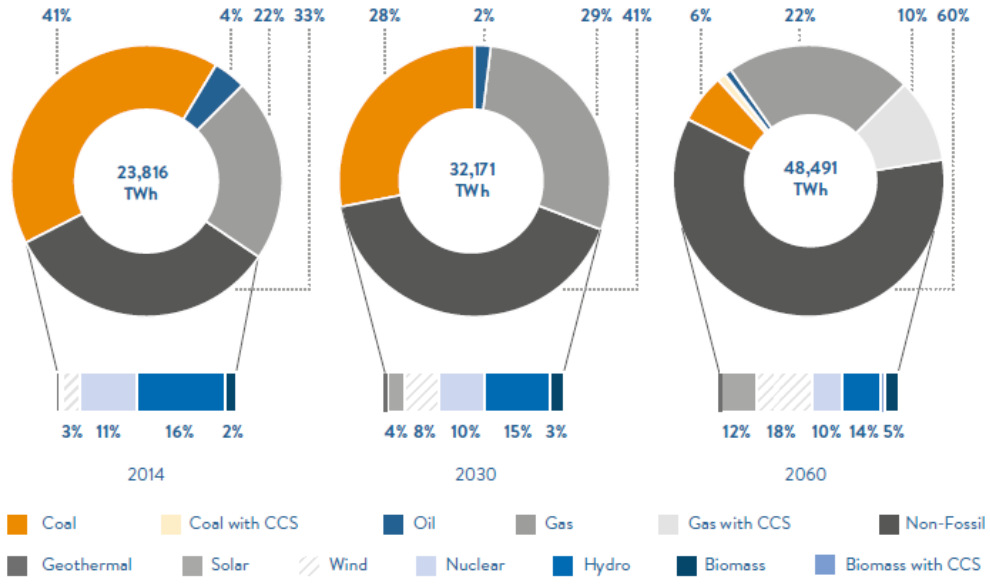

Figure 4 Electricity production by source type (2014) and predictions for 2030 and 2060 [1]

Nuclear energy has experienced a general decrease in development since the Seventies, due to emerging of environmental movements, nuclear accidents and deregulation of energy market that in turn has made expensive investment on nuclear projects less [16]. Hydropower is the most used renewable, supplying 16 % of electric power demand in 2015 [5]. It benefits from several advantages, such as having an high energy efficiency [2], high EROEI index [3], and low GHGs emissions [17]. Wind power is an emerging and promising renewable since it has experienced a huge improvement in installed capacity in the last fifteen years [18]. This is due to its reliability [18] and low environmental impact [2,17]. Beside other renewables, solar power is one of the other promising energy source, that will be explained in the next section.

1.2.2. Power of solar power

The most abundant renewable is probably solar energy [19]. Our planet averagely receives $1{,}8 \cdot 10^{21}$ W of energy from the Sun [20] and the intensity of sunlight just outside Earth's atmosphere is called solar constant and its value is 1360 W/m^2 [21].

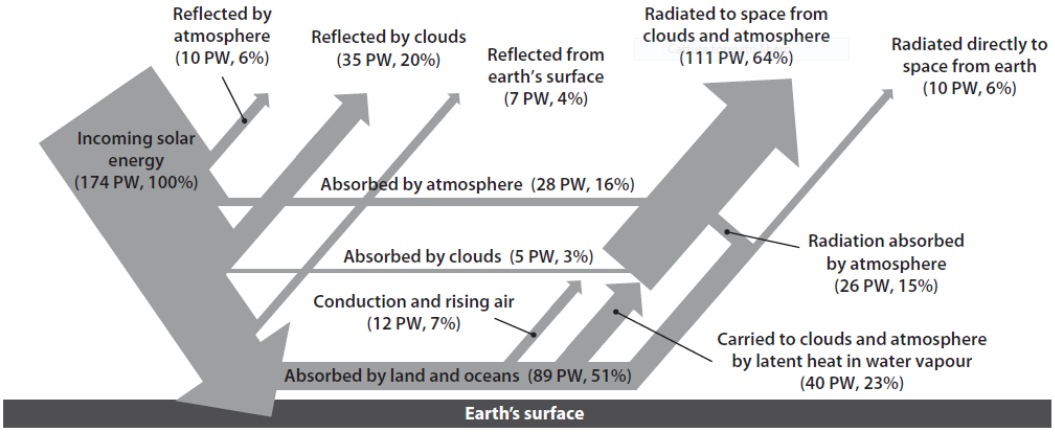

Figure 5 Solar energy balance on Earth [2]

As pictured in Figure 5, due to physical phenomena such as absorption, reflection and scattering that happen in atmosphere only a fraction of incoming sunlight actually reaches Earth surface. Moreover the sunlight that reaches the ground depends on other parameters like weather, seasonal variations and latitude [2], so there's a big variability on light intensity all around the world [20]. The most favourable zones are desert areas near the Equator.

Sunlight is composed of several kinds of electromagnetic radiations as pictured in Figure 6. The share of light intensity is the following: about 5% UV light ($\lambda < 400$ nm), 43,9% visible light ($400 < \lambda < 760$ nm) and 52,3% IR light ($\lambda > 760$ nm) [22].

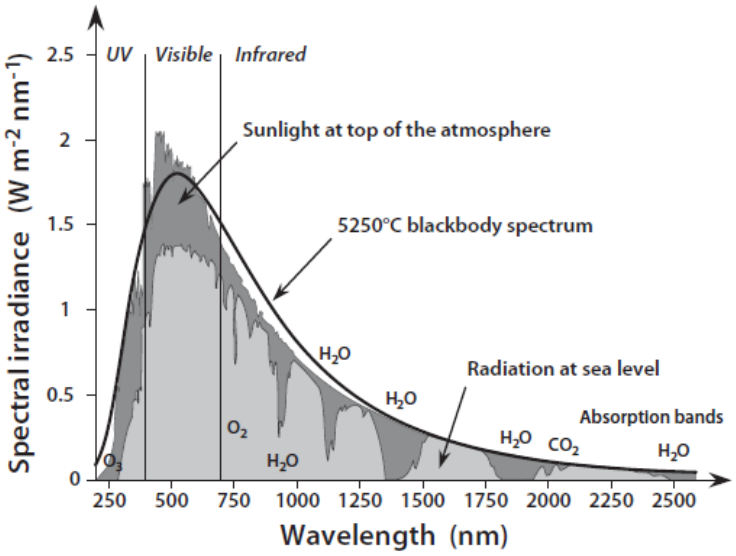

Figure 6 Sunlight spectra and absorption bands [2]

Solar energy is one of the most versatile renewables since it can be used for several purposes: photovoltaic (PV) systems for direct conversion to electric power [2,4,22,23]; thermal collectors for

heating [2,4,23] or concentrated solar power (CSP) for power generation [4,23,24]; photocatalytic or photoelectrochemical conversion systems for direct fuels production [22,25,26].

1.2.3 Renewables: drawn conclusions

This short overview shows the prospective of renewable energy for the future. It is expected that in 2060 one-third of TPES and half of electricity supply are supposed to derive from renewables [1]. Electricity is a versatile form of energy but the transportation sector is maybe the most reluctant to use electric energy. In 2014 only 1 % of total energy demand for transportation was supplied by electricity [1]. In the last seven years a huge development has happened in electric vehicles (EV): in 2015 1,26 million EVs were on the road while in 2010 only few thousand were used [28]. Nonetheless, as shown in Figure 7, fuelled vehicles are predicted to remain prevailing also in the next forty years.

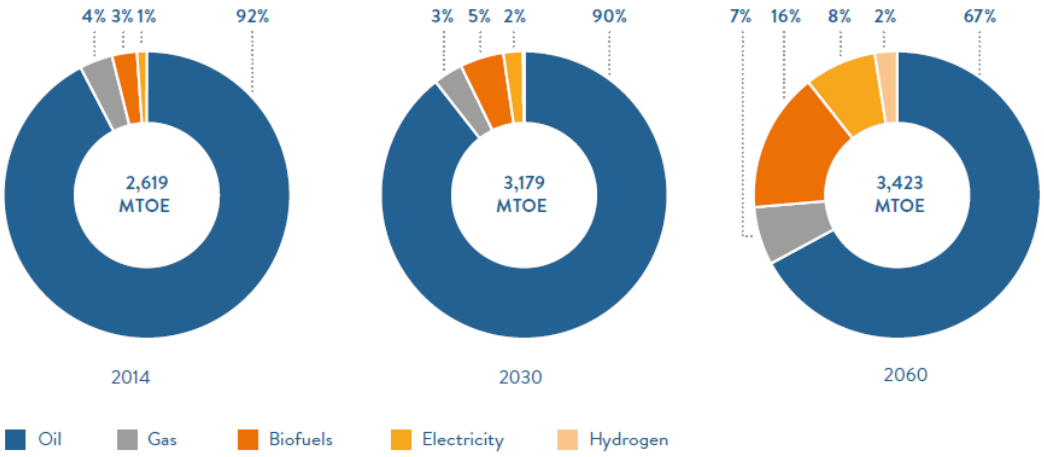

Figure 7 Energy share in transportation sector [1]

1.3. From Sun to biomass

1.3.1. Biomass: the origin

Another renewable energy source, not previously shown, is biomass. This energy derives from sunlight but is different from others since it is stored as chemical form. It was esteemed that 3,000 billion tonnes of organic carbon are stored worldwide as biomass [9]. Moreover it was assessed that 100 billion tonnes of dry biomass are produced every year by natural photosynthesis [2]. Natural photosynthesis efficiency is actually very low, only 1 % or less [2,29]. Nonetheless, the huge amount of solar energy income on the Earth leads to a remarkable biomass production.

1.3.2. First and second generation biomass

The first class of biofuels developed were the so-called first generation biofuels: biodiesel and bioethanol [31].

First generation bioethanol is produced from sugar crops such or starch crops [32]. Several microorganisms can convert simple sugars to alcohols (Equation 1): yeasts (*Saccharomyces cerevisiae*, *S. uvarum*, *Candida utilis*) and bacteria (*Zymomonas mobilis*) [32].

$$C_6H_{12}O_6 \rightarrow 2CO_2 + 2C_2H_5OH$$

Equation 1 Alcoholic fermentation of sugars (hexoses)

Since alcohol concentration, after fermentation, is low (lower than 110 g/L), it must be concentrated through distillation up to 95% v/v (azeotrope mixture) [32]. Then it must be dehydrated by technologies such as azeotropic distillation, adsorption, pressure swing distillation, pervaporation or solvent extraction [33]. Nonetheless, due to low ethanol concentration after fermentation, a huge amount of energy is needed in order to get concentrated ethanol, assessed to be up to 70-85% of energy demand in bio-refinery [34].

Research on first generation biofuels is nowadays of less interest mainly due to ethical reasons (the so-called food vs fuel debate) [31,38]. In 2015 about 1 billion tonnes of gasoline were consumed all around the world [4]: 2 billion m^3 of ethanol should replace fuel demand (calculated from energy and volumetric density of gasoline and ethanol [27]) and, using yield reported in Table 1, a cultivated area as large as arable land in USA [41] should be needed. This clearly shows that huge fertile-arable lands are needed, depriving land for food production.

	Maize	Sugarcane
Yield (m^3/ha)	6,2 [39]	4,2 [39]
GHGs emissions (g CO_2eq/MJ)	60 [39]	20 [39]
EROEI index	1,1-1,65 [40]	3-10 [40]

Table 1 Yield, EROEI index and GHGs for maize-derived and sugarcane-derived bioethanol

Moreover, as shown in Table 1, bioethanol production is not fully "carbon neutral" since a lot of steps in manufacturing process actually use fossil fuels. The energy needed, especially for corn-based crops, is very high compared to fossil fuels [3].

To overcome ethical, environmental and availability problems affecting first generation biofuels new source have been explored. The second generation biomass relies mainly on the so-called lignocellulosic biomass from forestry, sawmill and crops residues or the so called "energy crops" (both grasses or fast-growing trees) [31,38,42]. The lignocellulosic biomass is composed, as shown in Figure 8, mainly of three components: cellulose, a highly crystalline glucose-polymer; hemicellulose, a branched polymer composed of several sugars (e.g. glucose, xylose, arabinose); lignin, a complex amorphous polymer based on aromatic units, that improves waterproofing and microbial attack resistance [45]. Composition of biomass, both the share of three main component and composition of heteropolymers themselves (lignin and hemicellulose) is strongly affected by plant species and growing environment [29].

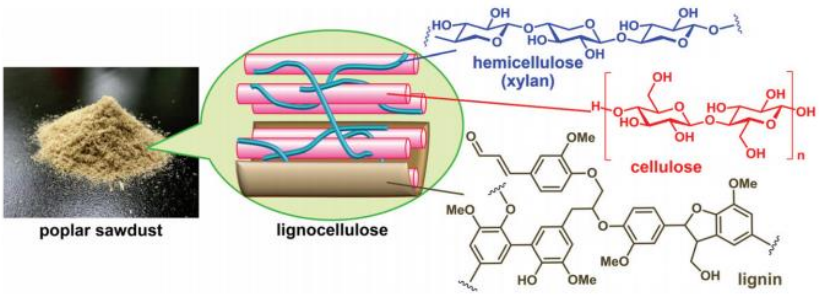

Figure 8 Lignocellulosic biomass structure and main components [44]

Several technologies are available to convert lignocellulose into valuable fuels. Thermo-chemical processes, namely gasification and pyrolysis, are maybe the simplest way to upgrade biomass to valuable gas (e.g. syngas) and liquid (bio-oil) products [30].

Biomass can be also upgraded by separation of main component eventually converting them into valuable products (fuels and/or chemicals). In this idea, lignocellulose must be first pre-treated to improve its degradability [47]. Then hemicellulose and cellulose have then to be hydrolysed into simple sugars (e.g. pentoses and hexoses) through enzymatic [48,49], homogeneous [48,50] or heterogeneous [50] acid-catalysed processes. Hexoses (C_6) and pentoses (C_5) obtained from the previous step can be transformed with either chemical and biochemical processes (Figure 9) into the so-called platform chemical, intermediate compounds that provide a huge variety of other substances for both fuel and chemical synthesis uses [44,51,52].

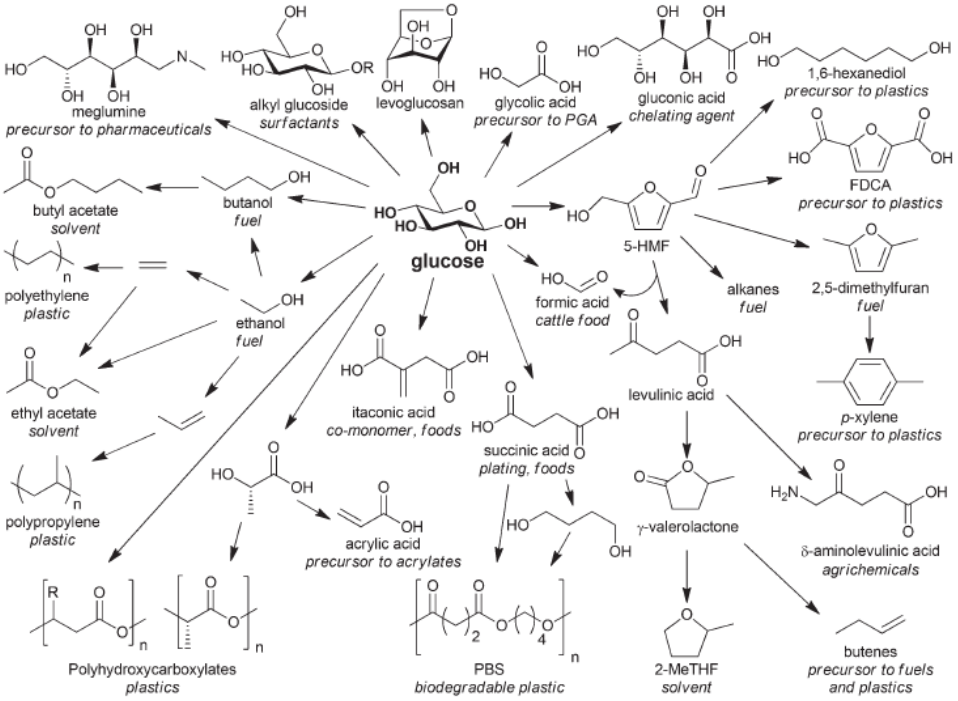

Figure 9 Glucose derivatives and their final utilisation [44]

Of particular interest in lignocellulose upgrading, is the conversion of agricultural waste [49,53] or energy crops (e.g. switchgrass) [54] to bioethanol, which is one of the most important biofuels as previously said. A part of pre-treatment and hydrolysis of polysaccharides, the process is basically the same of first-generation technology [32]. Cellulosic ethanol, besides the advantages of using non-food sources, is also more energy-saving than corn-based ethanol (EROEI index 4,4-11) [40] and can save up to 65% GHGs emissions in comparison to fossil-derived gasoline in internal combustion engines [55].

1.3.3. The biomass power: conclusion

The overall potential of biomass is still not clear: someone assesses that 100 EJ/y of lignocellulose waste is available [38], while others asses 251-1.272 EJ/y from surplus agricultural land and 150-153 EJ/y from agricultural and forestry waste [56]. A problem concerning biomass is its low energy density (0,1-1,2 W/m^2) compared to that needed by society (10-1.000 W/m^2) [2]: it has to be concentrated, simply meaning that it have to be collected from very large area.

Biomass is very promising as a source of fuels and chemicals, but technology competitive with fossil fuels still need further development. Moreover, a holistic point of view in this development (e.g. target molecule or compounds, chemical and engineering issues, economic, health and environment issues) should be taken in account [43]. Another interesting consideration concerning biomass upgrading is the emerging of non-hydrocarbon alternative fuels, that are usually oxygenated compounds such as the already mentioned bioethanol and biodiesel, but also new fuels like biobutanol or 2,5-dimethylfuran (DMF) [44].

1.4. The hydrogen economy

1.4.1. Hydrogen and fuel cells

Among the alternative non-hydrocarbon fuels, hydrogen is surely one of the most interesting since it yields only water as combustion product, it can be directly used in high energy efficient devices (fuel cells) and it can be made from renewables as it will be shown later [57]. The use of hydrogen as an alternative energy carrier, is named hydrogen economy [2,57].

A fuel cell is an electrochemical device in which fuel is supplied at anode, where oxidation occurs, while oxidant (air) is supplied at cathode where reduction occurs [2,22]. The overall reaction of hydrogen combustion (Equation 2), reported below, has a standard free energy (ΔG°) of 237,3 kJ/mol, which corresponds to a reversible standard potential (E°) of 1,23 V [58].

$$2H_2 + O_2 \rightarrow 2H_2O$$

Equation 2 Hydrogen combustion

The main advantage of fuel cells is the higher efficiency than other thermal engines (e.g. plug engines or steam turbine) [59]. Other advantages that can be mentioned are: mild operation conditions [58], modularity, static nature and low noisiness [59]. The most studied fuel cell is probably proton-exchange membrane fuel cell (PEMFC) that is the most interesting candidate for automotive uses and small-scale power generation [22]. A schematic picture is reported in Figure 10.

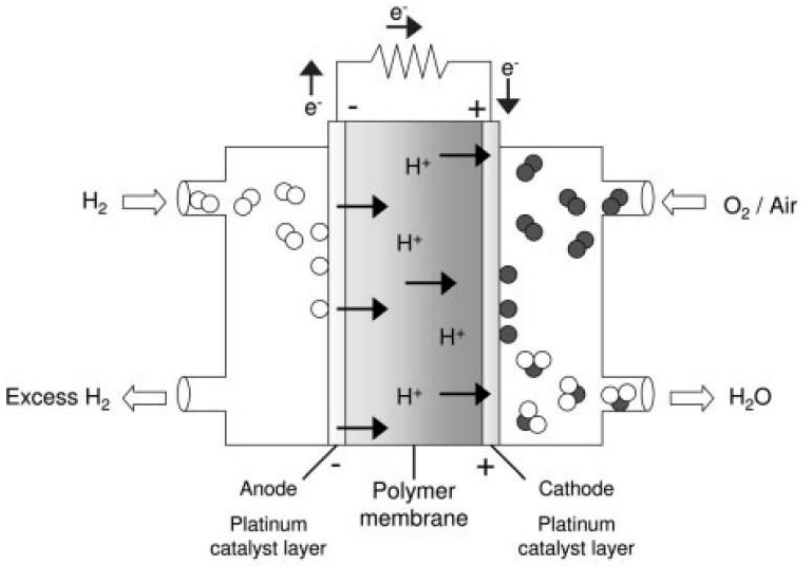

Figure 10 PEMFC scheme [57]

Unfortunately this kind of fuel cell has several drawbacks: expensive electrocatalyst material (Pt) [60] and its sensitivity to carbon monoxide poisoning [62]; expensiveness of solid electrolyte (Nafion) [57]; limited durability [60,63] and low power density compared with other engine [59]. Moreover the high cost of these devices (currently no less than 50 $/kW [61]) makes more attractive other technologies such as hybrid vehicles [57].

1.4.2. Storage problems

Another big problem relying hydrogen economy is its storage.

Fuel	Energy density (MJ/kg)	Energy density (MJ/L)
H_2 (298 K, 70 MPa)	119 [64]	4,7*
Liquid hydrogen (20 K, 0,1 MPa)	119 [64]	8,5 [64]
Ethanol	26,8 [27]	21,3 [27]
Diesel fuel	43 [27]	35,7 [27]
Gasoline	44 [27]	32,2 [27]
Compressed natural gas (293 K, 20 MPa)	50 [64]	8,2 [64]
Liquid natural gas	50 [64]	20,1 [64]

Table 2 Energy density of some fuels: a comparison (* calculated from density data reported in ref. [65])

Compression and liquefaction give low energy density compared with other fuels (Table 2), moreover special tank are needed (e.g. pressure withstanding or cryogenic tanks) and a lot of energy is required for both compression and liquefaction [57]. Several alternative hydrogen storage techniques have been developed [22,57,66], nevertheless none of these storage systems seems to be comparable to current used fuels. An interesting alternative seems indirect storage using fuels (e.g. alcohols) that can be converted to hydrogen through reforming processes [57,67] with good yields [65,67].

1.4.3. Hydrogen production: look to the future

Hydrogen is nowadays produced mainly from fossil fuels which account 96 % production capacity, mainly from natural gas (48 %) [68]. Currently about 50 million tonnes of hydrogen are produced every year [57] and mainly used in chemical industry and oil refining (Figure 11). Current hydrogen production corresponds to only 2% of TPES [57]. As previously shown, hydrogen does not seem to

become a widely used fuel in next future, nevertheless it should be an important means to upgrade biomass [44] and CO_2 [70] to valuable fuels and chemicals.

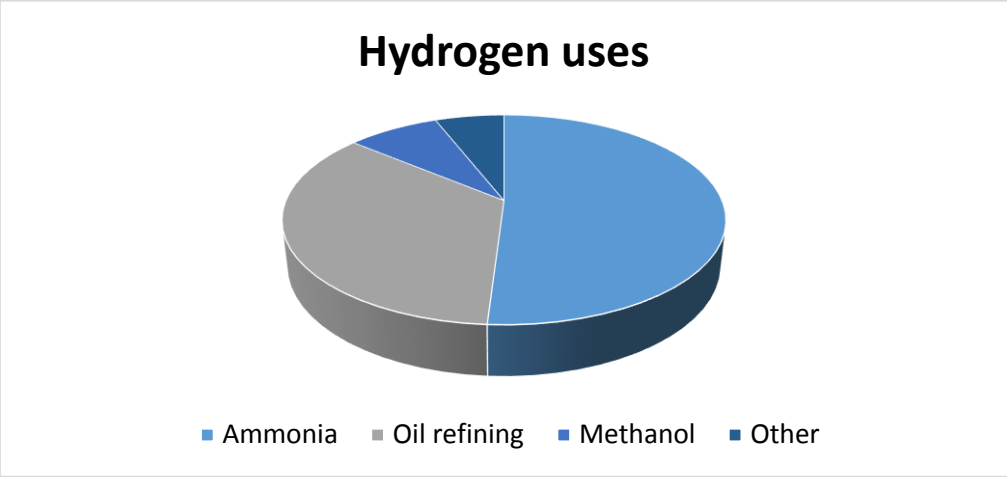

Figure 11 Hydrogen uses [57]

The conventional technology to produce hydrogen is methane steam-reforming (MSR) (Equation 3), that yields syngas, a hydrogen and carbon monoxide gaseous mixture.

$$CH_4 + H_2O \rightleftharpoons CO + 3H_2$$

Equation 3 Methane-steam reforming (MSR)

To improve hydrogen yield, water gas shift reaction (WGSR) (Equation 4) that convert carbon monoxide into carbon dioxide and hydrogen [46,71].

$$CO + H_2O \rightleftharpoons CO_2 + H_2$$

Equation 4 Water gas shift reaction (WGSR)

Water electrolysis is an interesting technology due to its high efficiency (58-87 %) [68] and pure hydrogen and oxygen obtained (> 99%) [69]. Nevertheless a lot of electric power, 4-6 kWh for 1 m^3 of H_2, is needed for this process [68], so its feasibility is correlated to cheap electricity supply. Only 4 % of hydrogen is produced by water electrolysis [57]. Currently, large MSR plants provide hydrogen at 1 $/kg, while current wind energy technology is assessed to produce hydrogen from water electrolysis at 6-7 $/kg, while solar PV at 28 $/kg [57]. It is clear that improvement on renewable technology are still needed.

1.4.4. Oxygenates reforming

An appealing method to couple sustainable hydrogen production and renewable biomass valorisation is oxygenate compounds reforming. Besides renewability and low GHGs emissions, reforming reaction with oxygenated biofuels are more suitable due to mild reaction conditions (lower temperature). Several substrates have been studied and several technologies are available [37].

The conventional steam-reforming (SR) reaction is one of the most studied and several biomass-derived feedstock can be used, such as methanol [72], ethanol [73], glycerol [74], and bio-oil [75]. Ethanol steam-reforming (ESR) is one of the most studied reaction [37]. Several reactions occur beside purely ethanol reforming [37,78], and some of them are unwanted like those yielding methane and carbon monoxide (selectivity losses), and coke formation (activity losses) [37]. ESR is performed at temperature of 250-950 °C [76], pressure close to 1 bar and steam-ethanol ratio of 3-13 [77], with several metal-supported catalysts based on either noble metals (Rh, Pt, Pd, Ir) or non-noble metals (Ni, Co, Cu) supported on different porous oxide (e.g. ZrO_2, CeO_2, $Ce_xZr_{1-x}O_2$, Y_2O_3) [76,77]. The main causes of activity losses are carbon deposition (coke) and metal sintering [37].

Another interesting reforming technology is aqueous phase reforming (APR), that operates lower temperature (220-270 °C) than SR, but higher pressure (250-300 bar). Moreover, those compounds cannot be vaporised (e.g. sugars) and water-rich feedstock can be directly used [79].

1.5. Photocatalytic approach to hydrogen: photoreforming

1.5.1. Photocatalysis: a brief overview

An interesting and alternative approach to get hydrogen is the direct photolysis of water since sunlight [20] and water are abundant and widespread all over the world. The huge research interest on photocatalysis started on Honda's and Fujishima's discovery that exposing a titanium dioxide crystal to UV light, it was able to split water into hydrogen and oxygen [80]. It was lately discovered that the addition of an organic compound in water rose considerably hydrogen yield [81]: since water acts indirectly as oxidant for organic compounds, the reaction has been recently named photoreforming [82].

Besides hydrogen production, photocatalysis offers other potentialities such as pollutant abatement [83] and water disinfection [84] by photooxidation, and solar fuels production by carbon dioxide photoreduction [26].

1.5.2. Semiconductors: fundamentals

Semiconductor, in the band-theory model, is a solid-state material in which the valence band (VB), orbitals where electrons are located in a non-excited system, is spaced by 1-6 eV from the conduction band (CB), empty orbitals where electrons can freely move upon excitation (Figure 12). The energy separation between the top of the valence band and the bottom of the conducting band, is called band-gap [85].

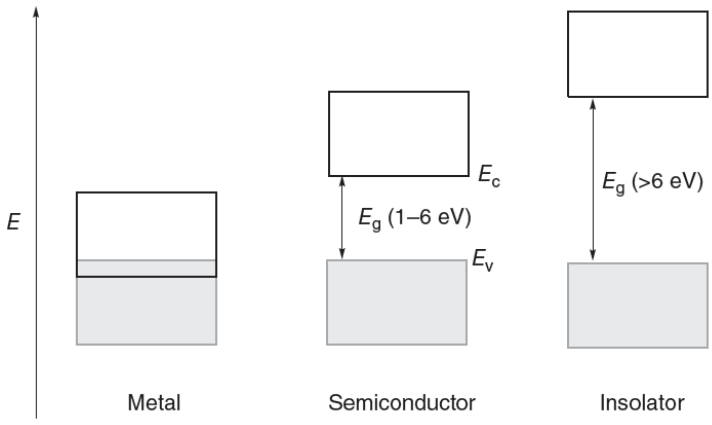

Figure 12 Band energy diagrams for metals (conductor), semiconductors and insulators [85]

Another important concept is Fermi level (E_F), defined as the energy at which there's 50 % of probability to find an electron and its position inside energy gap between CB and VB define

semiconductor nature as pictured in Figure 41. An n-type semiconductor has an E_F lying close to CB, and the so-called majority carrier are electrons, while a p-type has an E_F close to VB and majority carrier are holes [85]. This is due to creation of energy level inside the gap between CB and VB [23].

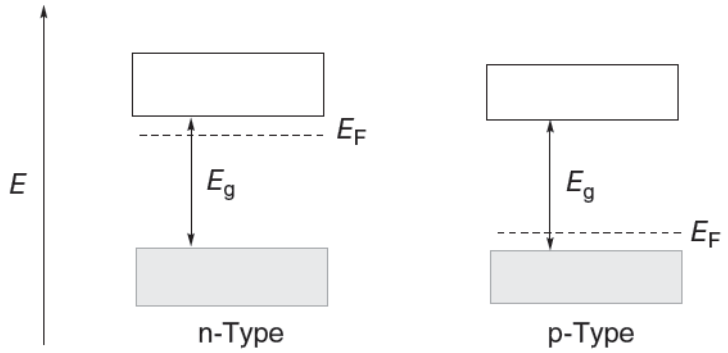

Figure 13 Band diagram of n-type and p-type semiconductor [85]

Upon absorption of a photon of identical or higher energy than bandgap, a very fast process (10^{-15} s) [83], an electron from VB is excited to CB, creating the so-called electron-hole pair [83]. Several phenomena can later occur, as reported in Figure 42: charge carrier recombination in the bulk (r), that dissipate energy as heat or light; diffusion of electron (s) and holes (t) to the surface where they can either recombine (q) or react with an electron acceptor or donor, respectively.

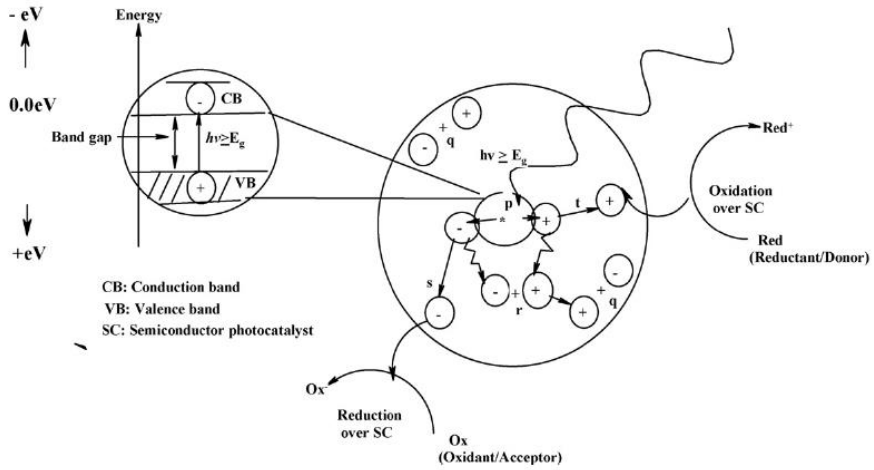

Figure 14 Mechanism of photocatalytic phenomenon [83]

Charge carrier recombination, a fast process (10^{-8}-10^{-7} s) [83], should be avoided and this can be achieved by choosing an indirect bandgap semiconductor [86,87], increasing surface/bulk trap ratio since bulk traps favour recombination while surface traps the interaction with reactants [88] and choosing a semiconductor with low effective mass [89]. Effective mass is a quantum property that

describes how fast a charge carrier (electron or hole) moves inside the semiconductor itself: the lower the effective mass, the faster the charge carrier movement [87].

1.5.3. Deep in the photoreforming reaction: mechanism

Upon excitation, electron is transferred to acceptor (proton) yielding hydrogen, while the hole extracts out an electron from the donor (organic compound), as reported in Figure 15. Charge carriers have different reactivity (charge transfer rate): holes react faster with acceptor (10^{-12}-10^{-9} s), while electron are slower to react (10^{-5}-10^{-3} s). This further improves charge carrier separation through fast holes consumption [82]. In order to transfer both charge carrier to reactant is essential that CB lies at higher energy (or more negative potential from a photoelectrochemical point of view) than electron acceptor, while VB lies at lower energy (more positive potential) than electron donor, thus allowing electron and holes flow [90]. Beside this thermodynamic requirement, it has been known than a higher energy gap between CB-electron acceptor or VB-electron donor, improves reaction rate [91].

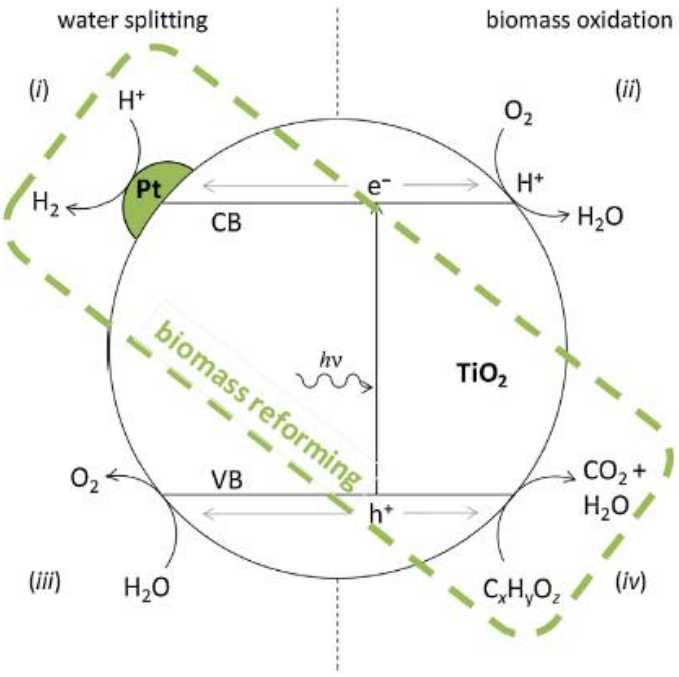

Figure 15 Semiconductor photocatalysis: charge carrier transfer [90]

It is known alcohols in presence of water, absorb onto a physisorbed layer of the latter at low temperature [94] eventually being oxidised by holes or surface-bonded hydroxyl radical (hole traps): the former is named direct oxidation, while the latter indirect oxidation [90]. It has been observed that direct or indirect mechanism path is affected by water/reactant ratio: the higher the water content,

the more probable is indirect (OH radical-mediated) path [95]. A generalised mechanism for oxidation pathway is proposed in Figure 16, where [ox] can be either a hole or a hydroxyl radical. Two main side-reaction can be seen: CO formation by aldehyde decarbonylation (that can desorb without being oxidised) and hydrocarbon formation through coupling of alkyl radical with hydrogen atom or another alkyl radical, thus lowering hydrogen yield.

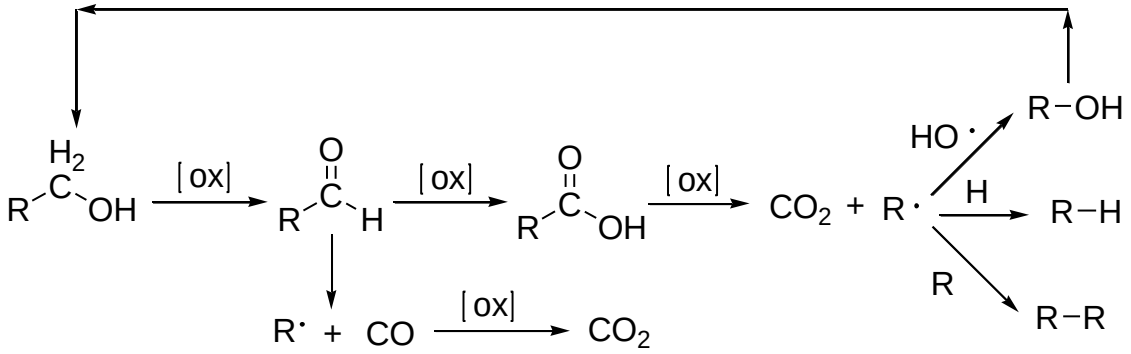

Figure 16 Generalised mechanism of oxidation pathway in photoreforming reaction [90,92]

Nevertheless a general mechanism was proposed, it's worthwhile to remind that the actual mechanism could be more complex since other side-reaction can afford unexpected by-product [93,97,98] and is also strongly dependent on used co-catalyst [99,100].

1.5.4. How do reaction parameters influence photoreforming reaction?

Reaction conditions in photoreforming (PR) have been proved to affect both yield and selectivity [90]. Light is one of the most important parameters since it is the energy source of a photocatalytic reaction. It is known that the lower the wavelength, the higher the hydrogen evolution [101] and the apparent quantum yield (AQY) [102]. The latter is defined as the ratio of electrons used for hydrogen reduction, in the assumption that one absorbed photon yield one excited electron, to the total amount of incident photons (Equation 5).

$$\Phi_a = \frac{n\ (transferred\ electrons)}{n\ (incident\ photons)} \cdot 100$$

Equation 5 Definition of apparent quantum yield (Φ_a) [90]

Concerning light intensity (or irradiance) the higher the irradiance, the lower the AQY [104] due to increasing electron-hole recombination rate [103] and scattering phenomena [90]. Although photocatalysis is a light-activated phenomenon, the temperature plays an important role in product desorption and diffusion [90]. It has been known that the higher the temperature, the higher the

hydrogen yield and reaction rate [97,98] and decreasing also some side-products [98]. Nonetheless an excessive increasing of temperature beyond a certain value, does not lead to further improvement of catalytic activity [97]. In general temperature lower than 90 °C are used [90], and further increases beyond 100 °C lead to a change in selectivity ascribed to a thermo-catalytic behaviour of the system [105].

Since photoreforming reaction needs water as a co-reactant, reagents concentration is another important parameter affecting the reaction. In general it has been observed that increasing reagent concentration, hydrogen yield is increased [97] up to a certain value beyond which a maximum activity is reached, then decreasing [95,106] or reaching a plateau [92]. Water/reactant ratio also affects selectivity, improving complete degradation to CO_2 at higher ratios [95]. The chemical structure of reagent plays an important role in activity and selectivity. Several compounds have been studied, and the most important are alcohols [90]. In general, the hydroxyl moieties improve hydrogen yield since α-hydrogens are reactive [86,99], while long alkyl chains reduce hydrogen yield and promote alkane formation (side reaction) [107]. It has been discovered that the more the number of α-hydrogen in simple alcohols molecule, the higher the hydrogen formation rate as pictured in Figure 17.

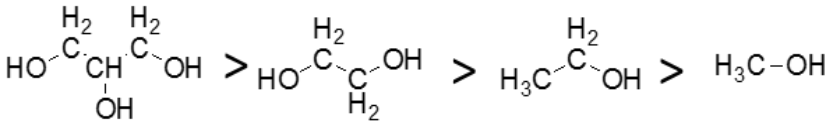

Figure 17 Influence of chemical structure on hydrogen evolution activity of simple alcohols [86]

1.5.5 Photocatalysts and co-catalyst

A photocatalyst must be, as previously said, a semiconductor material. The first and main used photocatalytic material is certainly titanium dioxide (TiO_2) [90,109]. Nevertheless several other materials can be used such as zinc oxide (ZnO) [110], strontium titanate ($SrTiO_3$) [111], calcium niobate ($Ca_2Nb_3O_{10}$) [112], sodium tantalate ($NaTaO_3$) [113], copper oxides (Cu_2O, CuO) [114], cobalt oxide (Co_3O_4) [115], bismuth-yttrium vanadates ($Bi_xY_{1-x}O_4$) [117], tantalum nitride (Ta_3N_5) [118], cadmium sulphide (CdS) [119], zinc-cadmium sulphide ($Zn_xCd_{1-x}S$) [120], graphene [121] and carbon-nitride [122]. In Figure 18 several oxide semiconductors with corresponding bandgap value and band-edge position are reported.

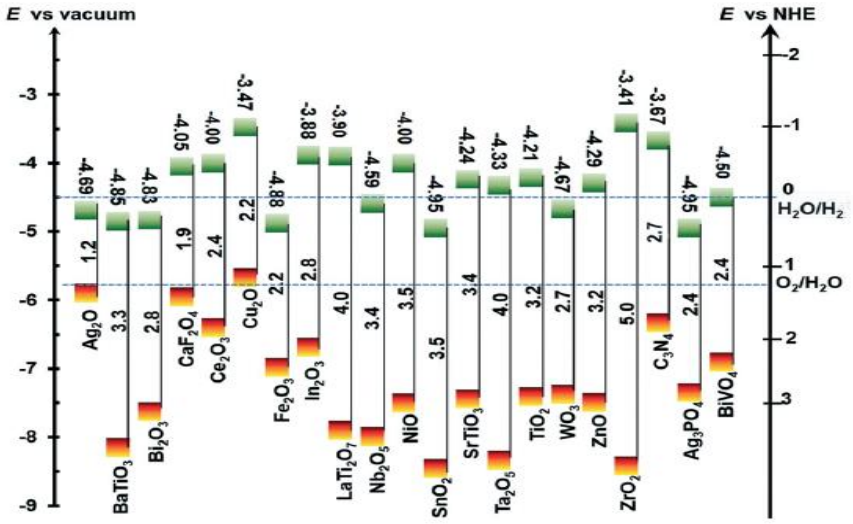

Figure 18 Bandgap and band edge position of several oxide semiconductors [25]

In order to improve photocatalytic performances of semiconductor, several strategies can be adopted. First, the morphology of catalytic nanomaterials plays an important role in order to get a good exposition to light source with low diffusion and reflection losses [91,123] and narrow path of the photogenerated charge carrier in order to avoid bulk recombination [82]. Thus morphology such as nanorod [124], nanowires [125], nanotubes [140] or mesoporous high-surface area material [126,139] are suitable for photocatalytic purposes.

Bandgap narrowing for wide bandgap materials can be performed with either non-metals [128] or metals ions [129]. The use of a dopant, modifies the electronic properties of the material inserting energy levels above the VB or below the CB and thus reducing the bandgap, depending on the dopant element as pictured in Figure 19. Anion doping is widely used [127] and nitrogen is the most used non-metal dopant [128,130].

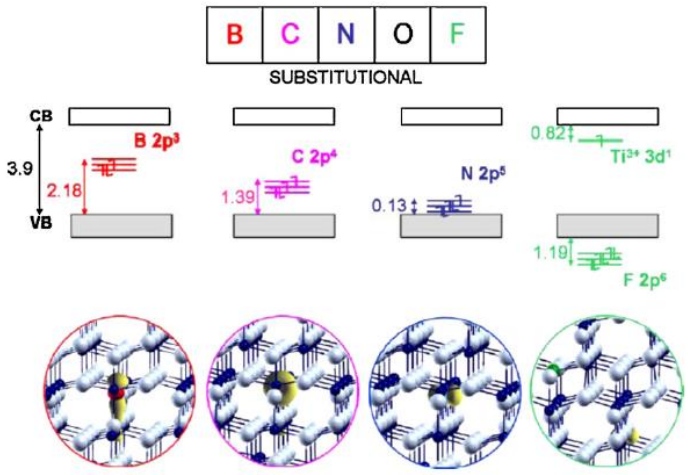

Figure 19 Non-metal substitutional doping in TiO_2 with first raw p-block elements [127]

Concerning metal doping, it has been known that nitrogen-metal co-doping gives good catalytic results due to synergic effect between nitrogen-doping (bandgap narrowing) and metal-doping (electron stabilisation) [131]. Visible light harvesting can also be performed coupling a wide band-gap semiconductor (e.g. TiO_2), acting as electron-receiver, to a second semiconductor with a narrow band-gap and more negative CB (e.g. CdS [133,134] or Cu_2O [135]), acting as visible-light harvester and getting a so-called heterojunction.

A co-catalyst added to the pristine photocatalyst improves remarkably its activity due to a dual role (Figure 20): on one hand acting as an electron-trap and thus improving electron-hole lifetime [90], on the other hand acting as a hydrogen-evolution site [104].

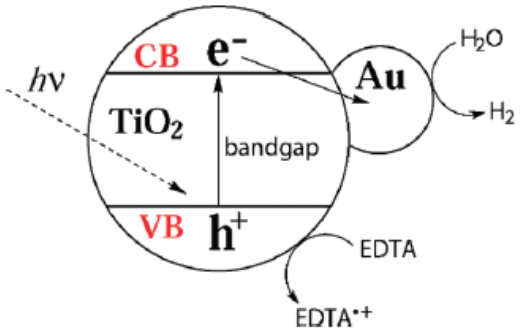

Figure 20 Effect of co-catalyst on photoreforming reaction [101]

On titanium dioxide, the addition of a co-catalyst boosts the activity of 1-2 order of magnitude [136,137]. The most used co-catalysts are noble metal such as palladium [99], platinum [108] and gold [100]. Platinum and palladium are reported to give better catalytic result than gold due to higher work function, related to electron-trapping capability [93] and lower activation energy, providing easier hydrogen

evolution [116]. Nonetheless gold is extensively studied due to visible light harvesting by the localised surface plasmon resonance (LSPR) [101]. Due to their low cost, of particular interest are non-noble metals such as copper and nickel [90]. Copper is certainly the most studied [138] in the form of both oxide [137] and metal [139]. Nickel is less studied [132,141,139] but very interesting due to C-C bond cleavage ability [142] and work function similar to palladium and platinum [132], thus improving charge separation. It has been known that loading of about 1% for both noble metals [143] and non-noble metals [137] give the highest catalytic activity since lower loading result in low trapping and hydrogen reduction sites, while higher loading results in decreasing light absorption by semiconductor and increased recombination centre [82]. Moreover the co-catalyst NPs size plays an important role in both activity [96,144] and selectivity [96].

1.5.6. Photoreforming: potentialities

Photoreforming can become a cheap and versatile process for hydrogen production in mild conditions from biomass. Ethanol is an interesting hydrogen source (Equation 6) since it can be viewed as both model substrate [98,143] and industrial feedstock derived from waste or energy-crops, (cellulosic ethanol). The gas phase conditions, that will be explained in the next chapter, seems to be more promising than liquid solution [136,145] but is still underdeveloped.

$$C_2H_5OH + 3H_2O \rightarrow 2CO_2 + 6H_2$$

$$\Delta G^0 = +\,137{,}6\ kJ/mol$$

Equation 6 Ethanol photoreforming reaction [90]

Potentialities wise, two prospects can be considered. On one hand, photoreforming allows direct storage of solar energy into molecular hydrogen chemical bond. Since solar energy is abundant and free, this process is more sustainable than state of the art thermo-catalytic ethanol SR which uses heat as energy source, usually by burning a fuel. On the other hand, ethanol could be a hydrogen storage media, convertible to hydrogen with an on-board reforming technology in transportation devices. In this case a more concentrated light source should be needed (e.g. a lamp or LEDs device), but low-temperature equipment would be required. Due to scarce fuel cell performances up to now, as previously, the latter can be viewed as a long-term prospect. The former seems to be more promising in the next future, especially as an alternative way to exploit solar energy.

Concluding, in the idea of a future technology for hydrogen production two main concepts must be considered: efficiency and sustainability. An efficient process is obviously a requirement for

industrial-scale application, meaning high hydrogen yield with cost as low as possible. A sustainable process is a key target for the future society in order to reduce environmental impact of human activities, as previously shown in section 1.1. In particular a whole picture point of view must be considered. This means besides a sustainable energy source, also the process itself (operative conditions) and the used material (e.g. catalyst) must be projected aiming sustainability.

The aim of this thesis work is to fulfil these goals (efficiency and sustainablility), through an integrated approach of process and catalysts development, those will be separately and extensively discussed in the next chapters.

1.6. References

1. World Energy Council website: https://www.worldenergy.org/wp-content/uploads/2016/10/World-Energy-Scenarios-2016_Full-Report.pdf
2. N. Armaroli, V. Balzani, Energy for a Sustainable World, Wiley-VCH 2011
3. D. J. Murphy, C. A. S. Hall, *Ann. N.Y. Acad. Sci.* 1185 (**2010**) 102-118
4. World Energy Council website: https://www.worldenergy.org/wp-content/uploads/2016/10/World-Energy-Resources-Full-report-2016.10.03.pdf
5. British Petroleum website: https://www.bp.com/content/dam/bp/pdf/energy-economics/statistical-review-2016/bp-statistical-review-of-world-energy-2016-full-report.pdf
6. G. Ertl, H. Knözinger, J. Weitkamp, Environmental Catalysis, Wiley-VCH 1999
7. C. Figueres, H.J. Schellnhuber, G. W. J. Rockström, A. Hobley, S. Rahmstorf, *Nature* 546 (**2017**) 593-595
8. International Energy Agency website: https://www.iea.org/publications/freepublications/publication/CO2EmissionsfromFuelCombustion_Highlights_2016.pdf
9. P. Falkowski, R. J. Scholes, E. Boyle, J. Canadell, D. Canfield, J. Elser, N. Gruber, K. Hibbard, P. Högberg, S. Linder, F. T. Mackenzie, B. Moore III, T. Pedersen, Y. Rosenthal, S. Seitzinger, V. Smetacek, W. Steffen *Science* 290 (**2000**) 291-296
10. Global Monitory Division of US National Oceanic and Atmospheric Administration: https://www.esrl.noaa.gov/gmd/trends/monthly.html
11. NASA website: https://climate.nasa.gov/vital-signs/carbon-dioxide/
12. Intergovernmental Panel on Climate Change website: https://www.ipcc.ch/pdf/assessment-report/ar4/syr/ar4_syr_full_report.pdf
13. S. A. Zimov, E. A. G. Schuur, F. S. Chapin III, *Science* 312 (**2006**) 1612-1613
14. M. Z. Jacobson, *J. Geophys. Res.* 110 (**2005**) 1-17
15. P. M. Cox, R. A. Betts, C. D. Jones, S. A. Spall, I. J. Totterdell, *Nature* 408 (**2000**) 184-187
16. International Atomic Energy Agency website: https://www.iaea.org/About/Policy/GC/GC60/GC60InfDocuments/English/gc60inf-2_en.pdf
17. B. K. Sovacool, *Energy Policy* 36 (**2008**) 2950-2963
18. J. K. Kaldellis, D. Zafirakis, *Renewable Energy* 36 (**2011**) 1887-1901
19. O. Ellabban, H. Abu-Rub, F. Blaabjerg, *Renew. Sustainable Energy Rev.* 39 (**2014**) 748-764
20. N. Kannan, D. Vakeesan, *Renew. Sustainable Energy Rev.* 62 (**2016**) 1092-1105
21. G. Kopp, J. L. Lean, *Geophys. Res. Lett.* 38 (**2011**) 1-7
22. B. Viswanathan, Energy Sources Fundamental of Chemical Conversion Processes and Applications, Elsevier 2016
23. K. Jägler, O. Isabella, A. H. M. Smets, R. A. C. M. M. van Swaaji, M. Zeman, Solar Energy Fundamentals, Technology, and System, Delft University of Technology 2014
24. H. L. Zhang, J. Baeyens, J. Degrève, G. Cacères, *Renew. Sustainable Energy Rev.* 22 (**2013**) 466-481
25. J. Li, N. Wu, *Catal. Sci. Technol.* 5 (**2015**) 1360-1384

26. Y. Ma, X. Wang, Y. Jia, X. Chen, H. Han, C. Li, *Chem. Rev.* 114 (**2014**) 9987-10043
27. G. Eng, I. Bywater, C. Hendtlass, New Zealand Energy Information Handbook 3rd ed., Caenz 2008
28. International Energy Agency website: https://www.iea.org/publications/freepublications/publication/Global_EV_Outlook_2016.pdf
29. P. McKendry, *Biores. Technol.* 83 (**2002**) 37-46
30. L. Zhang, C. Xu, P. Champagne, *Energy Convers. Maneg.* 51 (**2010**) 969-982
31. S.N. Naik , V. V. Goud, P. K. Rout, A. K. Dalai, *Renew. Sustainable Energy Rev.* 14 (**2010**) 578-597
32. N. Korisac, Z. Duvnjak, A. Frakas, H. Sahm, S. Bringer-Meyer, O. Goebel, D. Mayer, Ethanol, Ullmann's Encyclopedia of Industrial Chemistry, vol. 13, 334-397, Wiley-VCH 2012
33. A. K. Frolkova, V. M. Raeva, *Theor. Fund. Chem. En.* 44 (**2010**) 545-556
34. S. Zereshki, Distillation - Advances from Modeling to Applications, InTech 2012
35. F. Ma, M. A. Hanna, *Biores. Technol.* 70 (**1999**) 1-15
36. D. Y. C. Leung, X. Wu, M. K. H. Leung, *Appl. Energy* 87 (**2010**) 1083-1095
37. D. Li, X. Li, J. Gong, *Chem. Rev.* 116 (**2016**) 11529-11653
38. R. E. H. Sims, W. Mabee, J. N. Saddler, M. Taylor, *Biores. Technol.* 101 (**2010**) 1570-1580
39. C. L. Crago, M. Khanna, J. Barton, E. Giuliani, W. Amaral, *Energy Policy* 38 (**2010**) 7404–7415
40. B. D. Solomon, *Ann. N.Y. Acad. Sci.* 1185 (**2010**) 119–134
41. The World Bank website: http://data.worldbank.org/indicator/AG.LND.AGRI.K2
42. R. A. Lee, J. M. Lavoie, *Animal Frontiers* 3 (**2013**) 6-11
43. D. Yue, F. You, S. W. Snyder, *Comput. Chem. Eng.* 66 (**2014**) 36-56
44. H. Kobayashi, A. Fukuoka, *Green Chem.* 15 (**2013**) 1740-1763
45. P. Bajpai, Pretreatment of Lignocellulosic Biomass for Biofuel Production, Springer 2016
46. C. H. Bartholomew, R. J. Farrauto, Fundamentals of Industrial Catalytic Processes 2nd ed., John Wiley & sons, 2006
47. P. Kumar, D. M. Barrett, M. J. Delwiche, P. Stroeve, *Ind. Eng. Chem. Res.* 48 (**2009**) 3713-3729
48. F. M. Gìrio, C. Fonseca, F. Carvalheiro, L. C. Durte, S. Marques, R. Bogel-Łukasik, *Biores. Technol.* 101 (**2010**) 4775-4800
49. F. Talebdnia, D. Karakashev, I. Angelidaki, *Biores. Technol.* 101 (**2010**) 4744-4753
50. F. Guo, Z. Fang, C. C. Xu, R. L. Smith Jr, *Prog. Energy Combust. Sci.* 38 (**2012**) 672-690
51. K. Yan, C. Jarvis, J. Gu, Y. Yan. *Renew. Sustainable Energy Rev.* 51 (**2015**) 986-997
52. J. C. Serrano-Ruiz, R. Luque, J. M. Campelo, A. A. Romero, *Challenges* 3 (**2012**) 114-132
53. N. Sarkar, S. Kumar Ghosh, S. Bannerjee, K. Aikat, *Renewable Energy* 37 (**2012**) 19-27
54. K. David, A. J. Ragauskas, *Energy Environ. Sci.* 3 (**2010**) 1182-1190
55. Y. Bai, L. Luo, E. van der Voet, *Int. J. Life Cycle Asses.* 15 (**2010**) 468-477
56. H. Long, X. Li, H. Wang, J. Jia, *Renew. Sustainable Energy Rev.* 26 (**2013**) 344-352
57. G. A. Olah, A. Goeppert, G. K. S. Prakash, Beyond Oil and Gas: The Methanol Economy 2nd ed., Wiley-VCH 2009
58. I. Pilatowsky, R. J. Romero, C. A. Isaza, S. A. Gamboa, P. J. Sebastian, W. Rivera, Cogeneration Fuel Cell Air Conditioning Systems, Springer 2011

59. O. Z. Sharaf, M. F. Ohran, *Renew. Sustainable Energy Rev.* 32 (**2014**) 810-853
60. M. K. Debe, *Nature* 486 (**2012**) 43-51
61. A. Kraytsberg, Y. Ein-Eil, *Energy Fuels* 28 (**2014**) 7303-7330
62. J. J. Baschuk, X. Li, *Int. J. Energy Res.* 25 (**2001**) 695-713
63. L Dubau, L. Castanheira, F. Maillard, M. Chatenet, O. Lottin, G. Maranzana, J. Dillet, A. Lamibrac, J.-C. Perrin, E. Moukheiber, A. ElKaddouri, G. De Moor, C. Bas, L. Flandin, N. Caqué, *Energy Environ.* 3 (**2014**) 540-560
64. P. P. Edwards, V. L. Kuznetsov, W. I. F. David, N. P. Brandon, *Energy Policy* 36 (**2008**) 4356-4362
65. M. Hirscher, Handbook of Hydrogen Storage, Wiley-VCH 2010
66. E. David, *J. Mater. Process. Technol.* 162-163 (**2005**) 169-177
67. S. Golunski, *Energy Environ. Sci.* 3 (**2010**) 1918-1923
68. R. B. Gupta, Hydrogen Fuel: Production, Transport and Storage, CRC Press 2009
69. W. J. Buttner, M. B. Post, R. Burgess, C. Rivkin, *Int. J. Hydrogen Energy* 36 (**2011**) 2462-2470
70. A. Goeppert, M. Czaun, J.-P. Jones, G. K. S. Prakash, G. A. Olah, *Chem. Soc. Rev.* 43 (**2014**) 7995-804
71. P. Häussinger, R. Lohmüller, A. M. Watson, Hydrogen, 2. Production, vol. 18, 251-304, Wiley-VCH 2012
72. D. R. Palo, R. A Dagle, J. D. Holladay, *Chem. Rev.* 107 (**2007**) 3992-4021
73. A. Haryanato, S. Fernando, N. Murali, S. Adhikari, *Energy & Fuels* 19 (**2005**) 2098-2106
74. C. A. Schwengber, H. J. Alves, R. A. Schaffner, F. A. Silva, R. Sequinel, V. R. Bach, R. J. Ferracin, *Renew. Sustainable Energy Rev.* 58 (**2016**) 259-266
75. R. Trane, S. Dahl, M. S. Skjøth-Rasmussen, A. D. Jensen, *Int. J. Hydrogen Energy* 37 (**2012**) 6447-6472
76. J. L. Contreras, J. Salmones, J. A. Colìn-Luna, L. Nuño, B. Quintana, I. Còrdova, B. Zeifert, C. Tapia, G. A. Fuentes, *Int. J. Hydrogen Energy* 39 (**2014**) 18835-18853
77. M. Ni, D. Y. C. Leung, M. K. H. Leung, *Int. J. Hydrogen Energy* 32 (**2007**) 3238-3247
78. P. Bichon, G. Haugom, H. J. Venvik, A. Holmen, E. A. Blekkan, *Top. Catal.* 49 (**2008**) 38-45
79. J. D. Holladay, J. Hu, D. L. King, Y. Wang, *Catal. Today* 139 (**2009**) 244-260
80. A. Fujishima, K. Honda, *Nature* 238 (**1972**) 37-38
81. T. Kawai, T. Sakata, *Nature* 286 (**1980**) 474-476
82. I. Rossetti, ISRN Chemical Engineering 2012
83. U. I. Gaya, A. H. Abdullah, *J. Photochem. Photobiol.*, C 9 (**2008**) 1-12
84. S. Malato, M. I. I. Maldonado, P. Fernández-Ibáñez, I. Oller, I. Polo, R. Sánchez-Moreno, *Mater. Sci. Semicond. Process.* 42 (**2016**) 15-23
85. H. Kisch, Semiconductor Photocatalysis, Wiley-VCH 2015
86. W.-T. Chen, A. Chan, Z. H.N. Al-Azri, A. G. Dosado, M. A. Nadeem, D. Sun-Waterhouse, H. Idriss, G. I.N. Waterhouse, *J. Catal* 329 (**2015**) 499-513
87. J. Zhang, P. Zhou, J. Liu, J. Yu, *Phys. Chem. Chem. Phys.* 16 (**2014**) 20382-20386
88. J. Yan, G. Wu, N. Guan, L. Li, Z. Li, X. Cao, *Phys. Chem. Chem. Phys.* 15 (**2013**) 10978-10988
89. K. V. Baiju, K. S. Sandhya, J. James, K. G. Warrier, *Phys. Chem. Chem. Phys.* 111 (**2007**) 7612-7622
90. A. V. Puga, *Coord. Chem. Rev.* 315 (**2016**) 1-66
91. B. Han, Y. H. Hu, *J. Phys. Chem. C* 119 (**2015**) 18972-18934

92. X. Fu, J. Long, X. Wang, D. Y. C. Leung, Z. Ding, L. Wu, Z. Zhang, Z. Li, X. Fu, *Int. J. Hydrogen Energy* 33 (**2008**) 6484-6491
93. G. Chiarello, M. H. Aguirre, E. Selli, *J. Catal.* 273 (**2010**) 182-190
94. A. Y. Nosaka, T. Fujiwara, H. Yagi, H. Akutsu, Y. Nosaka, *Langmuir* 19 (**2003**) 1935-1937
95. G. Chiarello, D. Ferri, E. Selli, *J. Catal.* 280 (**2011**) 168-177
96. G. Wu, T. Chen, W. Su, G. Zhou, X. Zong, Z. Lei, C. Li, *Int. J. Hydrogen Energy* 33 (**2008**) 1243-1251
97. V. M. Daskalaki, D. I. Kondarides, *Catal. Today* 144 (**2009**) 75-80
98. E. Taboada, I. Angurell, J. Llorca, *J. Catal.* 309 (**2014**) 460-467
99. H. Bahruji, M. Bowker, P. R. Davies, F. Pedrono, *Appl. Catal., A* 107 (**2011**) 205-209
100. M. Bowker, L. Millard, J. Greaves, D. James, J. Soares, *Gold Bullietin* 37 (**2004**) 170-173
101. C. G. Silva, R. Juàrez, T. Marino, R. Molinari, H. Garcìa, *J. Am. Chem. Soc.* 133 (**2011**) 595-602
102. H. Yoshida, K. Hirao, J. Nishimoto, K. Shimura, S. Kato, H. Itoh, T. Hattori, *J. Phys. Chem. C* 112 (**2008**) 5541-5551
103. L. Yang, Z. Liu, *Energy Convers. Manege.* 48 (**2007**) 882-889
104. F. H. Hussein, R. Rudham, *J. Chem. Soc., Faraday Trans.* 83 (**1987**) 1631-1639
105. A Caravaca, H. Daly, M. Smith, A. Mills, S. Chansai, C. Hardacre, *React. Chem. Eng.* 1 (**2016**) 649-657
106. Y. Wu, G. Lu, S. Li, *Catal. Lett.* 133 (**2009**) 97-105
107. H. Bahruji, M. Bowker, P. R. Davies, L. S. Al-Mazroai, A. Dickinson, J. Greaves, D. James, L. Millard, F. Pedrono, *J. Photochem. Photobiol., A* 216 (**2010**) 115-118
108. D. I. Kondarides, V. M. Daskalaki, A. Patsoura, X. E. Verykios, *Catal. Lett.* 122 (**2008**) 26-32
109. X. Chen, S. S. Mao, *Chem. Rev.* 107 (**2007**) 2891-2959
110. R. Lv, X. Wang, W. Lv, Y. Xu, Y. Ge, H. He, G. Li, X. Wu, X. Li, Q. Li, *J. Chem. Technol. Biotechnol.* 90 (**2015**) 550-558
111. B. Zieliñska, E. Borowiak-Palen, R. J. Kalenczuk, *Int. J. Hydrogen Energy* 33 (**2008**) 1797-1802
112. Y. Ebina, A. Tanaka, J. N. Kondo, K. Domen, *Chem. Mater.* 8 (**1996**) 2534-2538
113. X. Fu, X. Wang, D. Y. C. Leung, W. Xue, Z. Ding, X. Huang, X. Fu, *Catal. Commun.* 12 (**2010**) 184-187
114. D. Barreca, P. Fornasiero, A. Gasparotto, V. Gombac, C. Maccato, T. Montini, E. Tondello, *Chem. Sus. Chem.* 2 (**2009**) 230-233
115. A. Gasparotto, D. Barreca, D. Bekermann, A. Devi, R. A. Fischer, P. Fornasiero, V. Gombac, O. I. Lebedev, C. Maccato, T. Montini, G. Van Tendeloo, E. Tondello, *J. Am. Chem. Soc.* 133 (**2011**) 19362-19365
116. A. Tanaka, K. Hashimoto, H. Kominami, *J. Am. Chem. Soc.* 136 (**2014**) 586-589
117. D. Jing, M. Liu, J. Shi, W. Tang, L. Guo, *Catal. Commun.* 12 (**2010**) 264-267
118. Y. Luo, X. Liu, X. Tang, Y. Luo, Q. Zeng, X. Deng, S. Ding, Y. Sun, *J. Mater. Chem., A* 2 (**2014**) 14927-14939
119. R. Peng, C.-M. Wu, J. Baltrusaitis, N. M. Dimitrijevic, T. Rajh, R. T. Koodali, *Chem. Commun.* 49 (**2013**) 3221-3223
120. S. Peng, M. Ding, T. Yi, Z. Zhan, Y. Li, *Environ. Prog. Sustain.* 35 (**2014**) 141-148
121. C. Lavorato, A. Primo, R. Molinari, H. Garcia, *Chem. Eur. J.* 20 (**2014**) 187-194
122. S. Ye, R. Wang, M.-Z. Wu, Y.-P. Yuan, *Appl. Surf. Sci.* 358 (**2015**) 15-27
123. Y.-J- Hwang, A. Boukai, P. Yang, *Nano Lett.* 9 (**2008**) 410-415

124. Y.V. Kolen'ko, K. A. Kovnir, A. I. Gavrilov, A. V. Garshev, J. Frantti, O. I. Lebedev, B. R. Churagulov, G. Van Tendeloo, M. Yoshimura, *J. Phys. Chem. B* 110 (**2006**) 4030-4038
125. J. Jitputti, Y. Suzuki, S. Yoshikawa, *Catal. Commun.* 9 (**2008**) 1265–1271
126. T. Sreethawong, Y. Suzuki, S. Yoshikawa, *J. Solid State Chem.* 178 (**2005**) 329–338
127. M. V. Dozzi, E. Selli, *J. Photochem. Photobiol., C* 14 (**2013**) 13-28
128. R. Ashai, T. Morikawa, T. Ohwaki, K. Aoki, Y. Taga, *Science* 293 (**2001**) 269-271
129. D. Dovoranová, V. Brezová, M. Mazúr, M. A. Malati, *Appl. Catal., B* 37 (**2002**) 91–105
130. R. Asahi, T. Morikawa, H. Irie, T. Ohwaki, *Chem. Rev.* 114 (**2014**) 9824−9852
131. S. Taylor, M. Mehta, A. Samokhvalov, *Chem. Phys. Chem.* 15 (**2014**) 942-949
132. E. P. Melián, M. N. Suáreza, T. Jardiel, J. M. D. Rodrígueza, A.C. Caballero, J. Araña, D.G. Calatayud, O. G. Díaz, *Appl. Catal., B* 152–153 (**2014**) 192–201
133. V. M. Daskalaki, M. Antoniadou, G. Li Puma, D. I. Kondarides, P. Lianos, *Environ. Sci. Technol.* 44 (**2010**) 7200-7205
134. T. Kida, G. Guan, N. Yamada, T. Ma, K. Kimura, A. Yoshida, *Int. J. Hydrogen Energy* 29 (**2004**) 269 – 274
135. L. Li, L. Xu, W. Shi, J. Guan, *Int. J. Hydrogen Energy* 38 (**2013**) 816-822
136. G. L. Chiarello, L. Forni, E. Selli, *Catal. Today* 144 (**2009**) 69–74
137. J. Yu, Y. Hai, M. Jaroniec, *J. Colloid Interface Sci.* 357 (**2011**) 223–228
138. L. Clarizia, D. Spasiano, I. Di Somma, R. Marotta, R. Andreozzi, D. D. Dionysiou, *Int. J. Hydrogen Energy* 39 (**2014**) 1681-1683
139. A. V. Korzhak, N. I. Ermokhina, A. L. Stroyuk, V. K. Bukhtiyarov, A. E. Raevskaya, V. I. Litvin, S. Ya. Kuchmiy, V. G. Ilyin, P. A. Manorik, *J. Photochem. Photobiol., A* 198 (**2008**) 126–134
140. S. Zhang, B. Peng, S. Yang, H. Wang, H. Yu, Y. Fang, F. Peng, *Int. J. Hydrogen Energy* 40 (**2015**) 303-310
141. W.-T. Chen, A. Chan, D. Sun-Waterhouse, T. Moriga, H. Idriss, G. I. N. Waterhouse, *J. Catal.* 326 (**2015**) 43-53
142. R. R. Davda, J.W. Shabaker, G.W. Huber, R.D. Cortright1 , J.A. Dumesic, *Appl. Catal., B* 56 (**2005**) 171–186
143. A. V. Puga, A. Forneli, H. García, A. Corma, *Adv. Funct. Mater.* 24 (**2014**) 241-248
144. W.-T. Chen, V. Jovic, D. Sun-Waterhouse, H. Idriss, G. I. N. Waterhouse, *Int. J. Hydrogen Energy* 38 (**2013**) 15036-15048
145. C. Ampelli, C. Genovese, R. Passalacqua, S. Perathoner, G. Centi, *Appl. Therm. Eng.* 70 (**2014**) 1270-1275

2. Reaction equipment

2.2 The gas phase conditions and reactor design: a brief introduction

The photoreforming reaction is usually carried out in liquid phase in slurry-type batch reactor, so using catalysts directly in powdered form [1-3]. Unfortunately, these liquid phase systems have several drawbacks such as high light scattering [145], mass transfer limitations [4] and leaching phenomena of co-catalyst [5].

Speaking of the gas phase, few literature reports have been reported [7-10], restricted to volatile or gaseous compounds like methanol [10], ethanol [7] and methane [11]. Nonetheless gas phase conditions have several advantages with respect to liquid ones. First because a higher hydrogen evolution rate than liquid systems, reported to be 20% higher by Ampelli *et al.* [145] and 30% higher by Chiarello *et al.* [10], due to low scattering phenomenon [145] which have been known to heavily affect efficiency of photocatalytic devices [12]. Moreover, gas-phase reactors allows a good irradiation pattern, easier scale-up, easier product recovery and no leaching problems [145].

Concerning ratios between the reagents (organic substrate and water), it has been known that low substrate/water ratio favours complete mineralisation of the substrate (high selectivity to photoreforming) but lower hydrogen yield [6,7]. At very high substrate/water ratios Chiarello *et al.* reported a plateau followed by a decreasing of hydrogen yield for methanol [6], while Taboada *et al.* reported a continuous increasing hydrogen production from ethanol, although a complete degradation is not reached in any case [7].

Besides simple choice of the reaction medium, the reactor configuration plays an important role since photocatalytic reactions are affected by photon and mass transfer limitations, those in turn are affected by catalyst and reactor design themselves [13]. The fluidised bed reactor (FBR), pictured in Figure 21, a configuration widely used in oil refining [46], allows high throughput but it is difficult to control, require system for catalyst's recovery (e.g. cyclones) [13] and dilution with inert particles, like silica beads, is needed in order to obtain a good fluidisation [14].

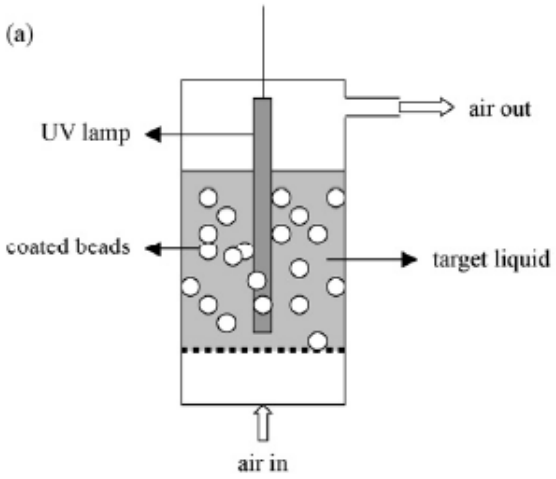

Figure 21 FBR configuration [4]

Moving to photoreactors those don't require catalyst separation, namely fixed-bed reactors, several configurations exist [13,16]. Plate type are the simplest configuration, consisting of a photocatalyst immobilised usually on a flat surface (Figure 22,a). Drawbacks like poor photon utilisation (e.g. due to scattering losses), low surface/volume ratio [17] and low throughput makes it unsuitable for industrial-scale application [13]. Annular type (Figure 22,b) basically consist of two concentric cylinder in which the inner wall of the outer ones is coated with photocatalyst, allowing a good irradiation of the catalyst [17] but, as for plate type, it is unsuitable to high throughput. However, plate-type and annular-type are suitable for kinetic studies [13]. Packed-bed type (Figure 22,c) are simple to set up [13], needn't catalyst immobilisation on wall and are one of the most used configuration on industrial scale for conventional thermo-catalytic reactions [46]. Nevertheless, besides classical high pressure drop [46], a light intensity radial gradient affect catalytic activity [13]. Monolith type (Figure 22) are very promising due to high throughput, low pressure drop and easy scaling-up but good irradiation of inner side of channel is the main drawbacks [4,16]. Moreover, mass transfer can affect monolith's catalytic performance [4].

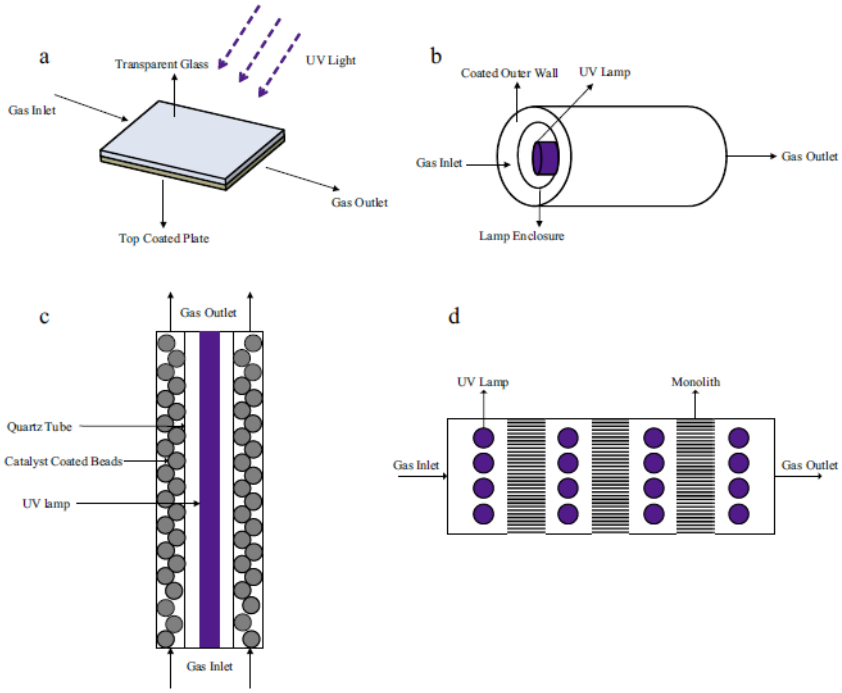

Figure 22 Main types of gas-phase photocatalytic reactor: coated plate (a), annular (b), packed-bed (c) and monolith (top view) (d) [13]

Comparing packed-bed and plate-type, two of the most common configurations, previous work reported by this research group shown an increase of about 3 order of magnitude of photocatalytic activity in plate-type with respect to packed-bed, due to better irradiation of the catalyst's surface [18,19].

Concerning the light transfer, a transparent wall coated with a catalyst's layer on one side shows two possible configuration. The "back-irradiation", in which the light have to travel through the transparent material (e.g. glass) and the catalyst's layer before reaching the outer surface where photocatalytic reaction occurs (Figure 23), while "front-irradiation" is the direct irradiation, so from "reagent side" of the just cited surface [4]. The latter is the preferred since no absorption, through the catalyst's layer, occurs [4].

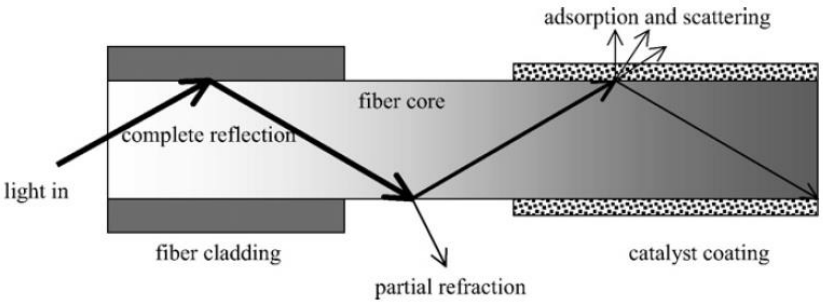

Figure 23 "Back-irradiation" in coated optical fibres [4]

Reactor configurations that use irradiated photocatalytic surfaces, namely plate, annular and monolith types, need an immobilisation process of catalyst on the surface itself that can be made of several material such as glass [145], steel [20] or ceramic material [7]. The photocatalyst can be anchored from finished powder through incipient wetness [21] or electrophoretic method [13,22] from a suspension of the catalysts. These techniques are relatively simple and work in mild conditions [21], so they are more eco-friendly. Sol-gel process [7,22] and chemical vapour deposition (CVD) [16,22] are more sophisticated techniques, often requiring high temperature treatment (i.e. sol-gel derived-material calcination and thermal decomposition of CDV precursors) [16] and specific equipment (e.g. CVD) [22] . Nonetheless they allow a strong catalyst-support interaction, namely chemical bonds, and a good quality supported material can be obtained [22].

Concluding a multi-parametric approach is required in photocatalytic process development. Besides catalyst design shown in section 1.5.5, several factors must be taken in account:

- Reactants ratios
- Light harvesting improvement
- Mass transfer enhancement
- Easy catalyst immobilisation
- Overall process flexibility

2.2. Aim

Ethanol was chosen as biomass-like model substrate, as renewable hydrogen source. Moreover an ethanol-water mixture was used instead of pure ethanol due to several reason:

- Water acts as an oxidant in photoreforming reaction [23]
- Water improves proton transfer on catalyst' surface from oxidising site to reducing site [24]
- Ethanol distillation requires a lot of energy [34], so the use of raw bioethanol or diluted ethanol is energy-saving

In this chapter the development of a lab-made rig for ethanol photoreforming is reported and discussed. Many variables affect photocatalytic reaction, as shown in section 1.5.4 and 2.1.1. Thus, an assessment is needed to evaluate the best operative conditions, carefully considering also sustainability (e.g. low operative temperature).

In order to simplify this evaluation, some variables remained unchanged through these preliminary tests (reaction configuration, light wavelength and intensity) while only most crucial parameters were assessed (gas flow and composition).

2.3. Equipment and materials

2.3.1. Photoreforming reaction rig

The scheme of photoreforming reaction equipment is reported in Figure 24. A Brooks mass flow controller is used to control carrier inert gas flow (helium). The ethanol-water vapour mixture is produced by bubbling the carrier through a temperature-controlled saturator, filled with 40 mL of a 35% v/v ethanol-water solution. The reaction is carried out in a fixed-bed thin-film photoreactor, made of borate glass ($\lambda_{cut\ off}$ = 300 nm [26]) with a volume of about 0,6 cm^3 and an exposed surface (one-side) of about 6 cm^2. The thin-film was prepared by deposition of a suspension of 10 mg powdered catalyst in 2-propanol [19], then drying the film at 110°C for 1 hour in order to remove all organic compounds. A 125 W medium-pressure mercury lamp with an emission range of 315-400 nm (31700-25000 cm^{-1}) purchased from Helios Italquartz, equipped with a 350 nm cut-off optical filter, and a main emission peak at 365 nm (27400 cm^{-1}) [28], was used as light source. The light intensity or irradiance is set to 50 W/m^2 and controlled with a Delta Ohm HD 2302.0 photo-radiometer and a LP 417 probe. Both saturator and photoreactor settings are equipped with two three-way valves and a bypass loop.

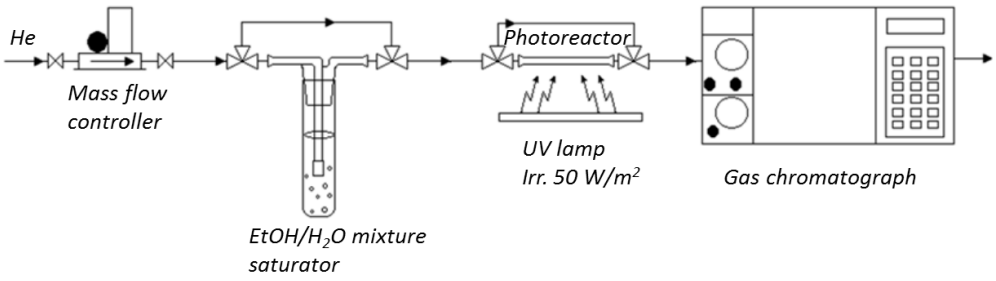

Figure 24 Lab-scale photoreforming reaction rig

The gas flow was analysed with a HP 5890 gaschromatograph equipped with two packed columns (2 m long) filled with Parapak Q (80-100 mesh), a ethylvinylbenzene-divinylbenzene copolymer, and molecular sieves (70-80 mesh), made of zeolites. The former allows analysis of organic compounds, carbon dioxide and water, while the latter allows separation of light non-polar gases (H_2, CH_4, CO) [29]. The injection is performed with a C-10WE valve, to inject 250 µL of gas in the instrument and

providing the switch of injected gas from the Porapak Q column to the MS column. Helium was used as a carrier gas, with a 30 mL/min flow.

The following programmed temperature was identified to achieve a good separation of analytes:

- 35°C for 2,2 min
- 35°C → 45 °C, rate 70 °C/min
- 45°C for 2,5 min
- 45°C → 55°C, rate 70°C/min
- 55°C for 10 min
- 55°C → 150°C, rate 70°C/min
- 150°C for 7,5 min

Analyte signal was recorded with a TCD detector. Calibration curves of reagents (H_2O, ethanol), expected products (H_2, CO_2, CO, CH_4, acetaldehyde, acetone) [7,145,31] and oxygen, that can arise from pure-water photolysis, were done separately and used for components quantification of flowing gas, while retention times (t_R) were used to identify the substances.

2.3.2. Materials

- Ethanol (assay > 99,8%) Honeywell
- 2-propanol (assay > 99,7%) VWR
- P25, Evonik

2.4. Result and discussion

2.4.1. Gas phase composition assessment

A photocatalytic reaction requires three components: reagents, light and a photocatalyst. Nevertheless side-processes can happen: photochemical reaction, catalytic reaction and catalyst decomposition. In order to exclude interference by these processes on the reaction, blank tests were performed on:

- Irradiated reaction mixture
- Reaction mixture on thin-film catalyst without irradiation
- Irradiated catalyst without reaction mixture

In all the cases, no substances other than ethanol and water were detected, meaning that a true photocatalytic phenomenon happens. Eventually a reaction test was run on pure water vapour with the conditions previously used in order to possibly compare activity on pure water photolysis with respect to photoreforming. Neither hydrogen nor oxygen were detected, meaning that in the current condition the system is inefficient for pure water photolysis.

Proceeding further, water/ethanol ratio was assessed. No literature is available concerning vapour phase composition of ethanol-water mixture below their boiling point, thus it was evaluated by putting a known mixture in the saturator and analysing the gas flow composition at different temperature. To reduce losses in reproducibility, piping was heated to 100°C (avoiding condensation phenomena) and measurement was carried out in irradiated empty reactor, where lamp is used as a heat source. This trick can be used since no photochemical reaction occurs in these reaction conditions, as previously proved.

A 35% v/v of ethanol in water (1:6 molar ratio) was chosen. This concentration represents a compromise between raw bioethanol (10% v/v or 1:29 molar ratio) and stoichiometric value (1:3 molar ratio). The composition of vapours at 40°C, 50°C and 60°C were evaluated and results are reported in Figure 25.

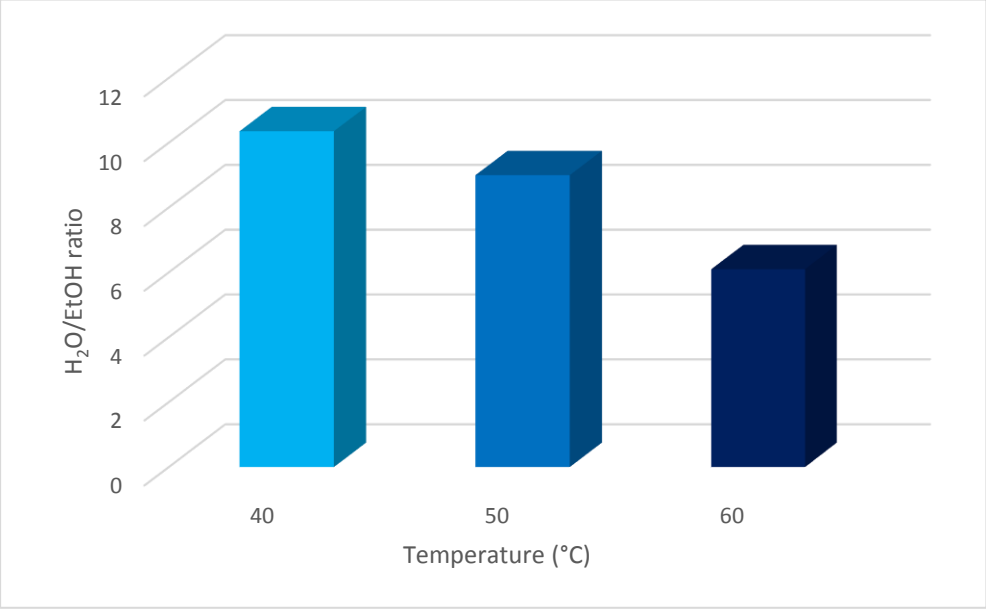

Figure 25 Ethanol concentration and water/ethanol ratio of 35% v/v mixture at different temperature

The optimal temperature was found to be 60°C, because the closest water/ethanol ratio to stoichiometric ratio (3:1). No further improvement of temperature was evaluated since in order to get a more sustainable process, temperature as low as possible should be used to save energy

requirement. Further tests assessed a water/ethanol ratio of 3,9 ± 0,8 and an ethanol concentration of 11 ± 1%.

These conditions were obtained in relatively mild conditions, thus fulfilling the sustainability goal. Moreover, a water/ethanol ratio close to stoichiometric allows on one hand an efficient use of reactants (e.g. an excess of one reagent requires further separation of unreacted compounds). On the other hand lower energy consumption to vaporise the mixture, since enthalpy of vaporisation of ethanol is lower than water [30].

2.4.2. Gas phase flow assessment

After evaluation of best gas phase composition (ethanol concentration and water/ethanol ratio), other conditions need to be optimised. Two of the most common reactor designs are plate-type thin film and packed bed (section 2.1.1.), reported in Figure 26. Briefly the first one is basically an empty glass container in which the photocatalyst is immobilised on wall in the form of thin film. The second is a glass hollow cylinder completely filled with catalyst particles of suitable size. Plate type thin-film design, as previously shown, has been proven to improve catalytic activity of three magnitude orders since a better exposition of the catalyst to light improves remarkably its activity. Moreover, a low amount of catalyst is required: 10 mg [19] instead of 400 mg [18].

Figure 26 Plate-type thin-film photoreactor (left) and packed-bed photoreactor (right)

Concerning light source an irradiance of 50 W/m^2 was chosen for two reason: on one hand since it represents the share of UV in sunlight, on the other hand low irradiance allows higher quantum

yield. If too much photons reach the catalyst's surface, electron-hole recombination wastes an increasing share of absorbed photon (section 1.5.4).

Gas flow affects the reaction behaviour in a continuous process, since it is correlated to space velocity (SV) and contact time (τ). They were calculated as reported in Equation 7 and Equation 8, where v_0 is the measured volumetric flow and V the reactor volume.

$$SV = \frac{v_0}{V}$$

Equation 7 Space velocity [46]

$$\tau = \frac{V}{v_0}$$

Equation 8 Contact time [46]

Starting from those reported in literature, a measured flow of 1,49 ± 0,06 mL/min was assessed to give the highest catalytic activity. It correspond to a space velocity of 149 ± 6 h^{-1} and a contact time of 24 ± 0,9 s. This is unfortunately the lowest flow possible with used mass flow controller.

2.5. Conclusion

A reaction rig was set up and reaction conditions optimised, getting a suitable process to study photocatalysts for photoreforming reaction.

Care was taken in order to operate in conditions as mild as possible, aiming to sustainability. In particular, temperature as low as possible was used (60°C) to yield water-ethanol vapours with a suitable composition, namely close to stoichiometric. Besides sustainability, conditions that allows hydrogen yield as high as possible was investigated, in particular reactor design, light intensity and gas flow. The first and the second variables was set unchanged, choosing a plate-type thin-film photoreactor and a low light intensity in order to get a more efficient photon utilisation. Moreover, lower amount of catalyst required makes the system less expensive and more sustainable with respect to a packed-bed reactor. The third variable was evaluated in order to get a suitable contact time in the reactor, aiming hydrogen yield as high as possible.

2.6. References

1. V. M. Daskalaki, D. I. Kondarides, *Catal. Today* 144 (**2007**) 75-80
2. L. S. Al-Mazroai, M. Bowker, P. Davies, A. Dickinson, J. Greaves, D. James, L. Millard, *Catal. Today* 122 (**2007**) 46- 50
3. X. Fu, J. Long, X. Wang, D. Y. C. Leung, Z. Ding, L. Wu, Z. Zhang, Z. Li, X. Fu, *Int. J. Hydrogen Energy* 33 (**2008**) 6484-6491
4. T. Van Gerven, G. Mul, J. Moulijn, A. Stankiewicz, *Chem. Eng. Process.* 46 (**2007**) 781-789
5. T. Montini, V. Gombac, L. Sordelli, J. J. Delgado, X. Chen, G. Adami, P. Fornasiero, *ChemCatChem* 3 (**2011**) 574-577
6. G. L. Chiarello, M. H. Aguirre, E. Selli, J. Catal. 273 (**2010**) 182-190
7. E. Taboada, I. Angurell, J. Llorca, *J. Catal.* 309 (**2014**) 460-467
8. C. Ampelli, C. Genovese, R. Passalacqua, S. Perathoner, G. Centi, *Appl. Therm. Eng.* 70 (**2014**) 1270-1275
9. A Caravaca, H. Daly, M. Smith, A. Mills, S. Chansai, C. Hardacre, *React. Chem. Eng.* 1 (**2016**) 649-657
10. G. L. Chiarello, L. Forni, E. Selli, *Catal. Today* 144 (**2009**) 69–74
11. H. Yoshida, K. Hirao, J. Nishimoto, K. Shimura, S. Kato, H. Itoh, T. Hattori, *J. Phys. Chem. C* 112 (**2008**) 5542-5551
12. B. Han, Y. H. Hu, *J. Phys. Chem. C* 119 (**2015**) 18972-18934
13. *Y.* Boyjoo, H. Sun, J. Liu, V. K. Pareek, S. Wang, *Chem. Eng. J.* 310 (**2017**) 537-559
14. M. Hajaghazadeh, V. Vaiano, D. Sannino, H. Kakooei, R. Sotudeh-Gharebagh, P. Ciambelli, *Catal. Today* 230 (**2014**) 79-84
15. C. H. Bartholomew, R. J. Farrauto, Fundamentals of Industrial Catalytic Processes 2nd ed., John Wiley & sons, 2006
16. O. Ola, M. Maroto-Valer, *J. Photochem. Photobiol., C* 24 (**2015**) 16-42
17. S. Das, W. M. A. W. Daud, *Renew. Sustainable Energy Rev.* 39 (2014) 765–805
18. A. Olivo, V. Trevisan, E. Ghedini, F. Pinna, C.L. Bianchi, A. Naldoni, G. Cruciani, M. Signoretto, *J. CO_2 Utiliz.* 12 (**2015**) 86-94
19. A. Olivo, E. Ghedini, M. Signoretto, M. Compagnoni, I. Rossetti, *Energies* 10 (**2017**) 1394
20. C. Passalía, O. M. Alfano, R. J. Brandi, *J. Hazard. Mater.* 211-212 (**2012**) 357-365
21. F. Thevenet, C. Guillard, A. Rousseau, *Chem. Eng. J.* 244 (**2014**) 50-58
22. A. Y. Shan, T. I. M. Ghazi, S. A. Rashid, *Appl. Catal., A* 389 (**2010**) 1-8
23. A. V. Puga, *Coord. Chem. Rev.* 315 (**2016**) 1-66
24. G. L. Chiarello, D. Ferri, E. Selli, *J. Catal.* 280 (**2011**) 168–177
25. S. Zereshki, Distillation - Advances from Modeling to Applications, InTech 2012
26. Hamamatsu website: https://www.hamamatsu.com/jp/en/support/glossary/w/index.html
27. S. Malato, M. I. I. Maldonado, P. Fernández-Ibáñez, I. Oller, I. Polo, R. Sánchez-Moreno, *Mater. Sci. Semicond. Process.* 42 (**2016**) 15-23
28. Helios Italquartz website: http://www.heliosquartz.com/prodotti/mercury-medium-pressure-uv-lamps/?lang=en

29. M. Ali Mohd, Advanced Gas Chromatography – Progress in Agricoltural, Biomedical and Industrial Application, InTech 2012
30. G. Baysinger, L. I. Berger, R. N. Goldberg, H. V. Kehiaian, K. Kuchitsu, G. Rosenblatt, D. L. Roth, D. Zwillinger, Handbook of Chemistry and Physics, CRC press 2005
31. A. V. Puga, A. Forneli. H. García, A. Corma, *Adv. Funct. Mater.* 24 (**2014**) 241-248

3. Photocatalyst development: synthesis, characterisation and reactivity test

3.1. The photocatalyst: an introduction

3.1.1. Titanium dioxide

Titanium is a very abundant element in Earth surfaces [4] and 6,6 million tonnes of ores (mainly ilmenite and rutile) were produced in 2016, while reserves are assessed to 830 million tonnes [5]. Titanium dioxide is an inorganic material widely used as a white pigment due to its remarkable scattering properties, chemical stability and non-toxicity [1]. It is used in sunscreens, toothpastes [2] and catalyst supports [3] too. Besides conventional uses, titanium dioxide has promising applications in photovoltaics, electrochromic devices, gas sensors [2], anti-cancer treatment, anti-fogging or self-cleaning coatings (based on superhydrophilicity of titanium dioxide) [6] and obviously photocatalysis for environmental remediation [7,8] or fuels production [26].

Due to its availability, chemical stability [6], high carrier mobility (in comparison to other semiconductors) [10] and limited toxicity [11], titanium dioxide is the most studied photocatalytic material and wide literature is available regarding synthesis, characterisation and utilisation [2]. Moreover, as reported in Figure 27, titanium dioxide has a sufficiently negative CB (– 0,5 V [24]) to reduce hydrogen (E° = 0,0 V) and a sufficiently positive VB (+ 2,7 V [24]) to oxidise several substrates, among which ethanol (E° = + 0,084 V).

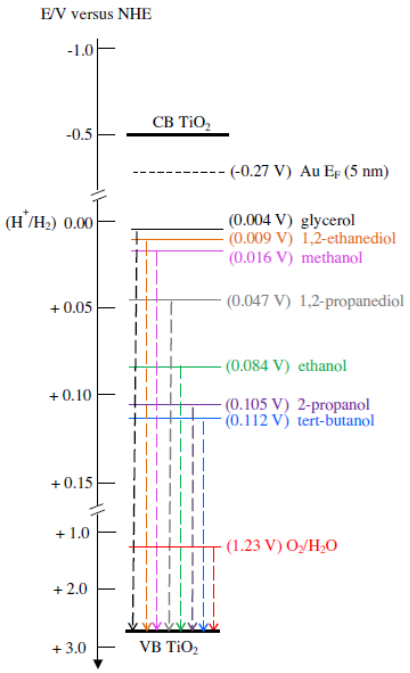

Figure 27 Redox potential of several electron-donor substances compared to anatase CB and VB [12]

Titanium dioxide exists in three main crystalline phases: anatase, rutile and brookite. These can be seen as TiO_6^{8-} octahedral units assembled in different ways, as shown in Figure 28.

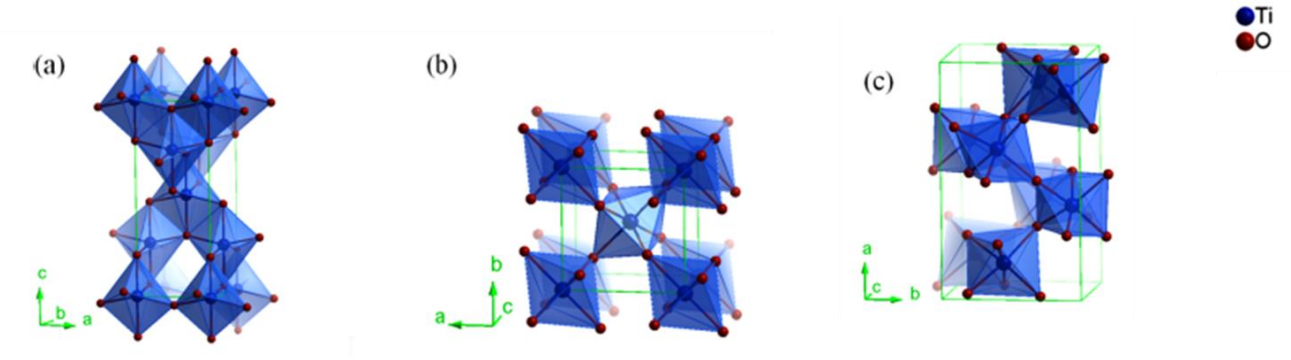

Figure 28 Titanium dioxide crystal phases: rutile (a), anatase (b) and brookite (c) [26]

The polymorphs have the same chemical composition, but differ for physical properties such as lattice parameters [26], bandgap [13], average crystal size [14] and electronic structure [15]. In particular the bandgaps of three polymorphs are 3,0 eV for rutile [16]; 3,21 eV for anatase [16] and 3,13-3,3 eV for brookite [13,16]. Among the three polymorphs anatase is the most active due to lower charge carrier recombination ascribing to higher surface defects [10,20], indirect bandgap and small charge carrier effective mass [15]. Moreover a more negative CB, allows higher reducing power of excited electrons [16]. Besides polymorph choice, other considerations must be taken in account. High crystallinity, high-surface area and small crystallite size improve catalytic activity by reducing carriers recombination probability and increasing adsorption capacity of reactant [22]. A careful tuning of preparation conditions (i.e. calcination temperature, Figure 28) allows a material with good photocatalytic properties.

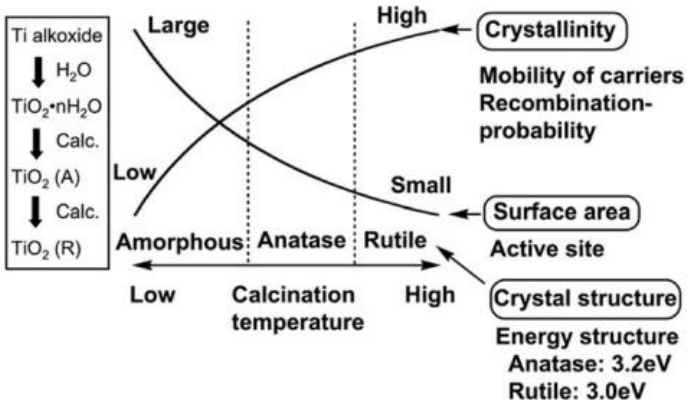

Figure 29 Influence of calcination temperature on surface area and crystallinity of the raw TiO_2 [22]

Another factor that must be considered, is the simultaneous presence of more than one crystal phase creating a so-called heterojunction. The most famous is surely the anatase-rutile heterojunction since it composes the benchmark material P25 (Evonik) [23]. The higher activity observed from this material [24] can be attributed to the charge separation through the junction, thus improving carriers' life [25].

Precipitation is an interesting alternative to other techniques (e.g. sol-gel), widely used in industrial practice for catalyst manufacturing [41] and can afford high-surface area material [42]. During precipitation, two steps are involved: nucleation and growth. These are affected by several operative conditions such as pH, temperature, reagents, method of precipitation, ageing step, so a careful control of the process is needed to obtain a suitable and reproducible material [41]. Tuning these conditions allows materials with different properties such as surface area, pore size, crystal phase, crystallite size, crystallinity, and degree of hydroxylation of surface [35]. As previously said, these properties affect in turn photocatalytic behaviour.

Eventually, speaking of sustainability, although titanium salts [43] are generally more expensive than titanium alkoxides [44,45], but precipitation technique can be seen more eco-friendly than sol-gel process on several point of view. First, the synthesis process requires only water as a solvent [42], while the sol-gel needs an organic solvent [27] and/or organic additives (i.e. acetylacetone) [19]. Precipitation by-products such as sodium sulphate and ammonium sulphate (depending on the precipitating agent) are inert non-toxic salt and can be recovered for other uses, such as is done in other industrial processes [46,47]. Second, sol-gel precursors are produced from titanium tetrachloride [48] which is a reactive liquid hard to handle. Moreover, its production requires harsh conditions and high-grade ores while titanyl sulphate is produced through a slightly safer process [1].

3.1.2. A cheap co-catalyst: copper

As shown in section 1.5., a co-catalyst is required to improve both hydrogen yield and apparent quantum yield. Noble metals are very active [23] but also expensive: 48 $/g for gold, 30 $/g for platinum and 29 $/g for palladium (September 2017) [50]. Non-noble metals like copper and nickel are very promising because their catalytic activity is comparable to noble metals [39,51,145], with the big advantage of very low cost (6,4 $/kg for Cu and 10,8 $/kg for Ni metals, September 2017 [50]), three order of magnitude cheaper than noble ones.

Copper is used as co-catalyst in its three oxidation states, mainly as metallic copper (Cu^0), copper (I) oxide (Cu_2O) and copper(II) oxide (CuO). Cu_2O is actually a visible light-harvester semiconductor rather than a co-catalyst, because its narrower bandgap (2,1 eV) and more negative CB than titania [56,57]. Copper metal [32] and CuO [40] are instead true co-catalysts, acting as both electron-trap and hydrogen evolution sites (Figure 30).

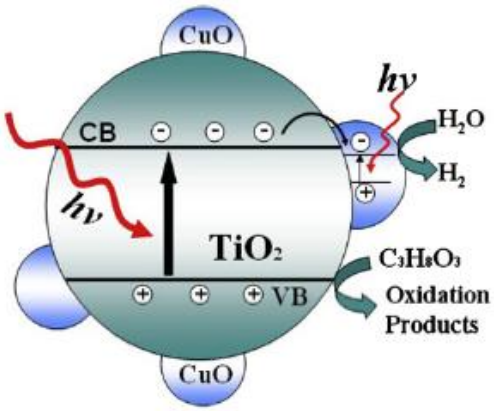

Figure 30 Mechanism of CuO/TiO_2 photoreforming [40]

CuO can be easily prepared from its precursors without any reduction step and/or reducing agent [40], have an higher work function (5,2-5,6 eV) [58] than copper (4,65 eV) [16], meaning that electrons can be easier stabilised [28] and, in contrast to Cu [60], is stable upon air exposure. However, copper(II) oxide is required to be nano-sized to be catalytically active [40], not only to improve its dispersion but also to rise CB, through quantum confinement effect [61], toward a more negative potential than H/H^+ couple as shown in Figure 31 thus allowing hydrogen reduction.

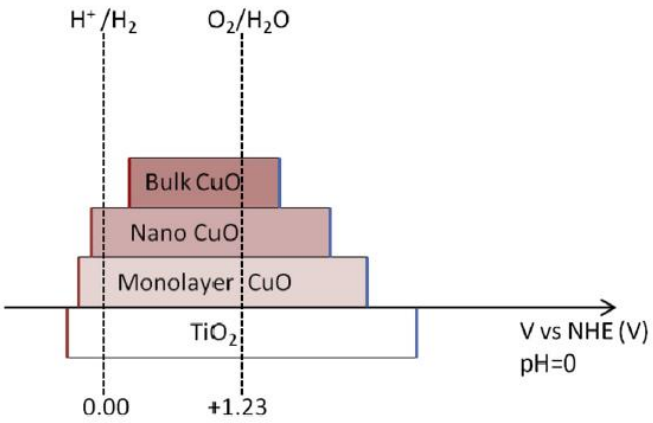

Figure 31 Quantum size effects on CuO-promoted TiO_2 [53]

Copper(II) oxide-promoted photocatalyst can be prepared mainly through two techniques: impregnation, both wet [40,62] and incipient wetness [36], and deposition-precipitation technique (DP) [51,62]. The latter is a method to obtain highly dispersed metal or oxide particles on a support [41]. Conventional impregnation technique allows to obtain small CuO nanoparticles (2-4 nm), detectable with transmission electron microscopy (TEM) [40]. The DP method seems to yield a thinner nanomaterial, namely a CuO monolayer, undetectable with TEM [51], but known to be more active than impregnated catalyst [62].

The key idea of DP is a gradual nucleation of an insoluble compound onto the support (e.g. through a slow increase of precipitating agent concentration), thus permitting high dispersion of this compound [63]. The addition of an organic chelating agent [62] probably delays precipitation [65] thus further improving gradual nucleation. Nonetheless only glycerol has been used as ligand until now [51,62] and no information about effect of different DP ligands on catalytic activity are now available, in particular compounds with different moieties than glycerol's hydroxyl groups (e.g. carboxylic group).

3.2. Aim

Catalyst design plays obviously a central role in photocatalytic processes development. In this chapter two kinds of TiO_2-based material will be chosen: a benchmark material (P25) and a lab-made high-surface area material, throughout precipitation technique. Then, choosing CuO as cheap co-catalyst, two different techniques will be used for its introduction in each TiO_2-based material promotion, namely wetness impregnation and DP technique. Furthermore two ligands that weren't previously reported in literature for such DP technique, will be used: citric acid and 1,3-propanediol.

These ligands have different moieties (carboxylic and hydroxyl groups, respectively), and they can be produced from biomass by biochemical (both) or chemical (1,3-propanediol) processes [66,67]. Starting from the best conditions identified in the previous chapter, it will be evaluated the effect of percentage of metal, introduction technique and effect of the semiconductor-pristine material on catalytic activity and selectivity. Eventually photocatalysts will be characterised in order to get a correlation between catalytic behaviour and physicochemical properties.

3.3. Experimental section

3.3.1. Synthesis of TiO_2 photocatalytic material

3.3.1.1. Reagents

- Titanium(IV) oxysulphate sulphuric acid hydrate $TiOSO_4 \cdot xH_2O \cdot yH_2SO_4$ (Ti assay > 29%) Sigma Aldrich
- Sodium hydroxide NaOH (assay > 97%), Carlo Erba
- Copper nitrate trihydrate $Cu(NO_3)_2 \cdot 3H_2O$ (assay > 99%), Sigma Aldrich
- 1,3-propanediol $HO(CH_2)_3OH$ (assay > 98%), Sigma Aldrich
- Citric acid monohydrate $HOC(COOH)(CH_2COOH)_2 \cdot H_2O$ (assay > 99%), Sigma Aldrich
- P25, Evonik
- Deionised water

3.3.1.2. Precipitated TiO_2

The precipitation was performed following a procedure previously optimised in this research group [81]. In a 250 mL beaker, 34,5 g of titanium oxysulphate were dissolved in 100 mL of deionised water, under vigorous magnetic stirring upon complete dissolution of the salt. A NaOH 9 M solution was prepared concurrently. The precipitation was performed with the equipment reported in Figure 32.

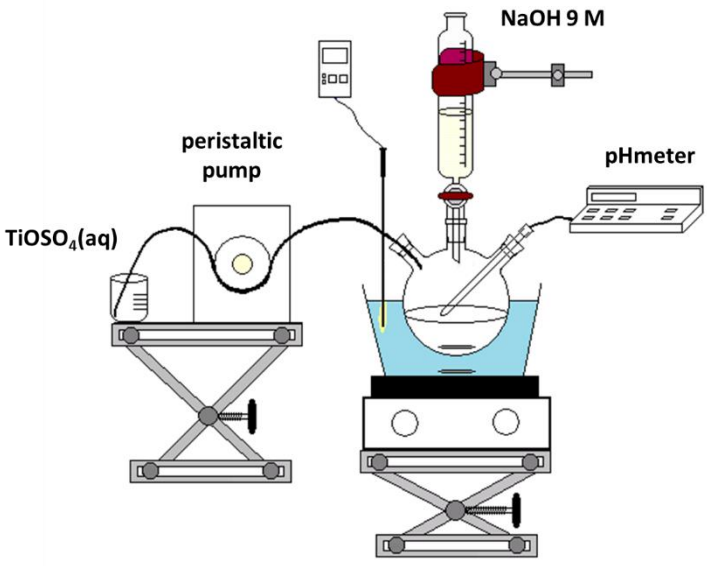

Figure 32 Lab-scale precipitation rig

In a 600 mL beaker, 200 mL of deionised water were added, then adjusting the pH to a value of 7. The solution containing titanium salt is dropped into deionised water at a rate of 1,5 mL/min by means of a peristaltic pump. The pH was maintained to a value of 7 by adding dropwise the NaOH 9 M solution, supervising it with a Metron 691 pHmeter. This leads to a white precipitate, namely $Ti(OH)_4$ suspension. During precipitation the suspension was maintained under vigorous stirring, to maintain homogeneity. After the complete addition of the titanium oxysuplhate solution, the as-prepared suspension was put in a round-bottom flask equipped with a reflux condenser, then set in a temperature-controlled ethylene glycol bath. The suspension of $Ti(OH)_4$ was aged at 60°C for 20 hours, in order to promote the evolution of the as-prepared precipitate, favouring agglomeration and complete titanyl salt hydrolysis. The aged suspension was finally cooled to r.t. and filtered with a Gooch funnel, collecting the $Ti(OH)_4$. The precipitate was washed with deionised water in order to remove as much as possible sodium and sulphate ions. Washed product was dried overnight at 110°C and then grinded yielding a $Ti(OH)_4$ powder. Eventually the precipitate was calcined in air at 400°C for 4 hours, with heating rate of 2°C/min and an air flow of 30 mL/min. The so-prepared pristine titanium dioxide was simply named TiO_2.

3.3.1.3. Copper-promoted materials

Incipient wetness impregnation

According to previous work [81], a selected amount of copper nitrate was dissolved in a proper amount of deionised water. The quantity of water was previously determined through a wettability test, adding dropwise water to a known amount of porous solid until a completely wet surface was obtained. The solution was added dropwise to 5 g of pristine titanium dioxide, stirring the powder with a glass rod to achieve a homogeneous distribution of the solution. The impregnated sample was then dried overnight at 110 °C and then calcined in air at 400 °C for one hour, with a heating rate of 2 °C/min and air flow of 30 mL/min. The sample thus obtained was named I##CuO/P25, if P25 was used, and I##CuO/TiO_2, if TiO_2 was used. Second and third digits, indicate the nominal amount of copper introduced (0,5% or 1,0%).

Deposition-precipitation

To get a very small size CuO nanomaterial, a DP technique was chosen [51]. A selected amount of copper nitrate was dissolved in a 600 mL beaker with 150 mL of deionised water, then adding an organic ligand under vigorous stirring, in molar ratio (ligand/copper) 1:3 in the case of 1,3-

propanediol and 1:2 in the case of citric acid. This ratio were chosen accordingly to copper (II) octahedral coordination geometry [48] and denticity of ligands [68]. Then 5 g of titanium dioxide were added to the solution and simultaneously a 0,5 M NaOH solution was prepared. Monitoring pH with a Metrohm 691 pHmeter, the NaOH solution was added dropwise to the copper-titanium dioxide suspension until pH 12 was reached. The solution's colour turned from white to blue-green, meaning that $Cu(OH)_2$ was formed. The as-prepared material was collected by a Gooch funnel, then washed with deionised water to remove sodium ions and the organic ligand. The material was eventually calcined in air at 400°C for 1 hours, with a heating rate of 2°C/min and air flow of 30 mL/min. The samples thus obtained was denoted as D##CuO/P25, C##CuO/P25, if P25 was used, and D##CuO/TiO_2, if TiO_2 was used. The first digit indicates the type of ligand used, 1,3-propanediol (D) or citric acid (C), while second and third indicates the nominal percentage of copper (0,5% and 1,0%).

3.3.2. Characterisations

The following characterisation techniques were used to understand physicochemical properties of the synthesised samples.

3.3.2.1. Thermal Gravimetric/Differential Thermal Analysis (TG/DTA)

Thermal gravimetric analysis, coupled with differential thermal analysis allows to identify physicochemical changes during sample heating in flow air. Thermal gravimetric analysis allows determining weight losses during heating, while differential thermal analysis identifies enthalpy variation during heating. Comparing results obtained from both TG and DTA, one can discern during a thermal treatment phenomenon entailing decomposition and consequent weight losses from phase transitions, that don't imply any weight loss. Alumina was used as reference and thermal differences between the two was monitored during the whole analysis.

TG/DTA analyses were performed in the Department of Earth Sciences at the University of Ferrara and prof. Giuseppe Cruciani is acknowledged for his collaboration. Simultaneous Netzsch Thermal Analyzer ST4 409 was used keeping a 10 mL/min air flow and a 10°C/min heating rate during all the analyses.

3.3.2.2. Nitrogen Physisorption

Nitrogen physisorption gives information concerning surface area, pore volume, pore size distribution and shape. This technique relies on non-selective absorption of gas molecule (adsorbate) on a solid surface (adsorbent) through weak interaction, such as dispersion forces or interaction between electrical dipoles [69]. According to International Union of Pure and Applied Chemistry (IUPAC), pores in porous material can be classified according to their size in [69,70]:

- Microporous, with pore diameter smaller than 2 nm
- Mesoporous, with pore diameter between 2 and 50 nm
- Macroporous, with pore diameter larger than 50 nm

Since heterogeneous catalysis is a surface phenomenon, knowledge of morphological properties such as surface area and pore size, is essentially to understand the correlations between catalytic properties and physicochemical properties of a catalyst.

The most used technique is nitrogen physisorption, relying on absorption and desorption of nitrogen at – 196°C [70]. Plotting the total amount of adsorbed (or desorbed) gas at a given value of relative pressure (p/p^0), yield a graph called adsorption isotherm. IUPAC classifies six types of isotherms, according to different materials (Figure 33).

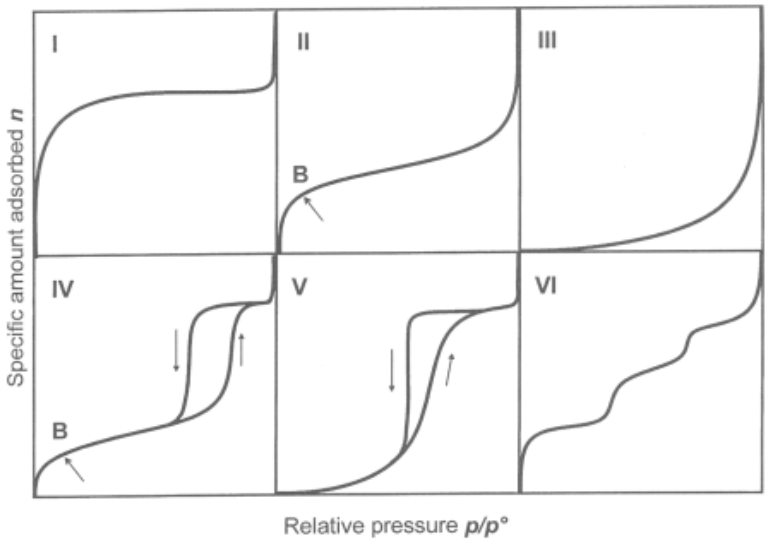

Figure 33 Adsoprtion isotherm by IUPAC classification [71]

Type I isotherm is typical for microporous materials. Type II regards non-porous or macroporous systems. Type IV is the most common and related to mesoporous material, showing also the typical hysteresis seen in Figure 33,IV. Type III and V are uncommon and regarded to weak adsorbate-

adsorbent interaction on macroporous or mesoporous materials, respectively. Type VI is related to flat surface with no porosity, showing a layer-by-layer adsorption.

Physisoprtion data were recorded using a Micromeritics ASAP 2000 Analyzer. Before starting the analysis, the sample (200 mg) was thermally treated in vacuum at 110°C for 3 hours in order to remove all adsorbed species. Surface area information was taken in 0,05-0,35 p/p^0 range, where no capillary condensation occurs. Surface area is calculated knowing the adsorbed nitrogen monolayer volume (V_m), through Equation 9. N_A is the Avogadro number ($6{,}023 \cdot 10^{23}$), 22414 represent the volume (cm^3) of one mole of ideal gas in standard conditions, while σ represent the occupied surface area by one molecule of N_2, generally accepted to be 0,162 nm^2 [70].

$$A_s = \frac{V_m}{22414} N_A \sigma$$

Equation 9 Surface area equation [70]

The monolayer adsorbed volume is calculated through the Brunauer, Emmet, Teller (BET) theory (Equation 10), whose fits experimental data only for p/p^0 lower than 0,35, where only physisorption occurs. V_{ads} is the adsorbed volume while c is the BET constant (related to adsorbate-adsorbent interaction).

$$\frac{p}{V_{ads}(p_0 - p)} = \frac{1}{V_m c} + \frac{c-1}{V_m c} \cdot \frac{p}{p_0}$$

Equation 10 BET equation [69]

3.3.2.3. Flame Adsorption Atomic Spectroscopy (FAAS)

This technique is used to quantify metallic elements in a sample. It was here used to determine copper content in promoted samples. It relies on excitation of one electron from the ground state of an atom to a higher energy orbital (excited state) by absorption of photon with an energy corresponding to energy difference between ground and excited states. This technique needs atoms in gaseous phase, obtained in FAAS by atomisation in a flame.

Before analysis a liquid sample must be obtained through a desegregation procedure. Operatively 100 mg of sample, previously dried in oven at 110°C overnight, are added in a 50 mL round bottom flask equipped with a reflux condenser, with 5 mL of milli-Q water and 5 mL of *aqua regia* (3:1 volumetric mixture of HCl and HNO_3). Heated was supplied by an Iso-pad, leaving the mixture under reflux for 3 hours. Then it was cooled in air. The desegregated solid-liquid mixture was added to a

100 mL volumetric flask and made up to volume with milli-Q water. A blank sample was also prepared putting 5 mL of *aqua regia* in a 100 mL volumetric flask and made up with milli-Q water.

Analyses were performed with a Perkin-Elmer Analist 100 flame atomic absorption spectrometer where flame has been fed by 1:3 acetylene-air mixture and a copper hollow-cathode lamp. The instrument parameters are:

- λ = 324,8 nm
- slit = 0,7 nm
- linearity range = 0 ÷ 5 ppm

For copper quantification, absorbance (A) was related to concentration (C) through the Lambert-Beer's law (Equation 11). ε is the molar absorptivity and b is the path length.

$$A = \varepsilon \cdot b \cdot C$$

Equation 11 Lambert-Beer law [72]

3.3.2.4. Ion Exchange Chromatography (IEC)

This technique is used to determine the concentration of both cation and anion in a sample. Ions in liquid sample are separated through an ion exchange chromatographic column, relying on ion exchange equilibrium [72]. In this work IEC was used to quantify sulphates.

Before analysis an extraction is performed to get sulphates in liquid form. Operatively 100 mg of sample were put in a 250 mL volumetric flask, and made up with a 0,1 M NaOH solution prepared in milli-Q water. The suspension was left to stand at room temperature for 30 minutes before analysis and collect by a syringe with a Teflon® 45 µm filter (LC20 Bionex).

Analyses were performed with a LC20 ionic chromatograph, equipped with a 25 µL injection loop, a 4 x 50 mm AS14 separation column, a 4 x 250 mm AG14 guard column, an acid resin suppressor and a ED40 conductivity detector. The eluent was a buffer solution of 10 mM Na_2CO_3 and 3,5 mM $NaHCO_3$ in milli-Q water, providing a flow of 1,2 mL/min at room temperature. Calibration curve was obtained from sulphate standard solution between 1 and 8 ppm.

3.3.2.5. Temperature Programmed Reduction (TPR)

Temperature programmed reduction is used to monitor reduction reaction while temperature is increased linearly in time. This technique provides information about reduction temperature of

metallic species [73], which is related to oxidation state and also interaction between metal and support.

Operatively, 50 mg of sample have been placed in a U shaped quartz reactor and heated in a 5% H_2/Ar gas mixture, flowing at 40 mL/min and heating with a rate of 10°C/min from room temperature to 800°C. A magnesium perchlorate trap is used to remove water for the gas flow. Hydrogen consumption is monitored by a Gow-Mac thermal conductivity detector (TCD), and it indicates that a reduction reaction occurs. Eventually hydrogen consumption is plotted against temperature.

3.3.2.6. Temperature Programmed Oxidation (TPO)

Temperature programmed oxidation is a technique usually used to detect carbon or nitrogen oxidisable residues on a solid material [74]. Carbon residues can be wanted (e.g. C-doping) or unwanted (e.g. coke deposit in used catalyst or organic residues on fresh catalyst those can react leading to misunderstanding of activity results [75]) and TPO is a useful technique for its detection.

Operatively the same procedure and analysis rig of TPR was used. The gas mixture used is a 5% O_2/He and the trap is equipped with magnesium perchlorate and soda-lime to remove water and CO_2, respectively. Eventually oxygen consumption is plotted against temperature.

3.3.2.7. X-Ray Diffraction (XRD)

X-ray diffraction is a widely used technique in solid-state material characterisation to get information concerning crystal phases and their abundance, crystallite sizes and distortion of the crystal lattice.

X-rays are an energetic form of electromagnetic radiation, with wavelength between 10^{-3}-10 nm [78], comparable with atomic-scale dimensions. When X-rays penetrate matter, oscillation of electron inside the crystal occurs and yield radiation with the same wavelength of the incoming: this is the scattering phenomena. Moreover, due to ordered structure of scattering atoms (periodic lattice), constructive and destructive interference occurs, depending on the diffraction angle (θ): this is the diffraction phenomena. Each material phases has a particular diffraction pattern, a graph in which intensity of scattered rays are plotted against 2θ.

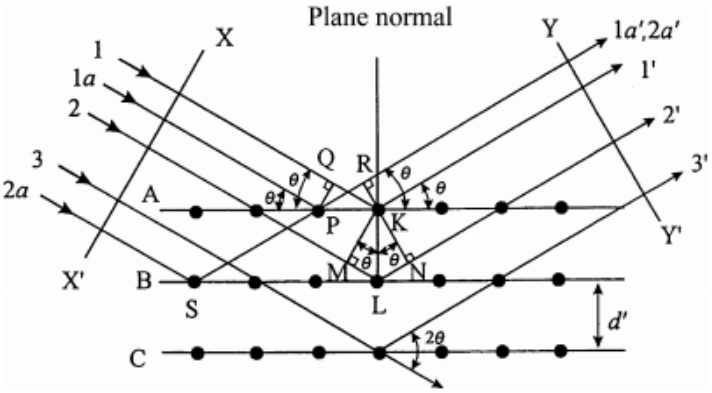

Figure 34 Diagram of scattering of X-ray by a crystal [78]

A correlation between diffraction angle (θ) and atom spacing (d_{hkl}) between two crystallographic planes with the same Miller indexes (h,k,l) (Figure 34) is given by Bragg's law (Equation 12). λ is the wavelength of incident radiation and n the order of diffraction.

$$n\lambda = 2d_{hkl} \sin\theta$$

Equation 12 Bragg's law [73]

Lattice constant (a, b, c) and volume can be calculated from plane spacing (d_{hkl}), whose knowledge is useful to understand possible lattice distortion. Eventually crystallite sizes (t) can be determined through the Scherrer equation (Equation 13). K is a constant that depends on the peak's shape, λ is the wavelength of incident radiation, θ is the diffraction angle and β the full width at half maximum intensity.

$$t = \frac{K\lambda}{\beta \cos\theta}$$

Equation 13 Scherrer equation [73]

Wide angle x-ray scattering (WAXS) was used to obtain this information. XRD analyses have been performed in the Department of Earth Science at the University of Ferrara and prof. Giuseppe Cruciani is acknowledge for his collaboration. It has been employed an automatic diffractometer Phillips PW 1829/00, whose emitted radiation are CuKα1,2 that works at 40 kV and 30 mA. Instrumental parameters are reported below:

- Stepsize = 0,02°
- Antiscatter = 1/2°, 0,1 mm, 1/2°
- 2θ range = 5-80°

- Time/step = 3 s

3.3.2.8. Diffuse Reflected Spectroscopy (DRS)

This technique is widely used to determine the bandgap of semiconductor, a critical parameter in photocatalysis. Moreover, effect of dopants or impurities in the lattice can be detected through bandgap modification.

DRS analyses have been performed in the Department of Chemistry at the University of Turin and Dr. Maela Manzoli is acknowledged for her collaboration. It has been employed a Varian Cary 5000 spectrophotometer, working in the 50000-4000 cm^{-1} range and running spectra at room temperature. UV-vis spectra are reported in the Kubelka-Munk function (Equation 14), where R_∞ is reflectance of an infinite thick layer of the sample.

$$f(R_\infty) = \frac{(1 - R_\infty)^2}{2R_\infty}$$

Equation 14 Kubelka-Munk function [76]

Correlation among wavenumber, wavelength and energy is given in Equation 15, where h is the Planck constant ($6{,}626 \cdot 10^{-34}$ J·s) and c the light speed ($2{,}9979 \cdot 10^{8}$ m/s).

$$E = h \cdot \tilde{\nu} \cdot \mathrm{c} = \frac{h \cdot c}{\lambda}$$

Equation 15 Correlation among energy, wavelength and wavenumber [77]

3.3.2.9. Fourier-Transform IR spectroscopy (FTIR)

The IR spectroscopy is widely used in catalysis to identify surface moieties (e.g. different types of OH groups) and surface morphology and properties, by probing it with simple molecules such as carbon monoxide [73]. Moreover, FTIR is a useful technique to evaluate how reactants absorb on the catalytic surface and how reactions proceed (*in-situ* studies) [79].

Transmission FTIR analyses have been performed in the Department of Chemistry at the University of Turin and Dr. Maela Manzoli is acknowledged for her collaboration. Sample in the form of self-supported pellets was introduced in the cell. Outgassing is performed at room temperature for 10 minutes. CO adsorption was performed at – 183 °C while ethanol adsorption at room temperature and 5 mbar. Measurements were performed on a Perkin Elmer 2000 spectrometer equipped with a cryogenic MCT detector.

3.3.3. Catalytic activity tests

The reaction rig is reported in chapter 2, running the reaction in the condition identified and optimised in the same chapter. Briefly reminding them:

- UV-light source: 50 W/m^2, main emission peak at 365 nm
- Thin-film plate type borate glass reactor, volume 0,6 cm^3 and exposed surface 6 cm^2
- Gas flow: 1,5 mL/min
- Saturator: 60°C, 35% v/v ethanol in water

Analyses of reaction mixture were performed after 20 minutes after UV source light on, in order to avoid cold spot on the reactor setting and data were recorded in 170-200 minutes of reaction in order to get at least three complete analyses (about 40 minutes per analysis) of reaction mixture. Catalytic tests were repeated two times for each sample and average results were reported.

Ethanol conversions were calculated by Equation 16, where $C(0)_{EtOH}$ is the initial ethanol concentration in gas phase, while $C(t)_{EtOH}$ is the concentration at a certain reaction time.

$$X(\%)_{EtOH} = \frac{C(0)_{EtOH} - C(t)_{EtOH}}{C(0)_{EtOH}} \cdot 100$$

Equation 16 Ethanol conversion

Turn-over frequencies (TOF) and apparent quantum yield (AQY) were calculated starting from ethanol conversion instead of hydrogen production. This choice is justified by observed complete selectivity of the reaction toward dehydrogenation, as shown later, and problems in hydrogen detection since less than 1% of hydrogen in total flow wasn't detectable.

TOFs (mmol·g^{-1}·h^{-1}), were calculated by Equation 17. Here F_{EtOH} is the volumetric ethanol flow in mL/min; 3,55·10^{-5} (mol·mL^{-1}) is a correcting factor calculated from ideal gas equation (T = 60°C, P = 0,1 MPa), converting volumetric flows to molar flows; $X(\%)_{EtOH}$ is the conversion; m_{cat} the used catalyst's mass; 6·10^4 µmol·min·mol^{-1}·h^{-1} is another correcting factor converting TOF values in mmol and hours.

$$TOF = \frac{F_{EtOH} \cdot 3{,}55 \cdot 10^{-5} \cdot X(\%)_{EtOH}}{m_{cat}} \cdot 6 \cdot 10^4$$

Equation 17 Turn-over frequency (TOF)

AQYs, were calculated by Equation 18. Where the numerator is the same reported in Equation 17, while at the denominator I is intensity, A geometrical reactor surface area, λ main wavelength, h Planck constant, c light speed, N_A Avogadro number and 60 a correcting factor converting seconds to minutes.

$$AQY = \frac{2 \cdot mol_{H_2}}{mol_{photon}} = \frac{2 \cdot F_{EtOH} \cdot 3{,}55 \cdot 10^{-5} \cdot X(\%)_{EtOH}}{\frac{I \cdot A \cdot 60 \cdot \lambda}{h \cdot c \cdot 10^9 \cdot N_A}} \cdot 100$$

Equation 18 Apparent quantum yield (AQY)

One must remind that AQY consider all incident photon, not only absorbed [23].

3.4. Result and discussion

3.4.1. Pristine titanium dioxide

The first material tested were pristine titanium dioxide material: P25 (benchmark sample) and TiO_2 (lab-made precipitated sample).

Surface area is one of the most important parameter in heterogeneous catalysis, so it was determined by nitrogen physisorption. Isotherms are reported in Figure 35.

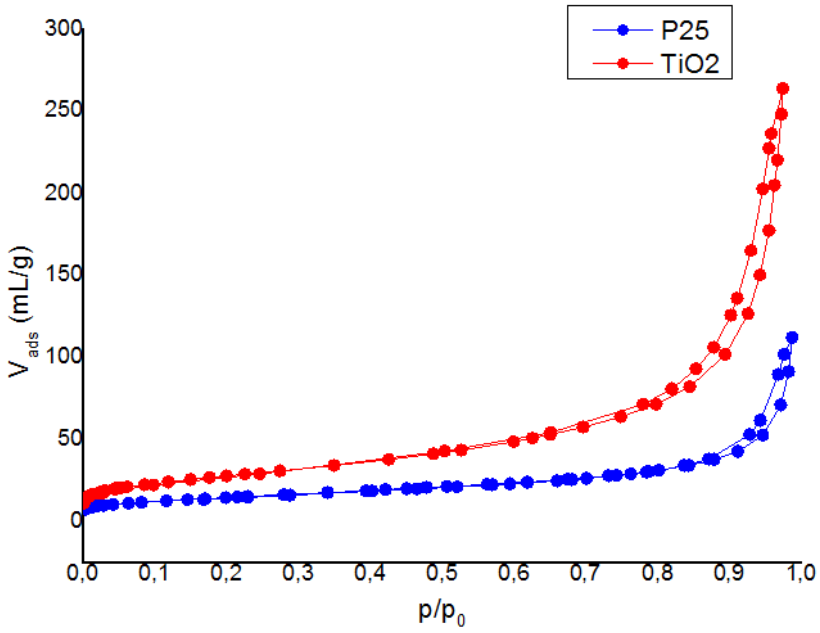

Figure 35 TiO2 and P25 physisorption isotherms

Both samples show a IV type isotherm, so these are mesoporous materials. Moreover the hysteresis looks like H1-type, corresponding to open-end cylindrical pores, but they finished close to saturation pressure ($p/p_0 = 1$), meaning that very wide pores (macropores) also exist in both samples. The surface areas (S_{BET}), calculated by the BET method, are reported in Table 3. The precipitation method affords a twofold surface area than benchmark P25.

Material	S_{BET} (m^2/g)
TiO_2	101
P25	50

Table 3 Surface area of titanium dioxide photocatalysts

Finally, since TiO_2 was prepared starting from a sulphate precursor and this anion is known to suppress catalytic activity [80], probably due to radical scavenging effect of sulphates moieties [81],

sulphate were quantified. IEC analyses was performed on P25, $Ti(OH)_4$ and TiO_2. Results, comparing with sulphate content of P25, are reported in Table 4. The losses of sulphate from titanium hydroxide to oxide can be attributed to their decomposition to volatile species like SO_3 during calcination.

Material	Sulphate (%)
P25	0
$Ti(OH)_4$	0,6
TiO_2	0,4

Table 4 Sulphates content of titanium dioxide materials

Catalytic tests were then run on pristine titanium dioxide material. It was first observed that the reaction proceeded through dehydrogenation instead of photoreforming, since only acetaldehyde was detected as product: it could be concluded that the reaction proceeded basically as a pure photodehydrogenation (Equation 19).

$$C_2H_5OH \rightarrow CH_3CHO + H_2$$

$$\Delta G^0 = +41{,}5\ kJ/mol$$

Equation 19 Ethanol dehydrogenation [17]

Nevertheless can be thought as the first step of ethanol photoreforming, reminding the proposed mechanism reported in section 1.5.3. Ethanol conversions are reported in

Figure 36, while TOFs and AQYs are reported in Table 5.

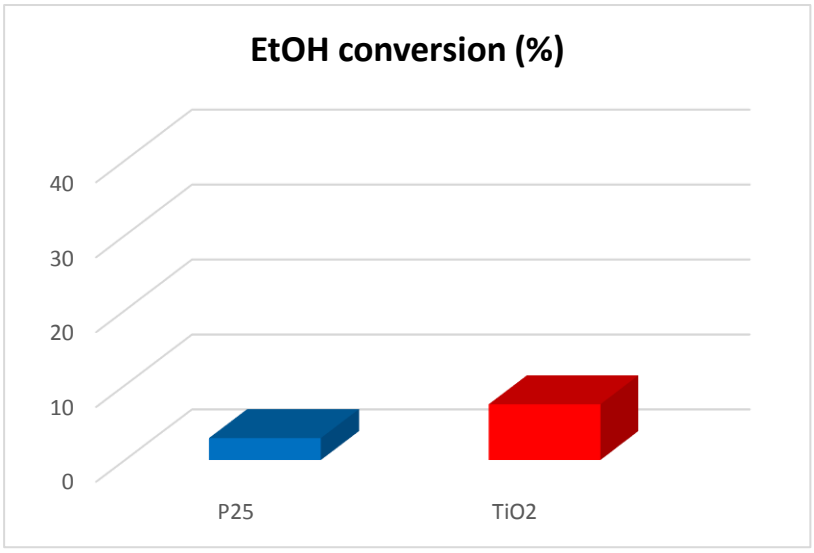

Figure 36 Ethanol conversion on pristine titanium dioxide photocatalysts

	TOF ($mmol \cdot g^{-1} \cdot h^{-1}$)	AQY (%)
P25	0,9 ± 0,1	5,7 ± 0,7
TiO_2	2,6 ± 0,2	15 ± 1

Table 5 TOF and AQY for pristine titanium dioxide photocatalysts

The TiO_2 photocatalyst gave the best result in term of both activity (conversion and TOF) and AQY. Reminding surface area reported above, it could be concluded that surface area plays a significant role in catalytic activity enhancement. Nonetheless, as shown in the introduction of this chapter, also crystal phase and crystallinity play an important role: XRD analyses are still ongoing to evaluate these parameters.

Finally UV-visible DRS spectra were recoded (Figure 37). TiO_2 sample shows a slight blue-shift in band-gap with respect to P25. Since rutile and anatase have different bandgap, 3,0 eV and 3,21 eV respectively, this shift can be attributed to different phase composition. XRD will confirm this hypothesis.

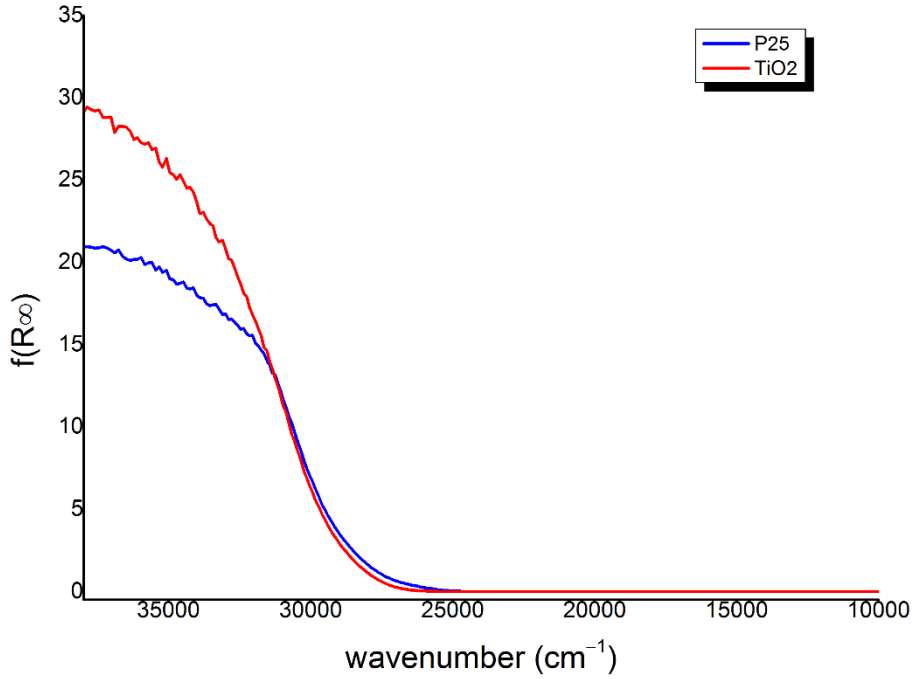

Figure 37 UV-vis DRS spectra of P25 and TiO_2 photocatalysts

In order to further improve catalytic activity, it was decided to introduce a copper promoter, studying introduction technique and loading. Since the chosen titanium dioxide materials exhibits different photocatalytic behaviour, it was decided to add copper to P25 (benchmark product with well-known physicochemical properties) identifying the best technique and loading, and then to high-surface area TiO_2.

3.4.2. CuO-promoted P25

The P25 was promoted with CuO with two techniques: incipient wetness impregnation and DP method, which in turn was performed with two different organic ligands. Moreover, two copper loading were used: 0,5 % and 1,0 %.

The syntheses (section 3.3.1.3) include a calcination step and, since very high temperature should be avoided, TG-DTA analyses were performed on uncalcined catalyst to identify the lowest temperature of thermal treatment in order to get the final material and to completely eliminate ligand traces. In order to get the highest sensibility, analyses were performed on 1 % loaded samples. In Figure 38 it is reported TG-DTA graph of impregnated sample. A remarkably loss of weight happened up to 400°C. An endothermic peak slightly above 100°C can be attributed to water losses (black arrow in Figure 38), since evaporation is an endothermic process. An exothermic peak at 350°C (red arrow) can be attributed to nitrate precursor decomposition. Eventually another

intense peak at 700°C was identified, where no weight losses occurs: this can be ascribed to anatase-to-rutile phase transition.

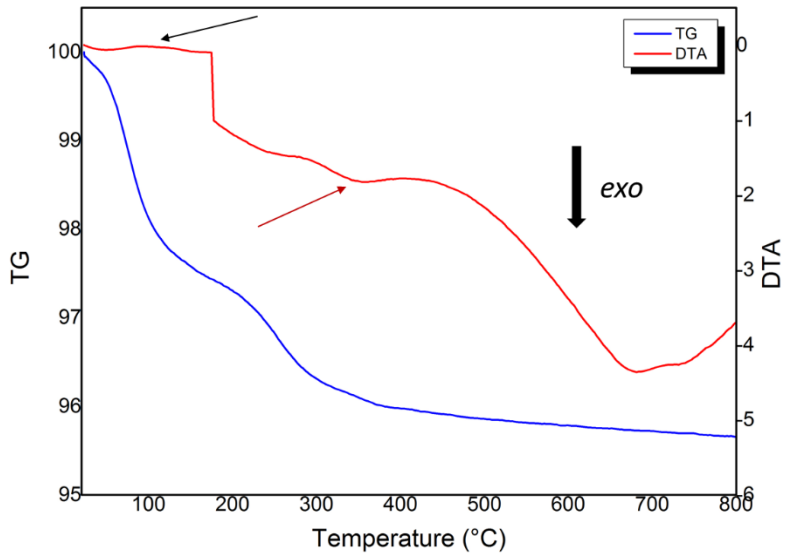

Figure 38 TG-DTA of uncalcined I1,0CuO/P25

In Figure 39 and Figure 40 TG-DTA of raw D1,0CuO/P25 and C1,0CuO/P25 are reported, respectively. Qualitatively the graphs are the same of impregnated sample, the only difference is the strong exothermic peak at temperature below 300 °C, ascribing to oxidation of residual ligand. Thus, a calcination temperature of 400 °C was chosen for all samples.

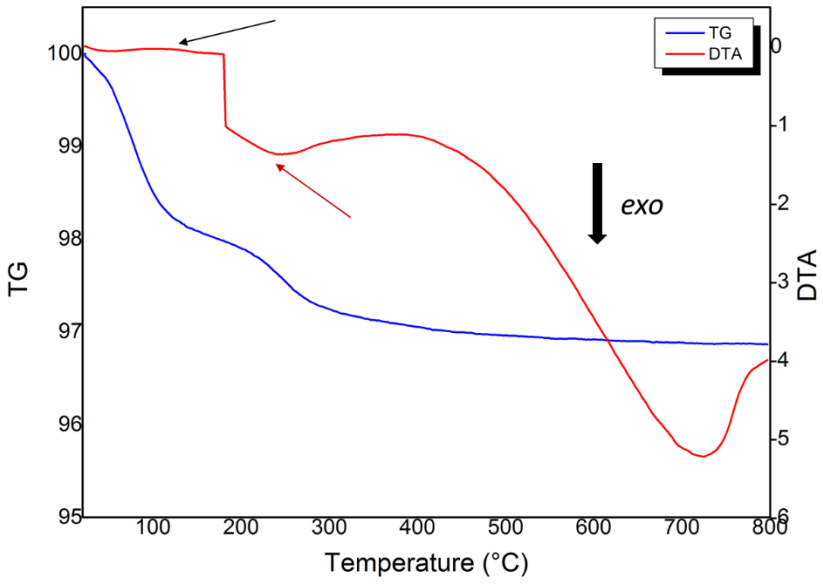

Figure 39 TG-DTA of uncalcined D1,0CuO/P25

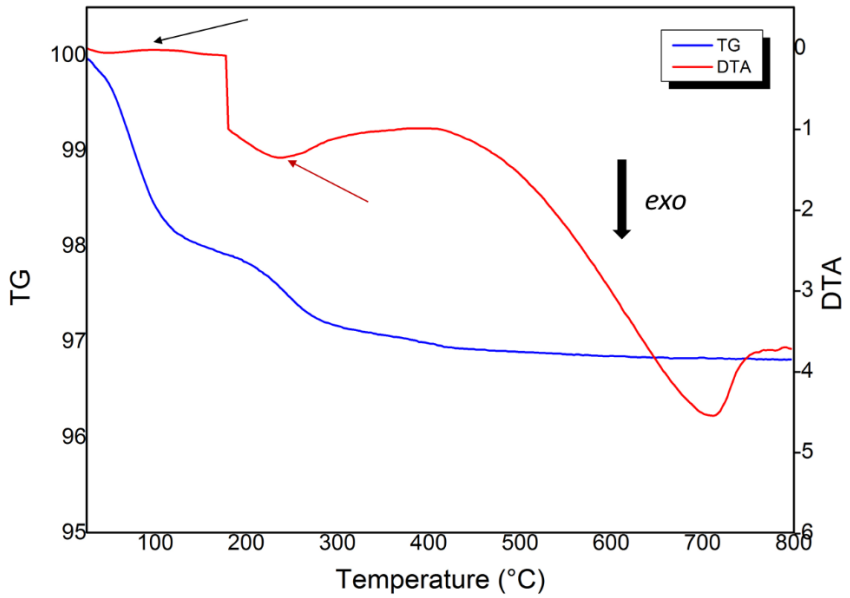

Figure 40 TG-DTA of uncalcined C1,0CuO/P25

A TPO analysis was finally performed on calcined sample from DP, in order to detect the complete removal of organic carbon. As pictured in Figure 41, no peaks ascribing to organic carbon oxidation occurs, confirming that the chosen calcination procedure is suitable to complete carbon residues removal.

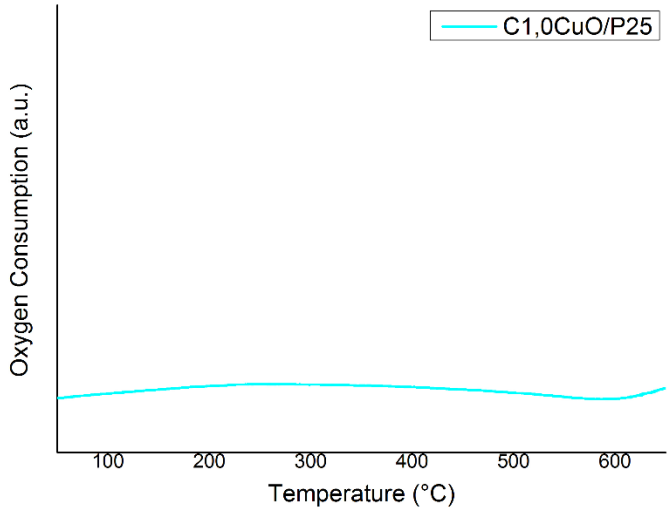

Figure 41 TPO analysis on calcined C1,0CuO/P25

In order to evaluate surface area and actual copper loading, FAAS and nitrogen physisorption were performed on synthesised samples, respectively. Results obtained are summarised in Table 6. Actual copper loadings were close to nominal value, whereas surface area values were quite similar and a bit smaller than pristine P25, probably due to a little sintering during calcination and CuO partially occupying titania's pores.

	Cu loading (%)	S_{BET} (m^2/g)
I0,5CuO/P25	0,4	41
I1,0CuO/P25	0,9	42
D0,5CuO/P25	0,4	44
D1,0CuO/P25	1,0	42
C0,5CuO/P25	0,4	45
C1,0CuO/P25	1,0	43

Table 6 Actual copper loading and surface area of Cu-promoted P25

XRD analyses are ongoing to get information concerning crystal phase and possible lattice distortion due to copper entering.

The catalytic tests performed on these material showed no change in selectivity on any copper-promoted sample, meaning that pure dehydrogenation occurs also in this case. Nevertheless a remarkably increase in catalytic activity was observed, with an increase of conversion up to twelve-fold for Cu-promoted with respect to pristine P25. Ethanol conversion results are reported in Figure 42 while TOF and AQY in Table 7, inserting P25 data for comparison.

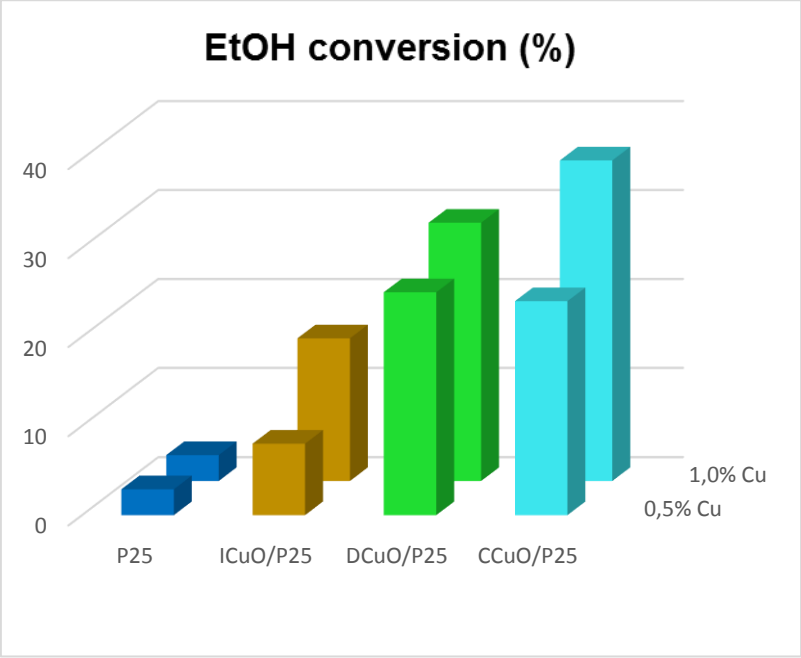

Figure 42 Ethanol conversion of Cu-promoted P25 photocatalysts

	TOF (mmol·g^{-1}·h^{-1})	AQY (%)
P25	0,9 ± 0,1	5,7 ± 0,7
I0,5CuO/P25	3 ± 1	20 ± 7
D0,5CuO/P25	7,5 ± 0,6	45 ± 4
C0,5CuO/P25	7 ± 2	44 ± 12
I1,0CuO/P25	6 ± 1	36 ± 6
D1,0CuO/P25	9 ± 2	57 ± 13
C1,0CuO/P25	10 ± 2	64 ± 13

Table 7 TOF and AQY of Cu-promoted P25 photocatalysts

Comparing the copper loading, increasing the metal loading from 0,5% to 1,0% enhances the hydrogen production, independently on introduction technique. This can be ascribed to an increment of active sites for hydrogen reduction and electron trapping on the surface. Concerning the introduction technique, the best outcomes were achieved with DP-method, and no remarkable difference on used ligand (propanediol or citric acid) were observed. Moreover, all samples have a similar surface area so these parameters cannot affect the reactivity.

The comparison of conversion and catalytic activity results with those reported in literature was not easy due to very different operative conditions (temperature, composition, flow, irradiance, wavelength, reactor design, organic substrate). Nevertheless it is worth comparing AQYs: the highest value reported in Table 7, although it is affected by a large error, is close to one of the best reported photocatalytic material (doped $NaTaO_3$), yielding an AQY of 56% at 280 nm [91] and also higher than the best AQY identified in the gas phase up to now [7].

In order to understand how physicochemical properties of the samples affect the catalytic activity, further analyses were done. The simplest difference is samples appearance, specifically their colour. As reported in Figure 43, DP-prepared samples appear to be lighter green (Figure 43 A and B) than impregnated, which is darker (Figure 43 C). Since copper loadings are basically the same, this could mean that structural properties of CuO, those in turn affect optical properties such as absorbance, are different and depend on introduction technique.

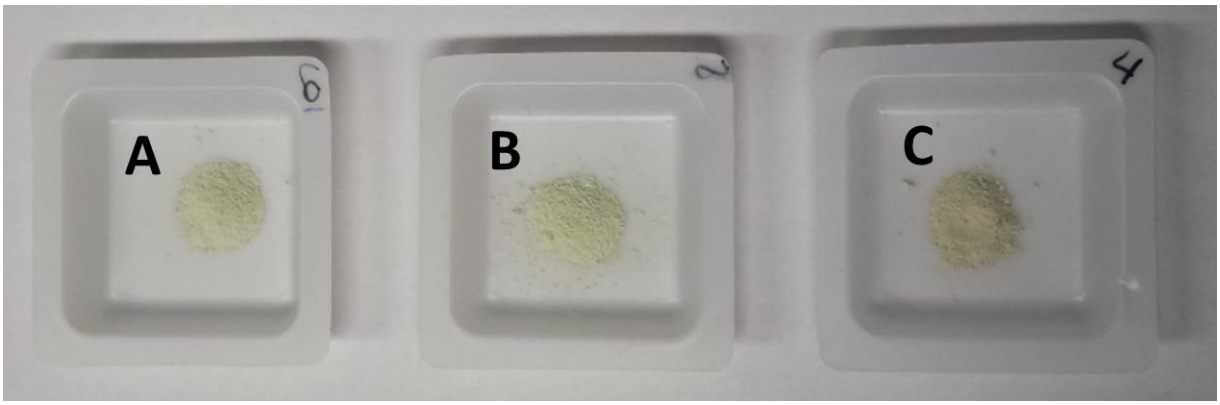

Figure 43 Appearance of Cu-promoted sample: D1,0CuO/P25 (A), C1,0CuO/P25 (B) and I1,0CuO/P25 (C)

TPR analyses was also performed on Cu-promoted P25 samples, in order to evaluate reduction temperature of copper oxide. As reported in Figure 44, reduction peaks close to 200°C can be seen for each samples. Deeply analysing TRP graphs, one can see that DP-sample shown a slightly lower T_{RED}, (174°C and 178°C for diol and citrate ligand-modified technique respectively), than impregnated sample (189°C). Moreover a weak peak is observed for the latter at 287°C,indicated in Figure 44 with a black arrow.

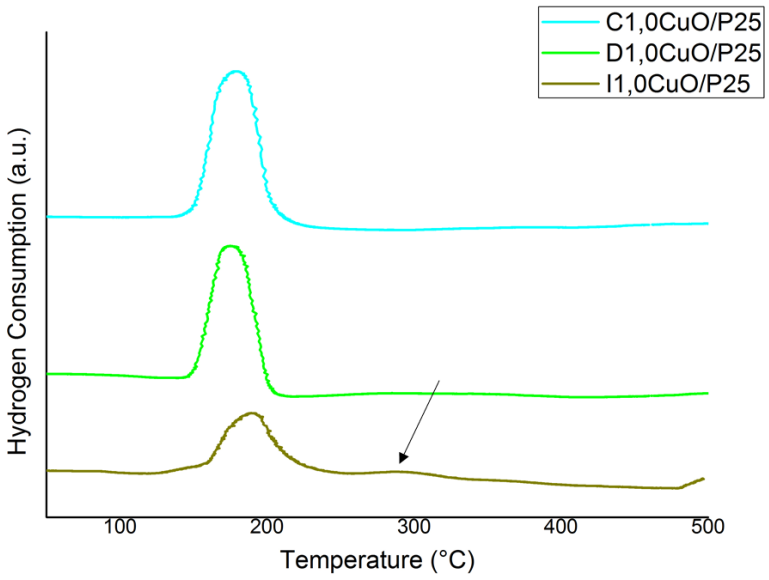

Figure 44 TRP of 1% Cu-promoted P25 photocatalysts

As reported in literature, the lower the T_{RED}, the higher the dispersion of the material, and the weak peak at 287°C found in impregnated sample TPR profile, can be ascribed to large CuO particles with less interaction with the support [84]. Although TPR are thermal experiment, on a photocatalytic point of view lower T_{RED} could be correlated to a more facile electron transfer to CuO particles: this can explain the better reactivity of DP samples (lower T_{RED}) than impregnated ones (higher T_{RED}).

DRS analyses on some of Cu-promoted P25 samples, compared with pristine P25 are reported in Figure 45. In Cu-promoted photocatalysts, a band centred at 12500 cm^{-1} (800 nm) was identified and ascribed to d-d transition in copper (II) oxide nanoparticles [85,86], meaning that actual CuO particles exists. Moreover, the observed red-shift on adsorption edge (band-gap) can be correlated to partial copper ions incorporation in titanium dioxide lattice, thus no all the copper loaded is available as CuO. Unfortunately this couldn't prove if CuO was existing as surface specie or it entered in titanium dioxide particle.

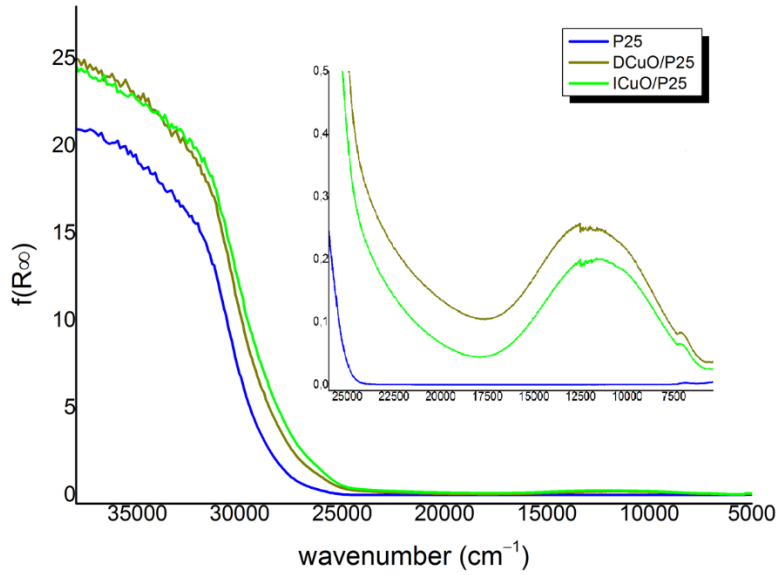

Figure 45 UV-visible DRS spectra of P25 and Cu-promoted P25 samples

Concluding the copper promotion remarkably improved catalytic activity of P25. It was also proven that 1% Cu loading has given better result than 0,5% Cu independently on introduction technique. Eventually, among the two investigated method of synthesis, deposition-precipitation (DP) showed the best results, and no or little difference concerning the ligand used (diol or citric acid) was observed.

3.4.3. CuO-promoted TiO_2

The screening on P25 allowed to identify the best introduction techniques. To further improve catalytic activity, it was decided to use an higher surface-area material, namely precipitated TiO_2.

A copper loading of 1% was chosen since it gave the best result independently on introduction technique. Two techniques were used: impregnation and DP method with 1,3-propanediol ligand, in order to evaluate effect of these introduction technique on high-surface area titanium dioxide too.

The TG-DTA analysis was performed on the uncalcined impregnated sample only, since higher temperature peak was previously observed on impregnated sample with respect to DP samples. TG-DTA diagram is reported in Figure 46. Surprisingly a different upon heating behaviour from those identified in I1,0CuO/P25 was detected. First, the weight losses end only above 650°C and a slight decrease in weight was observed between 250°C and 500°C. An endothermic peak at temperature slightly above 100°C can be ascribed to water losses (black arrow), as in P25-based samples, while two exothermic peak at 300°C and 450°C (red arrows) occurred in the temperature range of slighter decrease in weight (250-400°C). These exothermic peak can be ascribed to nitrate decomposition, although is not clear what really happens. Finally an intense peak at temperature higher than 800°C probably indicate the anatase-to-rutile transition, since no weight losses was here observed

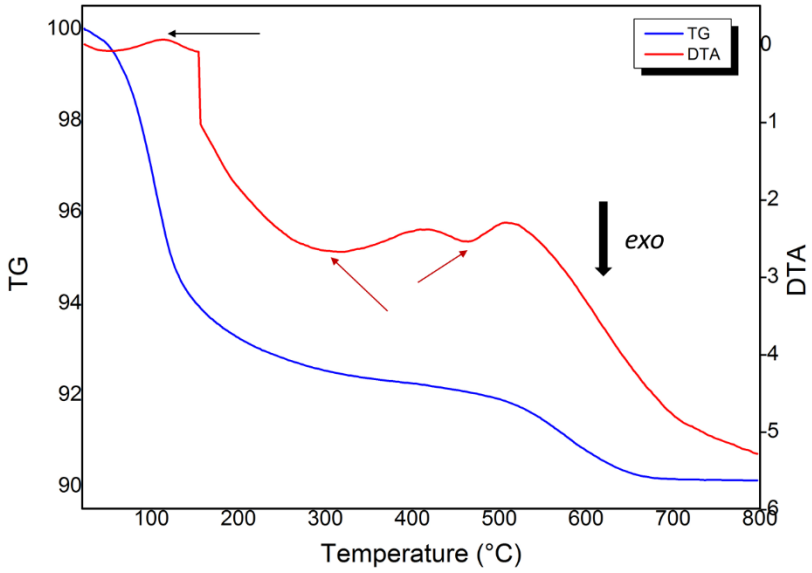

Figure 46 TG-DTA of uncalcined I1,0CuO/TiO_2

Although weight losses stop only at temperature higher than 650°C, it was decided to calcine the material with the same procedure used for P25-promoted samples in order to avoid great surface area contraction due to sintering.

As for P25-promoted samples, FAAS and nitrogen physisorption analyses (single point BET) were performed on these TiO_2-promoted samples in order to determine actual copper loading and surface area, respectively. Results are summarised in Table 8. As for P25-promoted samples, actual copper loadings were close to nominal value.

	Cu loading (%)	S_{BET} (m^2/g)
I1,0CuO/TiO₂	0,9	71
D1,0CuO/TiO₂	0,9	101

Table 8 Copper loading and surface area of 1% Cu-promoted TiO_2

An interesting behaviour was identified for surface area. Concerning impregnated sample, this parameter was about 30% lower than pristine material (TiO_2), and this can arise from sintering phenomena during calcination or partial pore-lockage by CuO particles. On the contrary, DP-sample shown exactly the same surface area of pristine titanium dioxide. Since it is unluckily that any surface area losses happened during calcination, another hypothesis was proposed. It has been known during aging of precipitated suspension, dissolution-reprecipitation phenomenon occurs [35], so this phenomena was bring into play. The hypothesis is that dissolution-reprecipitation yielded a higher surface area material than the pristine and, in the following thermal treatment, sintering led to a higher surface area than expected.

The catalytic tests showed no change in selectivity, as observed for Cu-promoted P25 photocatalysts. It was also observed, as for the P25-based catalysts, an increase in ethanol conversion upon addition of copper promoter, especially if DP method was used. Ethanol conversion are reported in Figure 47 while TOF and AQY in Table 9.

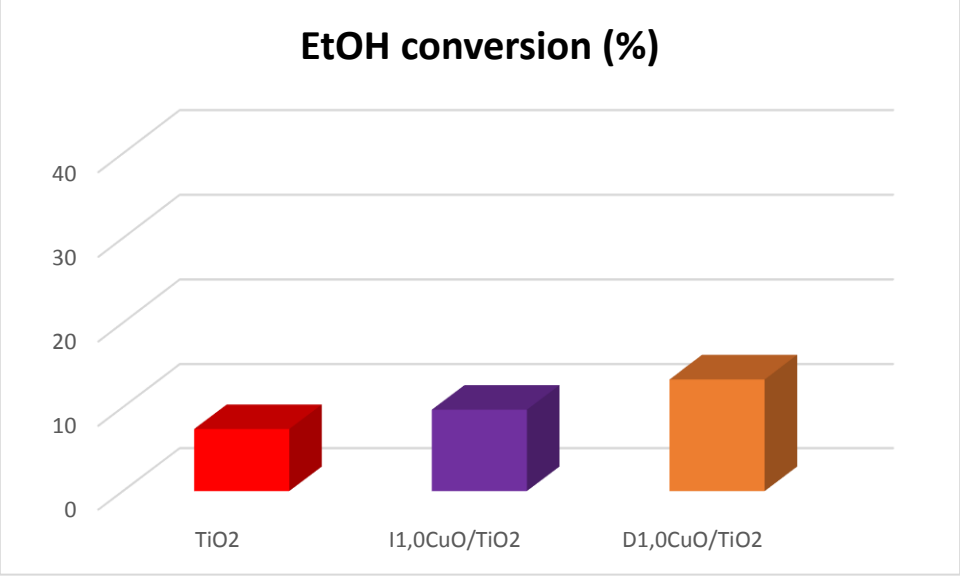

Figure 47 Ethanol conversion of Cu-promoted TiO_2 photocatalysts

	TOF (mmol·g^{-1}·h^{-1})	AQY (%)
TiO_2	2,5 ± 0,2	15 ± 1
I1,0CuO/TiO_2	3,1 ± 0,1	18,9 ± 0,9
D1,0CuO/TiO_2	4,7 ± 0,4	29 ± 2

Table 9 TOF and AQY of Cu-promoted TiO_2 photocatalysts

Although pristine TiO_2 gave better catalytic result than P25, promoting it with copper didn't increase activity as Cu-promoted P25 samples: DP-prepared samples showed tenfold increases of TOF on P25, while only twofold was observed on TiO_2. Nonetheless copper promotion on TiO_2 enhanced catalytic activity with respect to pristine material, especially with DP-prepared samples, as observed in P25-based samples.

As for P25-promoted samples, TPR analyses (Figure 48) were performed to understand this different behaviour with respect to P25 samples. Surprisingly the TPR patterns were completely different than P25 samples. Promoted material showed low temperature peaks at 337°C and 288°C for impregnated and DP samples, respectively. Moreover high temperature peaks, around 700°C, were observed and identified as reduction of the titanium dioxide itself [87], as shown by TPR of pristine TiO_2. Interestingly no high-temperature peaks ascribed to titanium dioxide reduction were seen on P25-promoted sample TPR.

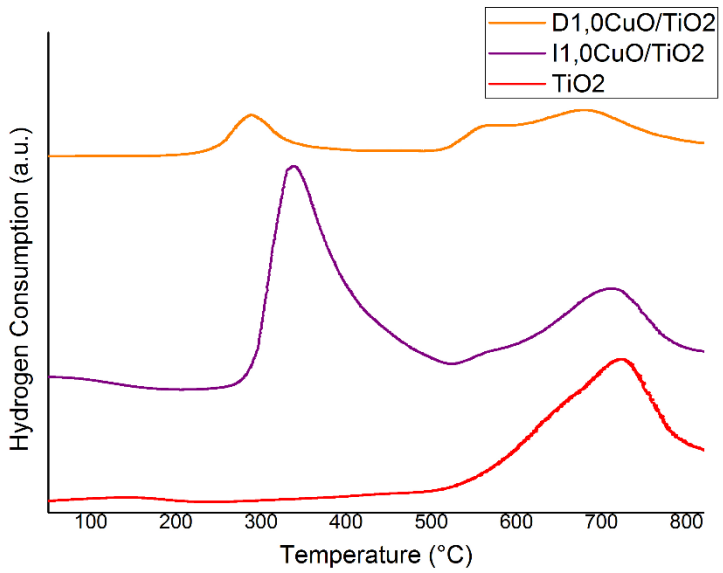

Figure 48 TPR of TiO_2-based sample

The reduction of titanium dioxide is confirmed by the change in colour of reduced sample, as reported in Figure 49. The partial reduction of Ti(IV) to Ti(III) is known to give a material known as titanium black, which has a dark-blue colour [87]. Concluding remarks on TPR analyses are, on one

hand that copper oxide was hardest to reduce and so probably less dispersed than P25 samples, on the other hand TiO_2 material here prepared is intrinsically more reactive than P25, since it can be easily reduced.

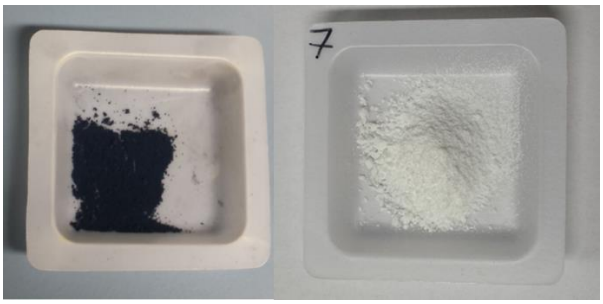

Figure 49 Pristine titanium dioxide (right) and titanium black (left)

The unexpected behaviour of lab-made TiO_2 can be explained with the following hypothesis. Residual sodium sulphate from precipitation was converted to sodium oxide and volatile sulphur trioxide, during calcination of $Ti(OH)_4$ (Equation 20).

$$Na_2SO_4(s) \rightarrow Na_2O(s) + SO_3(g)$$

Equation 20 Sodium sulphate thermal decomposition

Sodium ions acted as point defect, distorting the crystal lattice, making it more reactive (e.g. easier to reduce). Moreover, distorted lattice was probably able to strongly bond copper ions, making them less reducible and less active toward photoreforming reaction. To confirm this hypothesis, XRD analyses are ongoing in order to get information about lattice distortion.

DRS analyses were also performed on these samples and spectra are reported in Figure 50, also comparing TiO_2 samples with a Cu-promoted P25. A weak band centred at 11300 cm^{-1} (883 nm) corresponding to d-d transition of CuO was identified as in the case of promoted P25 samples. Moreover, a red-shift of adsorption edge (band-gap) occurs in Cu-promoted TiO_2, meaning that some copper ions were introduced in the titania lattice.

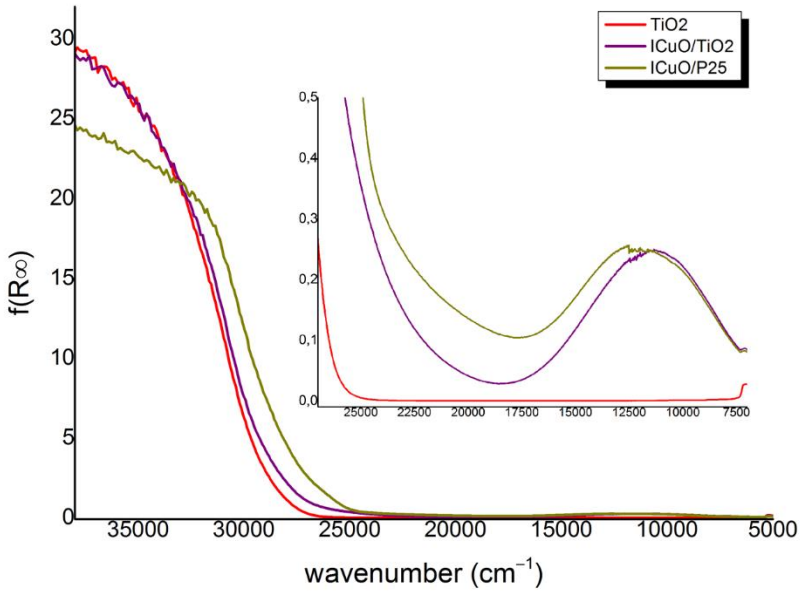

Figure 50 UV-visible DRS of TiO_2, Cu-promoted TiO_2 and Cu-promoted P25

An interesting comparison can be done between Cu-promoted P25 and Cu-promoted TiO_2 spectra reported in Figure 50: d-d bands in the 17000-5000 cm^{-1} region corresponding to CuO nanoparticles, are narrower meaning less heterogeneous CuO particles and diverse efficiency of d-d transitions.

Concluding, the expected enhancement of catalytic activity of Cu-promoted TiO_2 samples was not satisfied, nonetheless improvement was observed with respect to pristine TiO_2. Moreover, as for P25-promoted photocatalysts, DP method shown better results than impregnation. Nevertheless this enhancing seemed to be correlated to higher surface area rather than better dispersion of copper oxide.

3.4.3. FTIR analyses

All the techniques previously used, except of BET analyses, provide information concerning the bulk material. Since heterogeneous catalysis is a surface phenomenon, a surface-probing technique like FTIR is more useful to get information about surface morphology.

FTIR analyses were performed on TiO_2 and I1,0CuO/TiO_2 samples. In Figure 51 FTIR spectra of TiO_2 and Cu-promoted TiO_2 are reported. Focusing attention on 4000-2500 cm^{-1} region, a large band between 2700 cm^{-1} and 3700 cm^{-1} (indicated by blue arrows) can be seen, and it corresponds to OH stretching of adsorbed water: upon outgassing at r.t. (blue and green thinner curves), their intensity is reduced since water is partially desorbed. This is an important consideration since water is a co-reactant in photoreforming and it is known to be adsorbed as a layer on titanium dioxide surface [94],

so adsorbed water emulates the reaction medium. Finally, weak peaks just below 3000 cm^{-1} (red arrow) observed during outgassing (thin blue lines), can be attributed to vibrational transition of electron in titania's CB. In outgassed promoted titania (thin green lines) these signals disappeared, meaning that electrons are efficiently trapped by copper promoter.

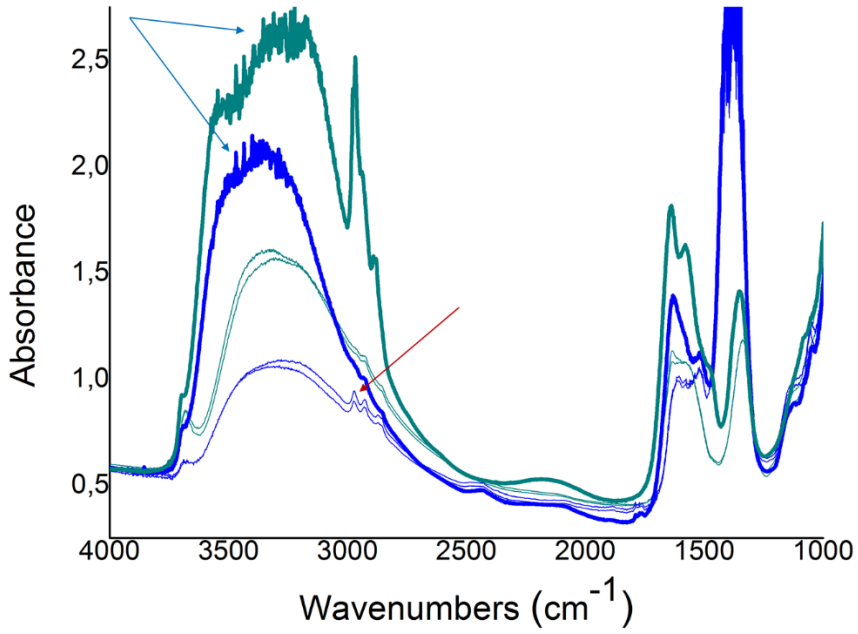

Figure 51 FTIR spectra of TiO_2 (blue) and I1,0CuO/TiO_2 (green)

The surface of photocatalyst was then probed with carbon monoxide (CO) at – 183 °C, after an outgassing at r.t. in order to remove adsorbed molecule possible interfering with CO adsorption. FTIR spectra of 4000-2600 cm^{-1} (OH bond stretching) and 2250-2000 cm^{-1} region (CO bond stretching) are reported in Figure 52.

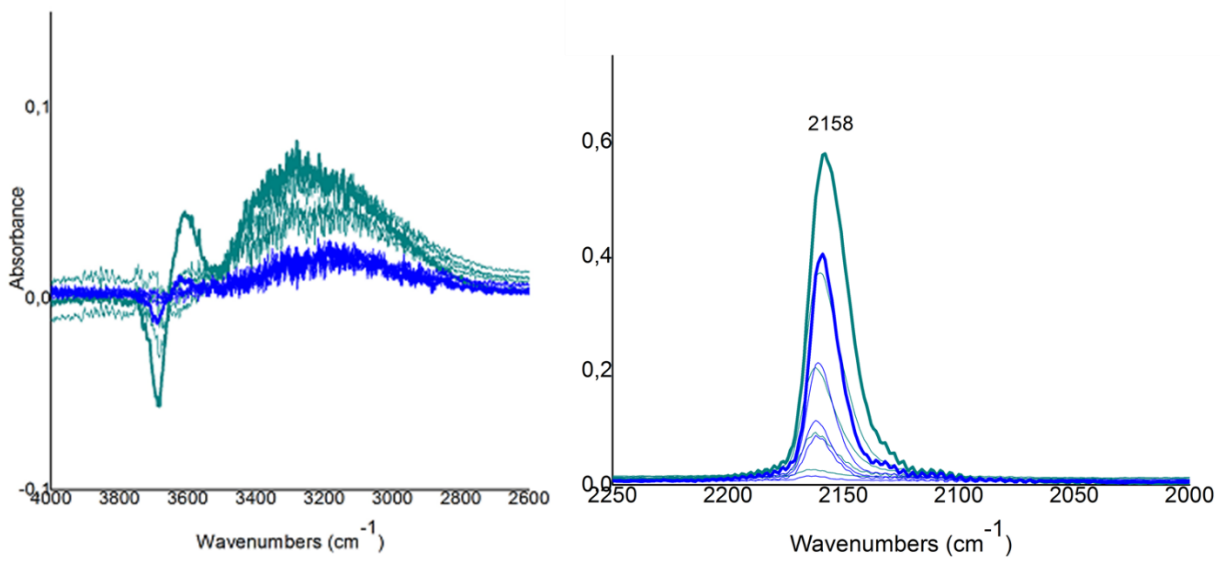

Figure 52 FTIR spectra of CO adsorbed on TiO_2 (green) and I1,0CuO/TiO_2 (blue) 2250-2000 cm^{-1} (right) and 2600-4000 cm^{-1} region (left)

The CO band observed in Figure 52 (right), is actually composed of three overlapped component: CO interacting by hydrogen bond with surface OH moieties (about 2150 cm^{-1}), CO coordinated to Cu^{2+} surface sites (2160-2120 cm^{-1}) and CO coordinated to Ti^{4+} surface sites (2175-2160 cm^{-1}) [89] and this lead to a slight shift observed between the two samples. Nevertheless the strongest component is the first (CO-HO). Comparing the pristine and the promoted sample, the band at 2158 cm^{-1} is more intense in TiO_2 (green) rather than in promoted-TiO_2 (blue) and this simply mean that highly dispersed CuO covering titanium dioxide surface was present. Moreover neither Cu^0 nor Cu^+ species are detected upon CO adsorption [90], meaning that only Cu^{2+} was present.

The 2600-4000 cm^{-1} region reported in Figure 52 (left) confirmed those observed in the CO band: on promoted-TiO_2 there were less hydroxyl groups on the surface, meaning that titanium dioxide surface is partially covered by nano-sized CuO.

Ethanol adsorption was also studied with CO-probed FTIR spectroscopy. After outgassing, spectra was recoded upon CO adsorption at 90 K then, after outgassing of CO, ethanol was absorbed at r.t. and 5 mbar and finally CO was adsorbed again at 90 K recoding the new spectra. On TiO_2, as shown in Figure 53, CO peak remarkably decreased in intensity meaning that ethanol was adsorbed on hydroxyl surface groups in competition with CO.

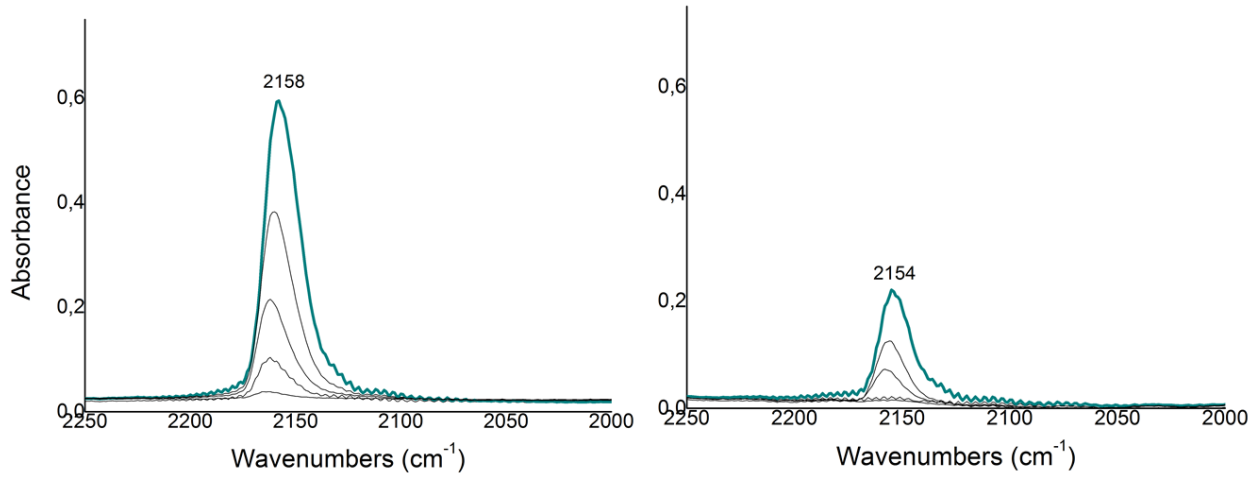

Figure 53 FTIR spectra of adsorbed CO before (left) and after (right) ethanol adsorption on TiO_2

In the case of promoted-TiO_2 (Figure 54) the same phenomena as TiO_2 happened upon ethanol adsorption. Nonetheless the intensity decrease of CO peak is less pronounced, simply meaning that less ethanol was adsorbed on titania surface, since a share was covered by CuO. This suggestion does not mean that no ethanol was also adsorbed on CuO surface, but the interaction on titania is stronger.

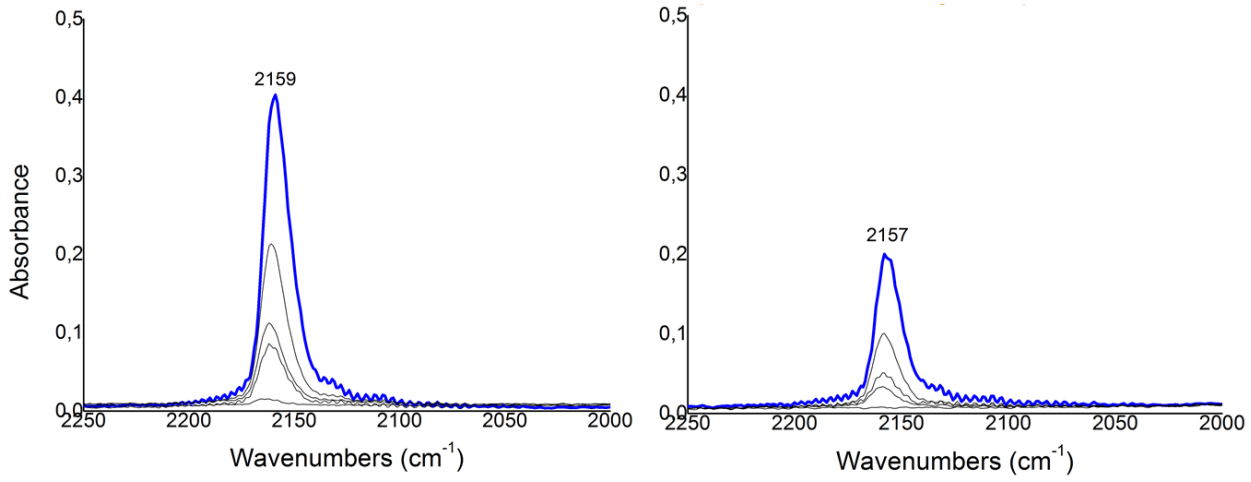

Figure 54 FTIR spectra of adsorbed CO before (left) and after (right) ethanol adsorption on I1,0CuO/TiO_2

Eventually it is worth to have a look on ethanol-adsorbed sample in 2000-4000 cm^{-1} region and 1000-1200 cm^{-1} region. As shown in Figure 55 the CH_3 stretching, just below 3000 cm^{-1}, peak was remarkably more intense in pristine TiO_2 than in Cu-promoted ones (indicated by red arrows). This observation supports that suppose previously on CO band: ethanol was stronger adsorbed on TiO_2 than Cu-promoted TiO_2. Another interesting comment relies on 1000-1200 cm^{-1} region: besides band intensity, in TiO_2 two band were seen (indicated by blue arrows), while in Cu-promoted sample

only one band is observed (indicated orange arrow). These signals correspond to ethoxy adsorbed species.

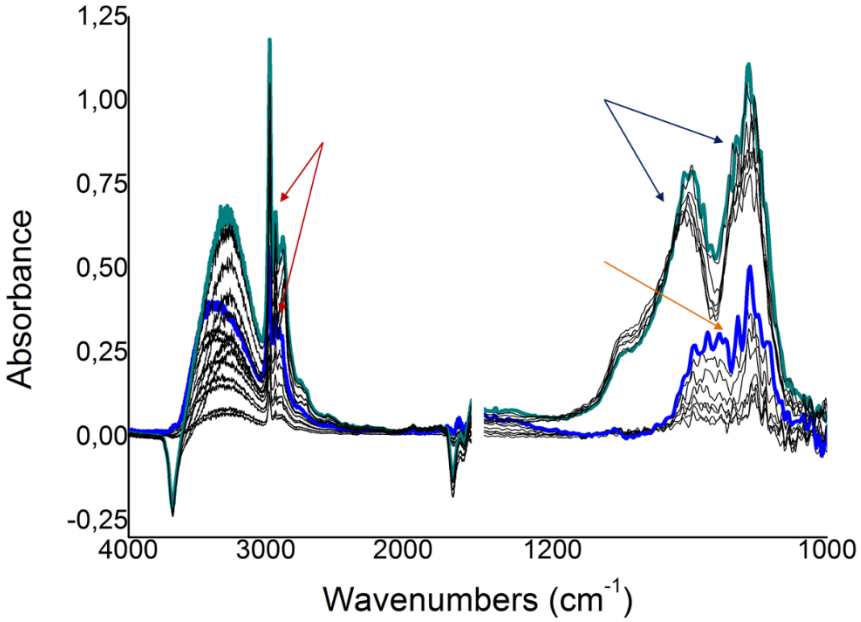

Figure 55 FTIR spectra of adsorbed ethanol on TiO_2 (green) and I1,0CuO/TiO_2 (blue)

Although further detailed studies will be needed to understand the actual coordination way (i.e. linear or bridged) of ethoxy species here observed, some interesting consideration can be done. First ethanol was adsorbed by losing a proton, as ethoxy surface specie. Second adsorption is stronger in TiO_2 rather than in Cu-promoted TiO_2 and in different way in the two catalysts. Since TiO_2 was less active than promoted-TiO_2, this can be mean than ethoxy group adsorption on titania is too strong and was not favourable to photocatalytic activity. Moreover, its coordination way to the surface also could play a significat role too. Further analyses will be needed in order to confirm these hypotheses, especially *in-situ* measurement on irradiated catalyst.

Concluding, FTIR spectroscopy shows that Cu-promoted photocatalyst had a widely dispersed CuO on their surface and lower hydroxyl groups on surface, moreover it was able to efficiently separate electron-hole couple. This leads to a weaker ethanol adsorption as ethoxy species, although this did not hinder photocatalytic activity, probably because weakly adsorbed ethanol scavenged holes more efficiently than stronger adsorbed ones. Another hypothesis is that electron-hole separation was more important than their transfer to adsorbed molecule since electrons on titania's CB are efficiently transferred to copper oxide promoter.

3.5. Conclusions

The photocatalyst formulation, meaning both titanium dioxide synthesis and promoter introduction, is essential since it heavily affects the catalytic behaviour. Copper (II) oxide was proven to be a promising co-catalyst, but its introduction technique is crucial since it considerably affects physico-chemical properties and thus photocatalytic activity of the material. Moreover, low cost and potentially biomass-derived additives (ligands), and no organic solvents were involved in the copper-promoted material synthesis, meaning a cheap and sustainable formulation. IR spectroscopy measurements showed a highly dispersed copper oxide co-catalyst on catalyst surface, that hindered reagent adsorption but gave the best catalytic activity result. Moreover, information concerning the possibly reaction mechanism was obtained.

Concluding lab-made titanium dioxide was proven to be more active than P25, due to high surface area and probably diverse crystal phase composition. Copper introduction as co-catalyst remarkably increases catalytic activity, although the best result was obtained on the low-surface area P25. DP method was also proven to be a promising technique for copper introduction, giving better result than those reported in literature.

3.6. References

1. G. Auer, P. Woditsch, A. Westherhaus, J. Kischkewitz, W.-D. Griebler, M. De Liedekerke, Ullmann's Encyclopedia of Industrial Chemistry, Pigment, Inorganic, 2. White Pigments, vol. 27, 257-289, Wiley-VCH 2012
2. X. Chen, S. S. Mao, *Chem. Rev.* 107 (**2007**) 2891-2959
3. C. H. Bartholomew, R. J. Farrauto, Fundamentals of Industrial Catalytic Processes 2nd ed., John Wiley & sons, 2006
4. H. Sibum, V. Güther, O. Roidl, F. Habashi, H. U. Wolf, Ullmann's Encyclopedia of Industrial Chemistry, Titanium, Titanium Alloys and Titanium Compounds, vol. 37, 51-78, Wiley-VCH 2012
5. Titanium mineral concentrates, UGCS 2017
6. A. Fujishima, T. N. Rao, D. A. Tryk, *J. Photochem. Photobiol., C* 1 (**2000**) 1–21
7. *Y.* Boyjoo, H. Sun, J. Liu, V. K. Pareek, S. Wang, *Chem. Eng. J.* 310 (**2017**) 537-559
8. *M.* Pelaez, N. T. Nolan, S. C. Pillai, M. K. Seery, P. Falaras, A. G. Kontos, P. S.M. Dunlop, J. W.J. Hamilton, J. A. Byrne, K. O'Shea, M. H. Entezari, D. D. Dionysiou, *Appl. Catal., B* 125 (**2012**) 331-349
9. Y. Ma, X. Wang, Y. Jia, X. Chen, H. Han, C. Li, *Chem. Rev.* 114 (**2014**) 9987-10043
10. D. A. H. Hanoar, C. C. Sorrell, *J. Mater. Sci.* 46 (**2011**) 855-874
11. S. Hackenberg, G. Friehs, K. Froelich, C. Ginzkey, C. Koehler, A. Scherzed, M. Burghartz, R. Hagen, N. Kleinsasser, *Toxicol. Lett.* 195 (**2010**) 9-14
12. Z. H. N. Al-Azri, W.-T. Chen, A. Chan, V. Jovic, T. Ina, H. Idriss, G. I. N. Waterhouse, *J. Catal.* 239 (**2015**) 355-367
13. D. Reyes-Coronado, G. Rodríguez-Gattorno, M. E. Espinosa-Pesqueira, C. Cab, R. De Coss, G. Oskam, *Nanotechnology*, 19 (**2008**) 145605
14. A. Di Paola, G. Cufalo, M. Addamo, M. Bellardita, R. Campostrini, M. Ischia, R. Ceccato, L. Palmisano, *Colloids Surf., A* 317 (**2008**) 366–376
15. J. Zhang, P. Zhou, J. Liu, J. Yu, *Phys. Chem. Chem. Phys.* 16 (**2014**) 20382-20386
16. K. Shimura, H. Yoshida, *Energy Environ. Sci.* 4 (**2011**) 2467-2481
17. A. V. Puga, *Coord. Chem. Rev.* 315 (**2016**) 1-66
18. N. Serpone, D. Lawless, R. Khairutdinovt, *J. Phys. Chem.* 99 (**1995**) 16646-16654
19. T. Sreethawong, Y. Suzuki, S. Yoshikawa, *J. Solid State Chem.* 178 (**2005**) 329-338
20. J. Yan, G. Wu, N Guan, L. Li, Z. Li, X. Cao, *Phys. Chem. Chem. Phys.* 15 (**2013**) 10978-10988
21. A. Scalafani, J. H. Herrmann, *J. Phys. Chem.* 100 (**1996**) 13655-13661
22. A. Kudo, Y. Miseki, *Chem. Soc. Rev.* 38 (**2009**) 253-278
23. AEROXIDE®, AERODISP® and AEROPERL® Titanium Dioxide as Photocatalyst, Technical information 1243, Evonik Industries
24. W.-T- Chen, A. Chan, Z. H. N. Al-Azri, A. G. Dosado, M. A. Nadeem, D. Sun-Waterhouse, H. Idriss, G. I.N. Waterhouse, *J. Catal.* 329 (**2015**) 499-513
25. I. K. Kho, A. Iwase, W. Y. Teoh, L. Mädler, A. Kudo, R. Amal, *J. Phys. Chem. C* 114 (**2010**) 2821-2829

26. E. P. Melián, M. Nereida Suárez, T. Jardiel, J.M. Doña Rodríguez, A.C. Caballero, J. Araña, D.G. Calatayud, O. González Díaz, *Appl. Catal., B* 152–153 (**2014**) 192–201
27. K. V. Baiju, S. Shukla, K. S. Sandhya, J. James, K. G. K. Warrier, *J. Phys. Chem. C* 111 (**2007**) 7612-7622
28. G. L. Chiarello, M. H. Aguirre, E. Selli, *J. Catal.* 273 (**2010**) 182–190
29. S. Zhang, Biyu Peng, Siyuan Yang, Hongjuan Wang, Hao Yu, Yueping Fang, Feng Peng, Int. J. Hydrogen Energy 40 (2015) 303-310
30. S. Zhang, B. Peng, S. Yang, Y. Fang, F. Peng, *Int. J. Hydrogen Energy* 38 (**2013**) 13866-13871
31. P. Carmichael, D. Hazafy, D. S. Bhachu, A. Mills, J. A. Darr, I. P. Parkin, *Phys. Chem. Chem. Phys.* 15 (**2013**) 16788-16794
32. A. V. Korzhak, N. I. Ermokhina, A. L. Stroyuk, V. K. Bukhtiyarov, A. E. Raevskaya, V. I. Litvin, S. Y. Kuchmiy, V. G. Ilyin, P. A. Manorik, *J. Photochem. Photobiol., A* 198 (**2008**) 126-134
33. S. Xu, A. J. Du, J. Liu, J. Ng, D. D. Sun, *Int. J. Hydrogen Energy* 36 (**2011**) 6560-6568
34. J. Jitputti, Y. Suzuki, S. Yoshikawa, *Catal. Comm.* 9 (**2008**) 1265–1271
35. S. Sakthivel, M.C. Hidalgo, D.W. Bahnemann, S.-U. Geissen, V. Murugesan, A. Vogelpohl, *Appl. Catal., B* 63 (**2006**) 31-40
36. A. Olivo, V. Trevisan, E. Ghedini, F. Pinna, C.L. Bianchi, A. Naldoni, G. Cruciani, M. Signoretto, *J. CO2 Utiliz.* 12 (**2015**) 86-94
37. L. S. Al-Mazroai, M. Bowker, P. Davies, A. Dickinson, J. Greaves, D. James, L. Millard, *Catal. Today* 122 (**2007)** 46–50
38. G. Wu, T. Chen, W. Su, G. Zhou, X. Zong, Z. Lei, C. Li, *Int. J. Hydrogen Energy* 33 (**2008**) 1243 – 1251
39. W.-T. Chen, A. Chan, D. Sun-Waterhouse, T. Moriga, H. Idriss, G. I. N. Waterhouse, *J. Catal.* 326 (**2015**) 43–53
40. J. Yu, Y. Hai, M. Jaroniec, *J. Colloid Interface Sci.* 357 (**2011**) 223–228
41. J. A. Schwarz, C. Contescu, A. Contescu, *Chem. Rev.* 95 (**1995**) 477-510
42. V. Trevisan, A. Olivo, F. Pinna, M. Signoretto, F. Vindigni, G. Cerrato, C. L. Bianchi, *Appl. Catal., B* 160–161 (**2014**) 152–160
43. Sigma Aldrich website: http://www.sigmaaldrich.com/catalog/product/aldrich/333980?lang=it&region=IT
44. Sigma Aldrich website: http://www.sigmaaldrich.com/catalog/product/aldrich/205273?lang=it&region=IT
45. Sigma Aldrich website: http://www.sigmaaldrich.com/catalog/product/aldrich/244112?lang=it&region=IT
46. H. von Plessen, Ullmann's Encyclopedia of Industrial Chemistry, Sodium Sulfate, vol. 33, 383-395, Wiley-VCH 2012
47. K.-H. Zapp, K.-H. Wostbrock, M. Schäfer, K. Sato, H. Seiter, W. Zwick, R. Cerutziger, H. Leiter, Ullmann's Encyclopedia of Industrial Chemistry, Ammonium Compounds, vol. 3, 263-285, Wiley-VCH 2012
48. F. A. Cotton, G. Wilkinson, Advanced Inorganic Chemistry 3rd ed., John Wiley & sons, 1972
49. The Essential Chemical Industry website: http://www.essentialchemicalindustry.org/chemicals/titanium-dioxide.html
50. InfoMine website: http://www.infomine.com/investment/metal-prices/

51. W.-T. Chen, V. Jovic, D. Sun-Waterhouse, H. Idriss, G. I. N. Waterhouse, *Int. J. Hydrogen Energy* 38 (**2013**) 15036-15043
52. C. Ampelli, C. Genovese, R. Passalacqua, S. Perathoner, G. Centi, *Appl. Therm. Eng.* 70 (**2014**) 1270-1275
53. L. Clarizia, D. Spasiano, I. Di Somma, R. Marotta, R. Andreozzi, D. D. Dionysiou, *Int. J. Hydrogen Energy* 39 (**2014**) 16812-16831
54. H. W. Richardson, Ullmann's Encyclopedia of Industrial Chemistry, Copper Compounds, vol. 10, 273-298, Wiley-VCH 2012
55. K. Lascelles, L. G. Morgan, G. Nicholls, D. Beyersmann, Nickel Compounds, Ullmann's Encyclopedia of Industrial Chemistry, vol. 24, 117-124, Wiley-VCH 2012
56. S. Zhang, B. Peng, S. Yang, Y. Fang, F. Peng, *Int. J. Hydrogen Energy* 38 (**2013**) 13866-13871
57. L. Li, L. Xu, W. Shi, J. Guan, *Int. J. Hydrogen Energy* 38 (**2013**) 816-822
58. J.-D. Kwon, Se-Hun Kwon, Tae-Hoon Jung, Kee-Seok Nam, Kwun-Bum Chung, Dong-Ho Kim, Jin-Seong Park, *Appl. Surf. Sci.* 285 (**2013**) 373-379
59. J. Bandara, C. P. K. Udawatta, C. S. K. Rajapakse, *Photochem. Photobiol. Sci.* 4 (**2005**) 857-861
60. T. Montini, V. Gombac, L. Sordelli, J. J. Delgado, X. Chen, G. Adami, P. Fornasiero, *ChemCatChem* 3 (**2011**) 574-577
61. Y. Ge, Z. H. Shah, C. Wang, J. Wang, W. Mao, S. Zhang, R. Lu, *Appl. Mater. Interfaces* 7 (**2015**) 26437-26444
62. L. S. Yoong, F. K. Chong, B. K. Dutta, *Energy* 34 (**2009**) 1652-1661
63. P. Munnik, P. E. de Jongh, K. P. de Jong, *Chem. Rev.* 115 (**2015**) 6687-6718
64. L. Prati, A. Villa, *Catalysts* 2 (**2012**) 24-37
65. A. J. van Dillen, R. J. A. M. Terörde, D. J. Lensveld, J. W. Geus, K. P. de Jong, *J. Catal.* 216 (**2003**) 257–264
66. F. H. Verhoff, H. Bauweleers, , Ullmann's Encyclopedia of Industrial Chemistry, Citric Acid, vol. 27, 1-9, Wiley-VCH 2015
67. C. S. Lee, M. K. Aroua, W. M. A. W. Daud, P. Cognet, Y. Pérès-Lucchese, P.-L. Fabre, O. Reynes, L. Latapie, *Renew. Sustainable Energy Rev.* 24 (**2015**) 963-972
68. R. W. Parry, F. W. Dubois, *J. Am. Chem. Soc.* (**1952**) 3749-3753
69. K. S. W. Sign, D. H. Everett, R. A. W. Haul, L. Moscou, R. A. Pierotti, J. Rouquérol, T. Siemieniewska, *Pure & Appl. Chem.* 57 (**1985**) 603-619
70. G. Leofanti, M. Padovan, G. Tozzola, B. Venturelli, *Catal. Today* 41 (**1998**) 207-219
71. MicrotracBEL website: http://www.microtrac-bel.com/en/tech/bel/seminar02.html
72. D. A. Skoog, F. J. Holler, S. R. Crouch, Fundamentals of analytical chemistry 8th ed., Thomson-Brooks/Cole 2003
73. J. W. Niemantsverdriet, Spectroscopy in Catalysis, Wiley-VCH 1995
74. V. Trevisan, A. Olivo, F. Pinna, M. Signoretto, F. Vindigni, G. Cerrato, C. L. Bianchi, *Appl. Catal., B* 160-161 (**2014**) 152-160
75. I. Grigioni, M. V. Dozzi, M. Bernareggi, G. L. Chiarello, E. Selli, *Catal. Today* 281 (**2017**) 214-220
76. Kubelka P., Munk F., *Zeitschrift für Technische Physik*, 12 (**1931**) 593-601
77. P. Atkins, J. de Paula, Atkins' Physical Chemistry 8th ed., Oxford University Press 2006
78. Y. Waseda, E. Matsubara, K. Shinoda, X-Ray Diffraction Crystallography, Springer 2011

79. J. M. Thomas, W. J. Thomas, Principles and Pratice of Heterogeneous Catalysis, Wiley-VCH 1997
80. V. Trevisan (2011), Sviluppo di materiali a base di TiO2 per l'abbattimento di inquinanti, Ph.D. thesis, Departement of Molecular Science and Nanosystems, Venice Ca' Foscari University
81. H. Dimitroula, V. M. Daskalaki, Z. Frontistis, D. I. Kondarides, P. Panagiotopoulou, N. P. Xekoukoulotakis, D. Mantzavinos, *Appl. Catal., B* 117-118 (**2012**) 283-291
82. Titanium Dioxide for Catalysts and Supports, Euro Support Manufacturing (ESM)
83. A. V. Puga, A. Forneli, H. García, A. Corma, *Adv. Funct. Mater.* 24 (**2014**) 241–248
84. F. Boccuzzi, A. Chiorino, G. Martra, M. Gargano, N. Ravasio, B. Carrozzini, *J. Catal.* 165 (**1997**) 129-139
85. S. Yashnik, Z. Ismagilov, V. Anufrienko, *Catal. Today* 110 (**2005**) 310–322
86. J. J. Bravo-Suárez, B. Subramaniam, R. V. Chaudhari, *J. Phys. Chem. C* 116 (**2012**) 18207–18221
87. X. Chen, L. Liu, F. Huang, *Chem. Soc. Rev.* 44 (**2015**) 1861-1885
88. *A. Y. Nosaka, T. Fujiwara, H. Yagi, H. Akutsu, Y. Nosaka, Langmuir 19 (**2003**) 1935-1937*
89. K.I. Hadjiivanov, G.N. Vayssilov, *Adv. Catal.* (**2002**) 307-511
90. M. A. Kohler, N. W. Cant, M. S. Wainwright, D. L. Trimm, *J. Catal* 117 (**1989**) 188-201
91. H. Kato, K. Asakura, A. Kudo, *J. Am. Chem. Soc.* 125 (**2003**) 3082-3089
92. E. Taboada, I. Angurell, J. Llorca, *J. Catal.* 309 (**2014**) 460-467

4. Conclusions

Photoreforming is a sustainable yet challenging process to obtain hydrogen but knowledge and technologies need to be improved in order to apply it on an industrial scale. In this thesis work a lab-scale photoreforming process was developed, aiming at improving efficiency and sustainability. Reaction conditions were optimised in order to achieve these goals (chapter 2), in particular composition of the gas phase, which in turn is affected by temperature and composition of liquid solution, and gas flow. In this work a generally lower irradiance was used than those reported in literature. This condition improve process's sustainability however allowing interesting result in term of photocatalytic activity.

Concerning the catalyst development, a very efficient and cheap catalyst, CuO/TiO_2, was formulated obtaining remarkable results, especially in term of AQY, with respect to those reported in literature. In particular, an easy but effective technique (deposition-precipitation) was proven to considerably boost catalytic activity. IR spectroscopy verified that co-catalyst was highly dispersed on titanium dioxide surface, identified that ethanol (reagent) interacts differently with promoted and un-promoted titania and gave information concerning a possible reaction mechanism. Eventually, synthetic procedure was improved: two different ligands, both cheap and biomass-derived, were used and both were proven to give excellent photocatalytic results.

Concluding, in this thesis work an efficient and sustainable photoreforming process was developed. Further development will be aimed at tuning both reaction conditions (e.g. composition of ethanol solution close to real bioethanol) and catalyst design. In particular, possible strategies for the latter could be a higher selectivity toward complete conversion of ethanol to carbon dioxide, and efficiency under visible-light.